Quantum manipulation of nitrogen-vacancy centers in diamond: from basic properties to applications

A dissertation presented

by

Jeronimo Maze Rios

to

The Department of Physics

in partial fulfillment of the requirements

for the degree of

Doctor of Philosophy

in the subject of

Physics

Harvard University

Cambridge, Massachusetts

April 2010

Thesis advisor

Mikhail D. Lukin

Author

Jeronimo Maze Rios

Quantum manipulation of nitrogen-vacancy centers in diamond: from basic properties to applications

Abstract

This thesis presents works not only to understand the spin degree of freedom present in the nitrogen-vacancy defect in diamond: its internal structure and its relation to its environment, but also to find novel applications of it in metrology. First, a mathematical model is develop to understand how this defect couples to a nuclear spin bath of Carbon 13 which constitutes the main dephasing mechanism in pure natural diamond. Next, we demonstrate the use of this defect to sense external oscillating magnetic fields. The high sensitivity and the small sensing volume achieved when a defect is placed in a nanocrystal of few tents of nanometers in diameter, allows this sensor to detect single electronic spins and even single nuclear spins. This sensitivity, proportional to the signal to noise per readout, can be improve by the help of the environment of this defect. We show that strongly interacting nearby nuclei can enable repetitive readout schemes to improve the signal to noise of the electronic spin signal. We also combine ideas from the microscopy community such as stimulated emission depletion to enable high spatial resolution magnetometry. Finally, we develop a formalism based on group theory to understand the internal structure of defects in solids such as their selection rules and the effect of spin-spin and spin-orbit

interactions even when perturbations reduce the symmetry group of the system.

Contents

Citations to Previously Published Work

Large portions of Chapter 2 have appeared in the following paper:

> "Electron spin decoherence of single nitrogen-vacancy defects in diamond", J. R. Maze, J. M. Taylor, and M. D. Lukin, Phys. Rev. B **78**, 094303 (2008), `abs/0805.0327`.

Chapter 3 appeared in the following publication:

> "Nanoscale magnetic sensing with an individual electronic spin in diamond", J. R. Maze, P. L. Stanwix, J. S. Hodges, S. Hong, J. M. Taylor, P. Cappellaro, L. Jiang, M. V. Gurudev Dutt, E. Togan, A. S. Zibrov, A. Yacoby, R. L. Walsworth and M. D. Lukin, Nature **455**, 644-647 (2008).

Chapter 4 appears in its entirety as

> "Repetitive Readout of a Single Electronic Spin via Quantum Logic with Nuclear Spin Ancillae", L. Jiang, J. S. Hodges, J. R. Maze, P. Maurer, J. M. Taylor, D. G. Cory, P. R. Hemmer, R. L. Walsworth, A. Yacoby, A. S. Zibrov and M. D. Lukin, Science **326**, 267 (2009).

Most of Chapter 5 has been published as

> "Far-field optical imaging and manipulation of individual spins with nanoscale resolution", P. C. Maurer, J. R. Maze, P. L. Stanwix, L. Jiang, A.V. Gorshkov, A.A. Zibrov, B. Harke, J.S. Hodges, A.S. Zibrov, D. Twitchen, S.W. Hell, R.L. Walsworth, and M.D. Lukin, submitted to Nature Physics (2009).

Finally, some portions of Chapter 6 is in preparation and it will be published as

> "Group theory of defects: Nitrogen vacancy center in diamond", J. R. Maze, A. Gali, E. Togan, Y. Chu, A. Trifonov, E. Kaxiras, and M. D. Lukin, to be submitted.

Some of the above publications are available as preprints by following the `typewriter font` at the following URL:

> `http://arXiv.org`

Acknowledgments

I am very grateful to have spent most of my years at Harvard working with Mikhail Lukin. His experience and the way he approaches physical problems have taught me to be rigorous and to tackle aspects of physics with a level of confidence that I never had before. I am also grateful to Ronald Walsworth. Working with him, a scientist who can achieve high impact results in multidisciplinary projects, has been a remarkable demonstration of the overlap between physics and other disciplines. Not only will I remember him as a researcher with great leadership skills but also as a friend. I hope to have fruitful collaborations in the near future with both Misha and Ron.

During my first theoretical project (Chapter 2), I was lucky to work with Jake Taylor. I appreciate his sharpness and high level of comprehension on the subject as well as his ability to overcome difficulties. At the end of my Ph.D., Paul Stanwix, My Linh Pham and David Lesage in Ron's laboratory experimentally confirmed many of the theoretical findings described in Chapter 2. I am thankful to all of them for their careful measurements and systematic studies on the magnetic field anisotropy of the NV center. I also thank David Glenn and Tsun Kwan Yeung for their contribution to this experiment.

For my first experimental project, I am immensely grateful for the great and hard work of Jonathan Hodges, Paul Stanwix, and Sungkun Hong. I am indebted for their willingness and enthusiasm to work and the pleasant environment they generated. However, we built our work on the shoulders of pioneers, Lily Childress and Gurudev Dutt. Their excellent research strongly influenced our work and made much of our success possible. I am indebted to them and also to Emre Togan and Sasha Zibrov

for all the unconditional help I received during the first months of my experimental project. I thank Liang Jiang and Paola Cappellaro for their theoretical contributions and to professors Amir Yacoby and Ronald Walsworth for their experimental help.

I am grateful to Peter Maurer and Paul Stanwix for their arduous and persistent work on the high spatial resolution experiment. I thank Benjamin Harke whose experience and help was indispensable to quickly achieve results in the early stages of this project. It was also a great pleasure to have worked with professor Stefan Hell. I had a wonderful time while visiting Gottingen and I am really grateful for Stefan's hospitality. During my visit to Germany, it was a real pleasure to work with Eva Rittweger and Dominik Wildnger and I am obliged for their kindness in sharing their experience and useful tips on the stimulated emission depletion experiments. I thank Alexey Gorshkov and Liang Jiang for their contributions on the interpretation of the Zeno effect in our experiments. I would also like to thank Sasha Zibrov and Zhurik Zibrov for their contributions to this experiments. Finally, I thank Huiliang Zhang and Sebastien Pezzagna for their help to implant one of our samples at Bochum University.

During my Ph.D., I received help from many people from several groups at Harvard University. I would like to thank Alexei Akimov, Mughees Khan, Frank Koppens, and Parag Deotare. In particular, Phil Hemmer has contributed numerous useful comments that helped me not only to overcome experimental difficulties but also to better understand the dynamics of the NV center. In this regard, I am also thankful to Fedor Jelezko and Georg Wrachtrup.

I am especially grateful to professor Marko Loncar for inviting me to participate

on his research. I had a pleasant and fruitful time working with Marko as well as with Tom Babinec and Birgit Haussman. I hope to continue collaborating with Marko, Tom, Birgit and Irfan Bulu on their exciting exploration of the phonon dynamic of the NV center.

I give special thanks to professor Adam Gali for fruitful discussions on group theory and on understanding the properties of NV centers. We went together through many of the results of Chapter 6, and Adam's expertise and insight was key to unraveling the properties of the NV center. Many of the results presented in this chapter would not been possible without the fruitful discussions with Emre Togan, Yiwen Chu and Alexei Trifonov. I am grateful for their patience and perseverance in perhaps one of the most difficult experiments I have witnessed. I also thank professor Efthimios Kaxiras for useful comments.

I have enjoyed interesting and illuminating discussions with Mohammad Hafezi, Peter Rabl, Dirk Englund, and Philip Walther on topics ranging from topology to the strangeness of quantum mechanics. In particular, I would like to thanks Brendan Shields for his enthusiasm on the road to reality and for his unconditional help on proof reading this thesis.

I would like to thank Sheila Ferguson for her counseling and dedication throughout my Ph.D. At the beginning of my graduate studies, I received much help from Ronald Walsworth folks . In particular, Leo Tsai, Ross Mair, David Phillips, Irina Novikova and Alex Glenday. I am also grateful to Patrick Maletinsky, Michael Grinolds, Garry Goldstein, Nick Chisholm, Georg Kucsko, Agnieszka Iwasievicz-Wabing, and John Morton. I also want to thank my friends Esteban Calvo, Paula Errazuriz, Cristobal

Paredes, Francisco Pino, Karina Veliz, and Joaquin Blaya for useful comments and support during my Ph.D.

Finally, I would like to thank my parents and especially my wife, Tamy, to whom I am indebted for life, for her unconditional help and sacrifice during the entire period of my graduate studies.

Dedicado a mis padres,
Fernando y Alicia,
y a mi esposa Tamy.

Chapter 1

Introduction

1.1 Background

For many years single atoms have drawn the attention of scientists due to the great controllability they exhibit over both internal and external degrees of freedom. Such control has been achieved over the past decade, e.g., for atoms captured in electromagnetic traps in vacuum. Single atoms can be prepared by optical pumping and their internal states can be probed coherently[1, 2] via optical or microwave radiation, often exhibiting exceptionally long coherence times[3] due to being well isolated from sources of decoherence. Single atoms can also be coupled to specific modes of the electromagnetic field in optical[4] as well as microwave cavities[5]. However, making two neighboring atoms interact controllably requires precise manipulation of their motional degrees of freedom. Ion traps[6] can be used to isolate single and multiple atomic ions and control their motional degrees of freedom to such a degree that two or more ions can be coupled through their collective quantized motion[7, 8]. Many years

of experimental work and redesign were needed to realize scalable ion traps where many ions interact in such a controllable way [9, 10] at the expenses of complicated architecture.

In contrast, in solid state devices, quantum systems are fixed relative to each other and the nature of their degrees of freedom can be many: e.g., superconducting flux qubits[11], the spin degree of freedom of a quantum dot in GaAs[12], mechanical resonators[13], and the spin degree of freedom of the Phosphorus defect in Silicon[14]. Most of these systems require very low temperatures, as they strongly couple to vibrations, excitations or electron spin baths. For example, Phosphorus defects in Silicon present a ground state electronic spin 1/2, which becomes stable only below 20 K due to the proximity of the defect states to the conduction band; and achieves long electron spin coherence times only below 1.5 K due a the strong spin-lattice interaction[15, 16]. In addition, the experimental signal for such paramagnetic defects has to date consisted of ESR-like measurements of large ensembles of paramagnetic spins in Silicon[17].

However, large band gap materials can contain deep defects where the ground state is far from the conduction band minimum (CBM), thereby achieving a stable ground state at large temperatures. As an example, diamond has a gap of 5.5 eV and contains many stable defects such as the nitrogen-vacancy (NV) center (3.3 eV below the CBM[18]) and the nitrogen substitutional defect (1.7 eV below the CBM[19]). Being deep in the gap of a solid-state system is essential for a stable ground state, however, it is not enough to share the nice properties of single atoms (long spin coherence times, optically-accessible electronic transitions, etc.). For this, the excited

state of the defect should also lie inside the gap of the material, as happens with the excited state of the NV center (1.3 eV below the CBM) and Nickel centers in diamond[20]. This enables the centers to be localized optically and individually[21] if no other centers are closer than the diffraction limited optical resolution.

Furthermore, the NV center in diamond is special because its electronic spin degree of freedom can be controllably accessed, initialized and readout optically[22], as well as rotated under resonant microwave radiation.

NV centers have recently become leading candidates for a number of applications such as quantum computers[23], quantum cryptography and communication[24], magnetic sensors[25, 26, 27, 28], spin-photon entanglement, and coupling them to a wide variety of interesting systems to achieve scalability and single shot readout [29, 30, 31]. However, to successfully implement these applications it is necessary to understand in detail the complex structure of this defect and how it is coupled to its environment.

In this thesis we cover both applications and theoretical efforts to understand the nitrogen-vacancy defect in diamond.

1.2 Description of this thesis

This thesis describes two theoretical (Chapters 2 and 6) and three experimental projects (Chapters 3, 4 and 5). Chapter 2 presents a detailed model to understand the decoherence of the electronic spin of the NV center due to a nuclear bath of Carbon-13. Chapter 3 demonstrates the use of NV cetners as magnetic sensors. Chapter 4 experimentally demonstrates an algorithm to repetitively readout the state of the electronic spin with the help of the environment. Chapter 5 describes a technique to

image and manipulate individuals spins with nanoscale resolution. Finally, Chapter 6 provides a detailed way to analyze and understand defects in solids.

1.2.1 Decoherence

A common problem of quantum systems is their lack of isolation with their surrounding. In many cases, this constitutes a limitation as the dynamics of the environment cannot always be controlled with high precision and therefore uncoupled from the system. As a result of this interaction, a superposition state of the quantum system (e.g. $|a\rangle + |b\rangle$) looses its coherent becoming a complete mixed state (e.g. $|a\rangle\langle a| + |b\rangle\langle b|$). We call this process decoherence. In Chapter 2, we present a detailed theoretical analysis of the electron spin decoherence in single nitrogen-vacancy defects in ultra-pure diamond. The electron spin decoherence is due to the interactions with ^{13}C nuclear spins in the diamond lattice. Our approach takes advantage of the low concentration (1.1%) of ^{13}C nuclear spins and their random distribution in the diamond lattice by an algorithmic aggregation of spins into small, strongly interacting groups. By making use of this *disjoint cluster* approach, we demonstrate a possibility of non-trival dynamics of the electron spin that can not be described by a single time constant. This dynamics is caused by a strong coupling between the electron and few nuclei and exhibits large variations depending on the distribution of ^{13}C nuclei surronding each individual electronic spin. Our results are in good agreement with experimental data and show the anisotropy of this defect, caused by the crystal lattice, in the response of the coherence time to the angle between the NV axis and the magnetic field. We also make a connection between our full quantum mechanical

description and phenomenological models and discuss how to compare these results with measurements in which a large number of NV centers are probed. We find that although ensemble measurements are the sum of individual signals with a particular decay shape, they can have a different decay shape. Our results are in good agreement with recent experimental observations[32] and allow us to understand the difference between individual and ensemble measurements.

1.2.2 Applications

Magnetometry

Nevertheless, NV centers always showed good enough coherence times so that the sensitive dephasing of a coherent superposition of the spin degree of freedom could be used to sense external magnetic fields. Detection of weak magnetic fields with nanoscale spatial resolution is an outstanding problem in the biological and physical sciences [33, 34, 35, 36, 37]. For instance, at a distance of 10 nanometers, a single electron spin produces a magnetic field of about one microtesla, while the corresponding field from a single proton is a few nanotesla. A sensor able to detect such magnetic fields with nanometer spatial resolution will enable powerful applications ranging from the detection of magnetic resonance signals from individual electron or nuclear spins in complex biological molecules[37, 38] to readout of classical or quantum bits of information encoded in an electron or nuclear spin memory[39]. In Chapter 3 we experimentally demonstrate a novel approach to such nanoscale magnetic sensing, employing coherent manipulation of an individual electronic spin qubit associated with a Nitrogen-Vacancy (NV) impurity in diamond at room temperature[25]. Using

an ultra-pure diamond sample, we achieve detection of 3 nanotesla magnetic fields at kHz frequencies after 100 seconds of averaging. In addition, we demonstrate 0.5 microtesla/$(\text{Hz})^{1/2}$ sensitivity for a diamond nanocrystal with a volume of $(30\text{ nm})^3$.

Repetitive readout

Robust readout of single quantum information processors plays a key role in the realization of quantum computation and communication as well as in quantum metrology and sensing. In Chapter 4 we implement a method for the improved readout of single spins in solid state systems. We make use of quantum logic operations on a system composed of a single electronic spin and several proximal nuclear spin ancillae to repetitively readout the state of the electronic spin. Using coherent manipulation of a single nitrogen vacancy (NV) center in room temperature diamond, full quantum control of an electronic-nuclear system composed of up to three spins is demonstrated. We take advantage of a single nuclear spin memory to obtain a ten-fold enhancement in the signal amplitude of the electronic spin readout. Finally, we demonstrate a two-level, concatenated procedure to improve the readout using a pair of nuclear spin ancillae, representing an important step towards realization of robust quantum information processors using electronic and nuclear spin qubits. Our technique can be used to improve the sensitivity and the speed of spin-based nanoscale diamond magnetometers.

Nanoscale imaging and manipulation of individual spins

A fundamental limit to existing optical techniques for measurement and manipulation of spin degrees of freedom[40, 41, 42, 43, 39, 44, 45, 46] is set by diffraction, which

does not allow spins separated by less than about a quarter of a micrometer to be resolved using conventional far-field optics. In Chapter 4, we report an efficient far-field optical technique that overcomes the limiting role of diffraction, allowing individual electronic spins to be detected, imaged and manipulated coherently with nanoscale resolution. The technique involves selective flipping of the orientation of individual spins, associated with Nitrogen-Vacancy (NV) centers in room temperature diamond, using a focused beam of light with intensity vanishing at a controllable location[47], which enables simultaneous single-spin imaging and magnetometry[25, 27] at the nanoscale with considerably less power than conventional techniques. Furthermore, by inhibiting spin transitions away from the laser intensity null using a quantum Zeno-like effect[48], selective coherent rotation of individual spins is realized. The inhibition is a combination of population hiding and the quantum Zeno effect[48]. We show individual control over two electronic spins separated by 150 nm. This technique can be extended to sub-nanometer dimensions, thus enabling applications in diverse areas ranging from quantum information science to bioimaging.

1.2.3 Understanding defects

Understanding the complex structure of defects in solids is crucial to effectively implement novel applications. The dynamics of defects in solid state systems are determined by the crystal field which is by far the largest interaction present in the defect. In Chapter 6 we present a mathematical procedure to analyze and predict the main properties of the negatively charged nitrogen-vacancy (NV) center in diamond using group theory (GT) which is a leading candidate to realize solid state qubits and

ultrasensitive magnetometers at ambient conditions. Our study particularly restricts on relatively low temperatures limit where both the spin-spin and spin-orbit effects are important to consider. We use a formalism that may be generalized to any defect in solids and demonstrate on our specific example that GT helps to clarify several aspects of the NV-center such as ordering of the singlets in the (e^2) electronic configuration, spin-spin and spin-orbit interaction in the (ae) electronic configuration. We also discuss how the optical selection rules and the response of the center to electric field can be used for spin-photon entanglement schemes.

Chapter 2

Decoherence of single electronic spin in diamond

2.1 Introduction

Isolated spins in solid-state systems are currently being explored as candidates for good quantum bits, with applications ranging from quantum computation [14, 49, 23] and quantum communication[24] to magnetic sensing[25, 27, 28]. The nitrogen-vacancy (NV) center in diamond is one such isolated spin system. It can be prepared and detected using optical fields, and microwave radiation can be used to rotate the spin [50, 51]. Recent experiments have conclusively demonstrated that in ultra pure-diamond the electron spin coherence lifetime is limited by its hyperfine interactions with the natural 1.1% abundance Carbon-13 in the diamond crystal [52, 53]. Thus, developing a detailed understanding of the decoherence properties of such an isolated spin in a dilute spin bath is a challenging problem of immediate practical interest.

This combined system of electron spin coupled to many nuclear spins has a rich and complex dynamics associated with many-body effects.

The decay of electronic spin coherence due to interactions with surrounding nuclei has been a subject of a number of theoretical studies [54, 55]. Various mean-field and many-body approaches have been used to address this problem [56, 57, 58, 59, 60, 61]. In this paper, we investigate a variation of the cluster expansion, developed in Ref. [58]. Our approach takes advantage of the natural grouping statistics for randomly located, dilute impurities, which leads to the formation of small, disjoint clusters of spins which interact strongly within themselves and with the central spin, but not with other such clusters. This suggests a natural hierarchy of interaction scales of the system, and allows for a well-defined approximation that can be seen as an extension of ideas developed in the study of tensor networks [62]. We develop an algorithm for finding such clusters for a given set of locations and interactions, and find that for dilute systems convergence as a function of the cluster size (number of spins in a given cluster) is very rapid. We then apply this technique to the specific problem of the decay of spin-echo for a single NV center, and find good qualitative and quantitative agreement with experiments. In particular, we demonstrate a possibility of non-trival dynamics of the electron spin that can not be described by a single time constant. This dependance is caused by a strong coupling between the electron and few nuclei and results in a substantial spin-echo signal even at microseconds time scale.

Phenomenological models

In this chapter we will see that there is a close connection between the full quantum mechanical solution and phenomenogical models (see Appendix A.1) in which decoherence is modeled by a fluctuating magnetic field with a particular spectral density. In particular, we will recover the relation between the dephasing times for free induction decay (T_2^*), echo experiments (T_2) and the correlation time of the bath (τ_c),

$$T_2 = \sqrt{T_2^* \tau_c} \tag{2.1}$$

where τ_c will be related with dipolar interaction among nuclear spins of the bath.

2.1.1 System and Spin hamiltonian

The negatively charged NV center ([N-V]$^-$) has trigonal C_{3v} symmetry and $^3A_2$ ground state[63] with total electronic spin $S = 1$[64]. Spin-spin interaction leads to a zero-field splitting, $\Delta = 2.87$ GHz, between the $m_s = 0$ and $m_s = \pm 1$ manifolds, where the quantization axis is along the NV-axis. This spin triplet interacts via hyperfine interaction with a spin bath composed of the adjacent Nitrogen-14 and the naturally occuring 1.1% Carbon-13 which is randomly distributed in the diamond lattice.

In the presence of an external magnetic field, the dynamics is governed by the

following hamiltonian,

$$\begin{aligned} H &= \Delta S_z^2 - \gamma_e B_z S_z - \sum_n \gamma_N \mathbf{B} \cdot \mathbf{g}_n(|S_z|) \cdot \mathbf{I}_n \\ &+ \sum_n S_z \mathbf{A}_n \cdot \mathbf{I}_n + \sum_n \delta \mathbf{A}_n(|S_z|) \cdot \mathbf{I}_n \\ &+ \sum_{n>m} \mathbf{I}_n \cdot \mathbf{C}_{nm}(|S_z|) \cdot \mathbf{I}_m. \end{aligned} \tag{2.2}$$

The relatively large zero-field splitting Δ (first term in Equation (2.2)) does not allow the electron spin to flip and thus we can make the so called secular approximation, removing all terms which allow direct electronic spin flips. Non-secular terms have been included up to second order in perturbation theory, leading to the $|S_z|$ dependence of other terms in the Hamiltonian. The second and third terms are, respectively, the Zeeman interactions for the electron and the nuclei, the fourth term is the hyperfine interaction between the electron and each nucleus, the fifth term is an effective crystal-field splitting felt by the nuclear spins, and the last term is the dipolar interaction among nuclei. The specific terms for this hamiltonian are discussed in Appendix A.4.

For the case of the NV center, the nuclear g-tensor, $\mathbf{g}_n$, can be anisotropic and vary dramatically from nucleus to nucleus[53]. This leads to a non-trivial dynamics between the electron and an individual nucleus (electron-nuclear dynamics), and motivates a new approach for the case of a dilute bath of spins described below. In addition, the interaction between nuclei is enhanced by the presence of the electron of the NV center. The resulting effective interaction strength can exceed several times the bare dipolar interaction between nuclei[39].

2.2 Method: Disjoint cluster approach

The large zero-field splitting Δ sets the quantization axis (called NV-axis) and allows us to neglect electron spin flips due to interactions with nuclei. Therefore, we can reduce the Hilbert space of the system by projecting hamiltonian (2.2) onto each of the electron spin states. We can write the projected hamiltonian, $P_{m_s} H P_{m_s}$ (where $P_{m_s} = |m_s\rangle\langle m_s|$), as

$$H_{m_s} = \sum_n \mathbf{\Omega}_n^{(m_s)} \cdot \mathbf{I}_n + \sum_{nm} \mathbf{I}_n \cdot \mathbf{C}_{nm}^{(m_s)} \cdot \mathbf{I}_m + \Delta |m_s| - \gamma_e B_z m_s, \tag{2.3}$$

where m_s denotes the electron spin state, $\mathbf{\Omega}_n$ is the effective Larmor vector for nucleus n and $\mathbf{C}_{nm}$ is the effective coupling between nuclei n and m. In Equation (2.3), we include the zero-field splitting and the Zeeman interaction. These terms provide just static fields whose effect is canceled by spin echo. In this way, we can write the evolution of the bath as $U_{m_s}(\tau) = T\left\{\exp\left(\int_0^\tau H_{m_s}(t')\,dt'\right)\right\}$. An exact expression for U_{m_s} can be found by ignoring the intra-bath interactions ($\mathbf{C}_{nm} = 0$). However, for an interacting bath (with arbitrary $\mathbf{C}_{nm}$), solving U_{m_s} for a large number of nuclei N is a formidable task since it requires describing dynamics within a 2^N dimensional Hilbert space. Therefore, some degree of approximation is needed.

The spin bath considered here is composed of randomly distributed spins, and not all pair interactions among nuclei are equally important. Specifically, interactions decay with a characteristic law $1/R_{mn}^3$, where R_{nm} is the distance between nuclei n and m. As a result, we can break the big problem into smaller ones by grouping those nuclei that strongly interact with each other into disjoint sets. Our procedure is illustrated in Figure 2.1. We denote the k-th group of nuclei as $\mathcal{C}_g^k$, where the

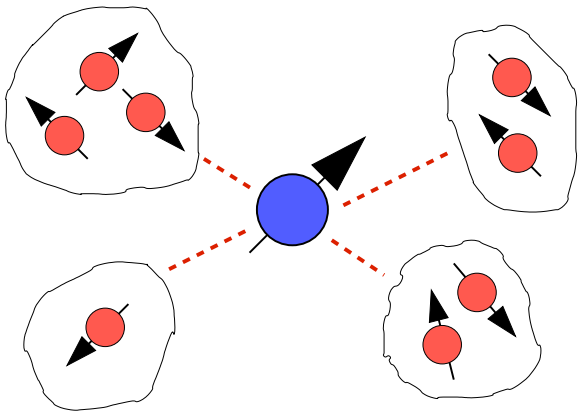

Figure 2.1: **Illustration of the method.** Spins that strongly interact can be grouped together and treated as isolated systems. Interactions that joint different groups can be incorporated as a perturbation.

subindex g indicates that each group has no more than g nuclei. Interactions inside each group (intra-group interactions) are expected to be much larger than interactions among groups (inter-group interactions). Our approximation method will rely upon neglecting the latter.

Formally, we start by separating intra-group interactions and inter-group interactions. We define the operator $H_B = \sum_k H(\mathcal{C}_g^k)$ which contains all electron-nuclear interactions (first term in Equation (2.3)) plus all interactions between bath spins within the same group $\mathcal{C}_g^k$. Similarly, operator $H_A = H(\tilde{\mathcal{C}}_g)(= H - H_B)$ contains all interactions between bath spins in different groups. As a first approximation, we can neglect the inter-group interactions but keep the intra-group interactions. The approximation can be understood by means of the Trotter expansion[65]

$$\exp\left(H_A t + H_B t\right) = \lim_{n\to\infty} \left(\exp\left(H_A t/n\right) \exp\left(H_B t/n\right)\right)^n .$$

Since H_B contains groups of terms that are disconnected from each other, $[H(\mathcal{C}_g^k), H(\mathcal{C}_g^{k'})] =$

0 and we can write the evolution operator as

$$U_g(\tau) = \lim_{n\to\infty} \left(U\left(\tilde{\mathcal{C}}_g, \frac{\tau}{n}\right) \prod_k U\left(\mathcal{C}_g^k, \frac{\tau}{n}\right) \right)^n, \tag{2.4}$$

where $U(\tilde{\mathcal{C}}_g, \frac{\tau}{n})$ is the evolution operator due to hamiltonian $H(\tilde{\mathcal{C}}_g)$ and so on.

To the zeroth order we neglect all terms in H_A since $H(\tilde{\mathcal{C}}_g)$ contains interactions among nuclei that interact weakly. Thus, we set $U(\tilde{\mathcal{C}}_g, \frac{\tau}{n})$ to the identity and simplify Equation (2.4) to

$$U_g(\tau) \approx \prod_k U\left(\mathcal{C}_g^k, \tau\right). \tag{2.5}$$

This approximation requires independent calculation of propagators for each group g, which corresponds to N/g independent calculations of $2^g \times 2^g$ matrices, exponentially less difficult than the original problem of direct calculation of the $2^N \times 2^N$ dimensional matrix. We remark that including the effect of $U(\tilde{\mathcal{C}}_g, \frac{\tau}{n})$ in the Trotterization can be done by using a tree tensor network ansatz wave function [62] where the number of complex coefficients to describe the wave function is $O(N^{log(N)})$ instead of 2^N.

2.3 Electron spin-echo

In this section we analyze the dynamics of the central spin in two cases: (1) when only the hyperfine interaction between the central spin and the nuclei is considered and (2) when the dipolar interaction among Carbon-13 is considered. The former do not lead to decoherence when the magnetic field is aligned with the symmetry axis of the NV center (the NV axis). However, as soon as the magnetic field is misaligned, few nuclei nearby the central spin destroy the coherence of the signal. In the latter case, the signal decoheres due to spin flip-flops between nuclei. We address the many

body problem involved in the evaluation of spin-echo signals.

Electron spin-echo removes static magnetic shifts caused by a spin bath, allowing to measure the dynamical changes of the bath. Assuming that an initial state, $|\varphi\rangle = (|0\rangle + |1\rangle)/\sqrt{2}$, is prepared, the probability of recovering the same state after a time 2τ is

$$p = \mathrm{Tr}(P_\varphi U_T(\tau)\rho U_T^\dagger(\tau)), \tag{2.6}$$

where $P_\varphi = |\varphi\rangle\langle\varphi|$ is the projector operator to the initial state, $\rho = |\varphi\rangle\langle\varphi| \otimes \rho_n$ is the density matrix of the total system, ρ_n is the density matrix of the spin bath, $U_T(\tau) = U(\tau) R_\pi U(\tau)$ is the total evolution of the system where U is the evolution operator under hamiltonian (2.2) and R_π is a π-pulse acting on the subspace $m_s = \{0, 1\}$ of the electron spin manifold. Probability (2.6) can also be written as $p = (1 + S(\tau))/2$, where

$$S(\tau) = \mathrm{Tr}\left(\rho_n U_0^\dagger(\tau) U_1^\dagger(\tau) U_0(\tau) U_1(\tau)\right) \tag{2.7}$$

is known as the pseudo spin and $|S(\tau)| = 0$ is the long-time (completely decohered) signal. In the high temperature limit, the density matrix of the nuclei can be approximated by $\rho_n \approx \mathbb{1}^{\otimes N}/2^N$ where N is the number of nuclei. The generalization of this relation for different sublevels of the triplet state is straighforward, $S(\tau) = \mathrm{Tr}\left(\rho_n U_\alpha^\dagger(\tau) U_\beta^\dagger(\tau) U_\alpha(\tau) U_\beta(\tau)\right)$, where $\alpha = 1$ and $\beta = -1$, for example. In what follows, we analyze the effect of an interacting bath on Equation (2.7).

2.3.1 Non-interacting bath

To understand the effect of an interacting bath we will first analyze the non-interacting case, which displays the phenomenon of electron spin-echo envelope modulation due to electron spin-nuclear spin entanglement. This is completely neglecting interactions among nuclei, $\mathbf{C}_{nm} = 0$. In this regime, the evolution operator is factored out for each nucleus and the pseudo-spin is the product of all single pseudo-spin relations. In the high temperature limit, $\rho_n = \mathbb{1}/2$, we obtain the exact expression[53]

$$S_T(\tau) = \prod_n S_n(\tau) = \prod_n \left(1 - 2\left|\hat{\Omega}_n^{(0)} \times \hat{\Omega}_n^{(1)}\right|^2 \times \sin^2\frac{\Omega_n^{(0)}\tau}{2}\sin^2\frac{\Omega_n^{(1)}\tau}{2}\right). \quad (2.8)$$

When the electron spin is in its $m_s = 0$ state and the external magnetic field points parallel to the NV-axis, the Larmor frequency $\Omega_n^{(0)}$ is set by the external magnetic field, and the nuclei precess with the same frequency $\Omega^{(0)}$. The total pseudo spin is 1 at times $\Omega^{(0)}\tau = 2m\pi$ with m integer. When the electron is in its $m_s = 1$ state, the Larmor vector $\mathbf{\Omega}_n^{(1)}$ has a contact and dipolar contribution from the hyperfine interaction $\mathbf{A}_n$ that may point in different directions depending on the position of the nucleus. As a consequence, when interactions from all nuclei are considered, these electron-nuclear dynamics makes the total pseudo-spin relation collapse and revive. However, when the magnetic field is aligned with the NV axis, this description does not show any decay of the revival peaks.

When the transverse (perpendicular to the NV-axis) magnetic field is non-zero, nuclei near the center experience an enhancement in their g-factors leading to a position-dependent Larmor frequency $\Omega_n^{(0)}$ (see Appendix A.4). This results in an effective decay of the signal since the electron state will not be refocused at the same time for all nuclei. The envelope of the echo singal in this case is given by (see Section

A.2),

$$S_{\text{env}}^{\text{off-axis}}(\tau) \approx \exp\left(-\alpha\theta^2\tau^2\right). \tag{2.9}$$

where α is proportional to the hyperfine interaction squared between the central spin and the corresponding nucleus. See Figure 2.6 and Section 2.6 for experimental verification of this behavior.

2.3.2 Interacting bath: an example

When the intra-bath interactions are considered, the spin-echo signal can show decay in addition to the electron-nuclear dynamics. As an illustrative and simple example, consider a pair of nuclei with their Larmor vectors pointing in the same direction regardless the electron spin state (in this case there is no electron-nuclear dynamics and the non-interacting pseudo-spin relation for two nuclei is $S_{nm} = S_n S_m = 1$ (see Equation 2.8)). When the interaction between nuclei is included, the pseudo-spin relation can be worked out exactly,

$$S_{nm}(\tau) = 1 - \left[\frac{\Delta\Omega_{nm}^0 c_{nm}^1 - \Delta\Omega_{nm}^1 c_{nm}^0}{2}\right]^2 \frac{\sin^2(\omega_{nm}^0\tau)\sin^2(\omega_{nm}^1\tau)}{(\omega_{nm}^0)^2(\omega_{nm}^1)^2}, \tag{2.10}$$

where $(\omega_{nm}^{m_s})^2 = (\Delta\Omega_{nm}^{m_s}/2)^2 + (c_{nm}^{m_s})^2$, $\Delta\Omega_{nm}^{m_s} = \Omega_n^{m_s} - \Omega_m^{m_s}$ and $c_{nm}^{m_s}$ is the strength of the dipolar interaction $c_{nm}^{m_s}(\hat{I}_{n+}\hat{I}_{m-} + \hat{I}_{n-}\hat{I}_{m+} - 4\hat{I}_{nz}\hat{I}_{mz})$ between nuclei n and m. The two frequencies involved in (2.10), ω_{nm}^0 and ω_{nm}^1, are not necessarily the same for different pairs of nuclei. They depend on the relative position between nuclei and the relative position of each nucleus to the NV center. Therefore, when all pair interactions are included the pseudo-spin relation decays. In the following section

we present an approach to incorporates not only this two body interaction but also n-body interactions with $n \leq 6$.

2.4 Application of the disjoint cluster approach

The many-body problem can be readily simplified by following the approximation described in Section 2.2. When the interactions that connects different groups are neglected, the evolution operator is factored out in groups and the spin-echo relation becomes simply

$$S_g(\tau) \approx \prod_k S\left(\mathcal{C}_g^k, \tau\right), \tag{2.11}$$

where $S\left(\mathcal{C}_g^k, \tau\right)$ is the pseudo-spin relation, Equation (2.7), for group $\mathcal{C}_g^k$. $S_g(\tau)$ can be calculated numerically and exactly for small g ($\lesssim 10$). Therefore, electron-nuclear and intra-bath hamiltonians can be simultaneously considered.

In the following section, we present our algorithm for sorting strongly interacting nuclei in a random distributed spin bath into well defined groupings. We take the electron spin-echo signal, with the initial state $|\phi\rangle = (|0\rangle + |1\rangle)/\sqrt{2}$ as a figure of merit. We examine the convergence of our disjoint cluster approach as a function of the maximum group size g and consider the statistics of spin-echo for a variety of physical parameters such as Carbon-13 abundance and magnetic field magnitude and orientation.

2.4.1 Grouping algorithm

One of the criteria to aggregate groups of spins is to consider the strength of the intra-bath interaction. This parameter can be summarized in one variable $\mathbb{C}(i,j)$ which is a scalar function of the interaction $\mathbf{C}^{ij}$ between nuclei i and j. The aggregation algorithm used for this criterion is as follow. Consider an array $\mathbb{A}$ containing the criterion for all pairs ordered from high to low values in $\mathbb{C}$ and let $\{i,j\}_n$ be the n-th nuclear pair in array $\mathbb{A}$. The array $\mathbb{A}$ is scanned completely and one of the following cases applies for each pair $\{i,j\}_n$

- **if nuclei i & j belong to different groups:** join both groups if $\mathcal{N}(\mathbb{G}(i)) + \mathcal{N}(\mathbb{G}(j)) \leq g$.
- **if nucleus i belong to group $\mathbb{G}(i)$ and nucleus j does not belong to any group:** add j to group $\mathbb{G}(i)$ if $\mathcal{N}(\mathbb{G}(i)) < g$. If not, make a new group with j.
- **if nucleus j belong to group $\mathbb{G}(j)$ and nucleus i does not belong to any group:** add i to group $\mathbb{G}(j)$ if $\mathcal{N}(\mathbb{G}(j)) < g$. If not, make a new group with i.
- **if nuclei i & j do not belong to any group:** make a new group with i & j,

where $\mathcal{N}(\mathbb{G})$ is the number of nuclei in group $\mathbb{G}$ and g is the maximum number of nuclei per group. In what follows, we use the criterion $\mathbb{C}(i,j) = (C_{xx}^{ij})^2 + (C_{yy}^{ij})^2 + (C_{zz}^{ij})^2$ (i.e. the interaction between nuclei i and j) to estimate the electron spin-echo in NV centers.

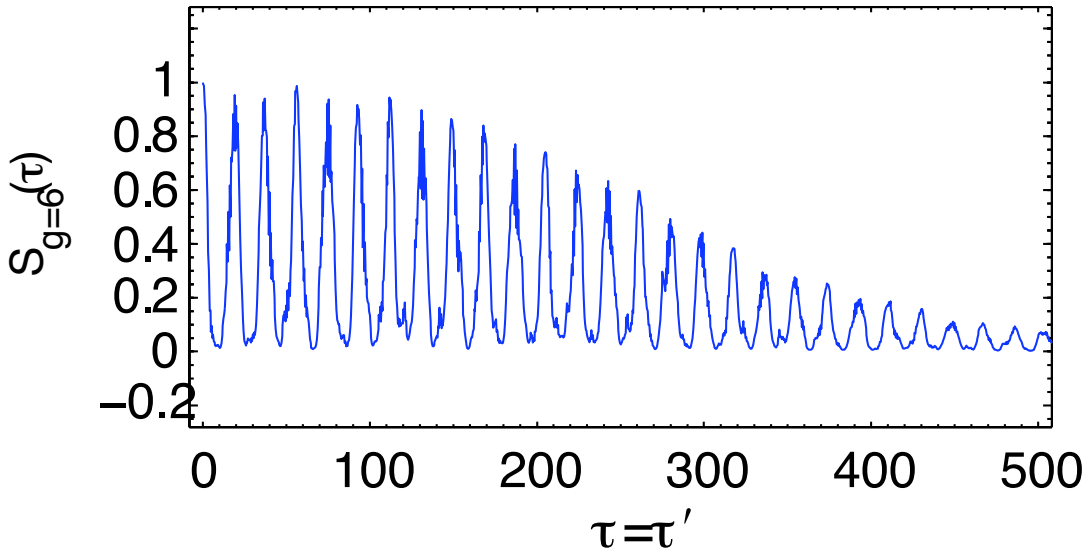

Figure 2.2: **Example of spin echo signal simulation.** Pseudo spin $S_{g=6}(\tau)$ for a single NV center in a magnetic field of 50 Gauss oriented parallel the NV-axis.

2.4.2 Numerical methods and example cases

In the particular case of the NV center, the interaction between nuclei $\mathbf{C}^{ij}$ involves both the bare dipolar interaction and a second order process interaction mediated by the electron spin (see Appendix A.4). The latter interaction does not depend on the distance between nuclei but rather on the distance between each nuclei and the electron. As a result, it can couple two separate nuclei that are near the electron but far from each other. At low fields (< 1000 Gauss), these second order processes are reduced by the large zero-field splitting Δ (≈ 3 GHz) and by the large average distance between nuclei (hundred times the nearest neighbor distance, 100×1.54 $\mathring{A}$, at the natural abundance of ^{13}C (1.1%)). In this regime, the dynamics can be faithfully describe by considering a small number of nuclei (≤ 6) near the electron spin in a single group.

Figure 2.2 shows $S_g(\tau)$ for $g = 6$ (Equation (2.11)) for 750 random and distributed

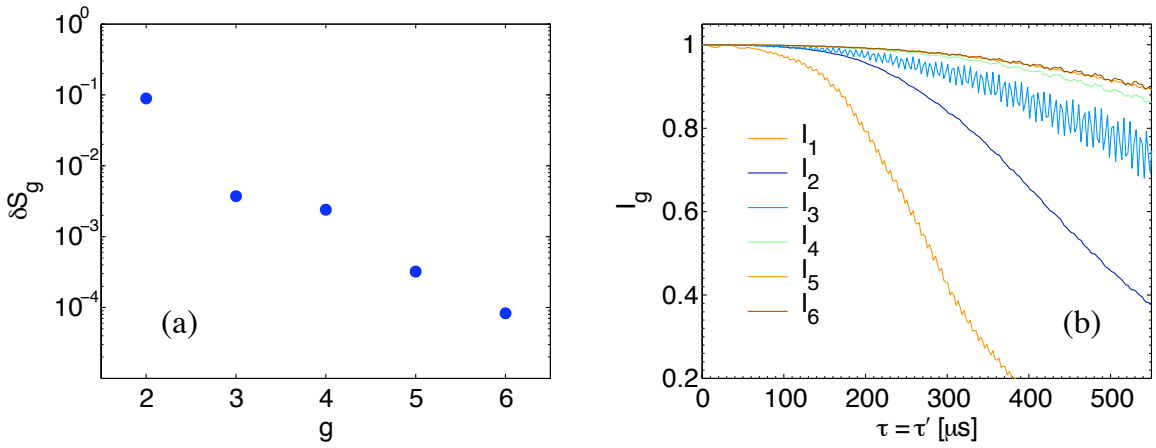

Figure 2.3: **Convergence analysis of the disjoint cluster method.** (a) Convergence: Equation (2.12) as the maximum number of nuclei g per group is increased. (b) Indicators I_g of the contribution of neglected pairs. When g is increased, the most important pair interactions are added to the pseudo spin relation S_g. The rest is used to calculate I_g.

Carbon-13 in a diamond lattice in a magnetic field of 50 Gauss oriented along the NV-axis. The algorithm was implemented using MATLAB and the Hamiltonian for each group was diagonalized exactly followed by the calculation of the corresponding unitary matrices for 6000 points from 0 to 1 ms. Each simulation of $S_g(\tau)$ takes approximately 10 min.

The method also shows good convergence. When the maximum size of subgroups g is increased, more interactions among nuclei are considered and the approximation gets better. As a figure of merit, we plot the integrated squared difference between consecutive spin-echo relations, S_g and S_{g-1},

$$\langle \delta S_g^2 \rangle = \frac{1}{T} \int_0^T \left[S_g(t) - S_{g-1}(t) \right]^2 dt. \tag{2.12}$$

Figure 2.3a shows $\frac{1}{2} \log \langle \delta S_g^2 \rangle$ up to $g = 6$. Each time the maximum size g of subgroups $\mathcal{C}_g^k$ is increased, the spin echo relations, S_g's, get closer.

In addition, following Ref. [58], we introduce the following indicator of all interactions not included in groups $\mathcal{C}_g^k$, and therefore in S_g,

$$I_g(\tau) = \prod_{\{n,m\}\epsilon\tilde{\mathcal{C}}_g} S_{nm}(\tau). \tag{2.13}$$

The product in Equation (2.13) runs over all neglected pair interactions contained in $\tilde{\mathcal{C}}_g$ and S_{nm} is calculated according to Equation (2.10). In this way, $I_g(\tau)$ has the next order of smallest couplings for a given spin bath distribution and is an indicator of convergence for our approach that obeys $0 \leq I_g(\tau) \leq 1$. When $I_g(\tau)$ is close to unity, good convergence is achieved. Figure 2.3b shows $I_g(\tau)$ for several aggregations (different g's). As expected, when the maximum subgroup size g is increased, the contribution from all neglected interactions is small. By the time the neglected interactions become important, the pseudo-spin $S_g(\tau)$ has already decayed (see Figure 2.2).

2.5 Results and Discussion

The results shown in Figure 2.4 clearly indicates that the electron spin echo signal cannot be modeled by just one time scale. This result can be understood by noting that few strongly interacting nuclei can coherently modulate the usual exponential decay. This is in good quantitative agreement with recent experimental results[27].

The random distribution of the spin bath and the relative high coupling between two nearest neighbor nuclei ($\sim$ 2 kHz) may cause a few nuclei to contribute significantly to the decay of the spin-echo signal. Nuclei that makes small contributions to the decoherence of the electron contribute as $1 - a\tau^4 \approx \exp(-a\tau^4)$ as it can be

seen from Equation (2.10). This behavior starts to deviate from $\exp(-a\tau^4)$ as the interaction between nuclei increases. Figure 2.4a shows a very unusual decay at which few nuclei modulate coherently (Fig. 2.4b, black curve) the irreversible contribution from the rest of the bath (Fig. 2.4b, red curve). Therefore, individual NV centers can show a rich variety of spin-echo signals with multiple time scales. The coherent modulation of the spin-echo diffusion due to strong interacting nuclei suggests that we can think about a system composed of the electron and these few strong interacting nuclei and an environment composed of the rest of the spin-bath.

Each NV center experiences a different random configuration and concentration of Carbon-13. This causes a large distribution of decoherence times T_2 when many centers are probed. In order to estimate the decoherence time T_2 we fit the envelope of $S_g(\tau)$ to $\exp\left(-(2\tau/T_2)^3\right)$. When the fit is not accurate we define T_2 as the longest time for which $S_g \geq 1/e$. Figure 2.5a shows the histogram of T_2 for 1000 different random distribution of Carbon-13 in the diamond lattices for an external magnetic field of 50 Gauss parallel to the NV-axis. Clearly, there exists substantial variation in T_2 for different centers.

As expected, the decoherence time decreases as the impurity concentration increases. This is shown in Figure 2.5b where T_2 goes as $1/n$. To understand this it is possible to make an analysis using a small τ expansion; while this is not always correct, it provides a simple explanation of the underlying behavior. From Equation (2.10), the decoherence time scales as the geometric mean of the bath dynamics and the bath-spin interaction, i.e.,

$$T_2 \sim \left(\bar{C}A_c\right)^{-1/2}, \tag{2.14}$$

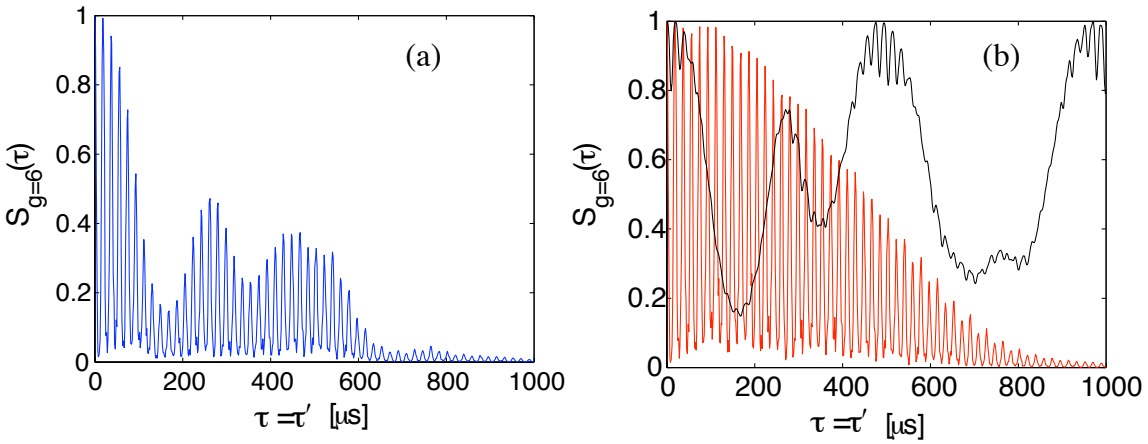

Figure 2.4: **Example of spin echo signal modulated by a pair of Carbon-13.** (a) Electron spin-echo signal highly modulated by a few Carbon-13 that strongly interact with the electron spin. (b) The strong contribution to the signal (black curve) has been isolated from the contribution from the rest of the spin bath (red curve).

where $\bar{C}$ is the averaged nuclear-nuclear dipolar interaction and A_c is some characteristic value for the electron-nuclear interaction. Here we can make a connection with phenomenological models and in particular with Equation (2.1). Free induction decay rates are proportional to the interaction between the central spin and the bath, $T_2^* \sim A_c^{-1}$. In turn, the correlation time of the nuclear bath is proportional to the dipole-dipole interaction between nuclear spins, $\tau_c \sim C^{-1}$. Combining the two times and Equation (2.14) leads to Equation (2.1).

Since both interactions, A and C, decay as r^{-3} and the average distance between bodies scales with the concentration as $n^{-1/3}$, both interactions scale linearly in n. Therefore, the decoherence time T_2 decreases approximately as

$$T_2 \propto 1/n. \tag{2.15}$$

For non-zero transverse magnetic fields, second order processes via the electron spin (see Appendix A.4) make a substantial contribution to decoherence. Even in

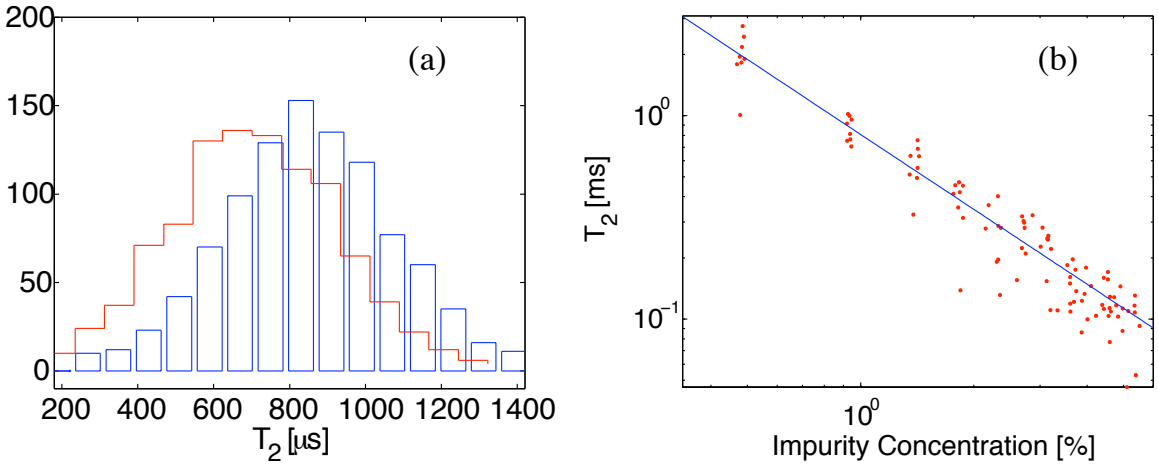

Figure 2.5: **Statistical behavior of spin echo signals for different lattice realizations.** Histogram of T_2 for 1000 simulations at a magnetic field of 50 Gauss at an angle of $\theta = 0°$ (blue) and $\theta = 6°$ (red) with respect to the NV-axis. (b) Decoherence time T_2 versus impurity concentration, Carbon-13, at 50 Gauss along the NV axis.

the case of non-interactig nuclei, Equation (2.8), a transverse magnetic field causes the revivals to diminish due to an enhanced nuclear g-factor experienced by nuclei nearby the electron (see Equation (A.55) in Appendix A.4). To understand this effect, consider that revivals occur because in each half of the spin-echo sequence each ^{13}C nuclear spin makes a full 2π Larmor precession (or multiples of it). Thus, in each half of the spin-echo sequence the accumulated Zeeman shift, due to the AC component of the ^{13}C nuclear field, cancels regardless of the initial phase of the oscillating field produced by the ^{13}C nuclear spins. The ^{13}C nuclear DC field component is refocused by spin-echo. However, if different nuclei precess at different Larmor frequencies, Ω_n^0, the accumulated Zeeman shifts for each nuclei cancels at different times and therefore the total accumulated Zeeman shift will be non-zero, preventing a complete refocusing of the electron spin. In addition, the average interaction between nuclei close to the electron spin is enhanced due to the enhancement of their g factors (see Equation

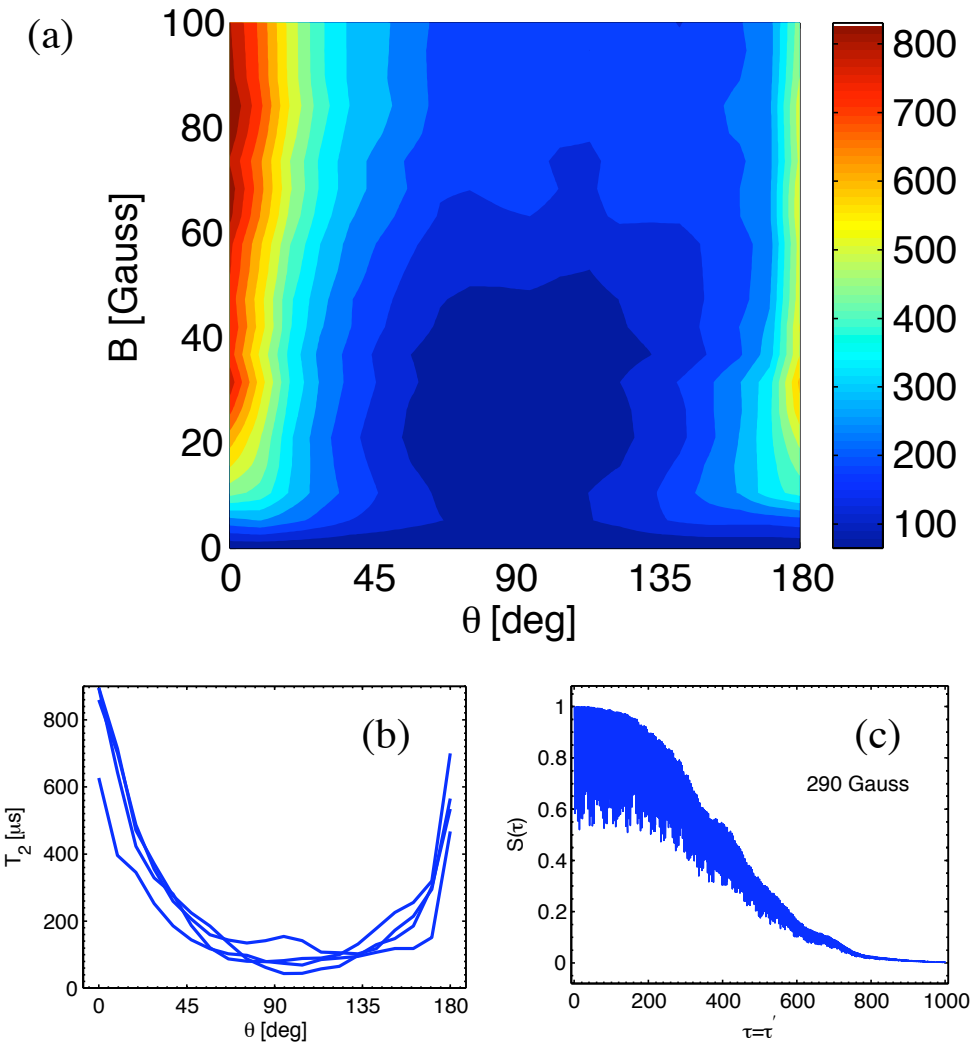

Figure 2.6: **Magnetic field magnitude and alignment dependence.** (a) Coherent time T_2 for different magnetic field strength and angles (measured from the NV-axis). Each point is average over 6 different random distributed baths. (b) Coherence time T_2 versus angle of the magnetic field for 4 different spin baths at 50 Gauss. (c) Pseudo spin $S_{g=6}(\tau)$ at 290 Gauss. At high fields the collapses due to the electron-nuclear dynamics decreases (see text).

(A.55) in Appendix A.4). These effects are illustrated in Figure 2.5a for a magnetic field at an angle of $\theta = 6°$ from the NV-axis and in Figure 2.6b.

As the angle between the magnetic field and the NV-axis, θ, is increased, the

electron-nuclear dynamics dominates and the spin-echo signal shows small revivals and fits poorly to a single exponential decay. Thus, to describe the coherence time at these angles, we have plot the average value of the signal, normalized by the average signal at $\theta = 0°$:[1]

$$T_2(B,\theta) \equiv T_2(B,\theta=0)\frac{\int_0^\infty |S_{B,\theta}(t)|dt}{\int_0^\infty |S_{B,\theta=0}(t)|dt} \ . \tag{2.16}$$

Figure 2.6a shows how the coherence of the signal varies with the strength and orientation of the magnetic field. This map is averaged over 6 different spin baths, since the random localization of Carbon-13 nuclei in the lattice makes the coherent time to vary from NV-center to NV-center as it can be seen in Figure 2.6b for a fixed magnetic field.

When the magnetic field along the NV-axis increases, the contribution from the electron-nuclear interactions decreases (see Figure 2.6c). This happens because the quantization axis for the nuclei points almost in the direction of the external magnetic field producing a small oscillating field. This can be easily seen in the non-interacting case, Equation (2.8), where the second term vanishes if $\mathbf{\Omega}_n^{(0)} \parallel \mathbf{\Omega}_n^{(1)}$. Similarly, when electron spin-echo is performed using the sub manifold $m_s = \{+1, -1\}$, the signal does not revive since each nuclei refocus the electron at different times. This occurs because the Larmor frequencies in this case, $\Omega_n^{\pm 1}$, are position dependent and differ for each nuclei.

We also point out that the approximation introduced in Section 2.2 is valid as long as the impurity concentration of Carbon-13 is not too high, so the neglected interac-

[1] We choose this approach as the signal has sufficiently non-trivial electron-nuclear dynamics for $\theta \neq 0$ that fitting an envelope decay function, as is done for $\theta = 0$, leads to large errors.

tions that connect different groups do not play an important role. This allows us to treat the bath as isolated groups. A heuristic argument to evaluate the validity of the present method is to consider the ratio between intra and inter group dipolar interations. We consider the root mean square (RMS) value of the dipolar interaction since the interaction itself average to zero due to its angular dependance when an isotropic distribution of nuclear spins is considered and due to the random initial spin configuration in the high temperature limit. The RMS contribution from a shell of spins is proportional to $I\left(r_{min}, r_{max}\right) = \left(\int_{r_{min}}^{r_{max}} r^{-6} 4\pi r^2 dr\right)^{1/2} = \left((4\pi/3)(r_{min}^{-3} - r_{max}^{-3})\right)^{1/2}$. Therefore, the ratio between intra and inter group interactions can be estimated as $I\left(r_{nn}, r_g\right)/I\left(r_g, R\right) \approx \left(r_g/r_{nn}\right)^{1/2}$, where r_{nn} is the nearest neighbor distance, r_g is the radius of the group that contains g nuclear spins and R is the radius of the spin bath. For a given concentration of Carbon-13 nuclei n, the number of nuclear spins g inside a sphere of radius r_g is $g = n \times 8 \times 4\pi(r_g/a)^3/3$, where a is the size of the unit cell which contains 8 Carbons. Under these considerations, the mentioned ratio is $\sqrt{g/nN_{nn}} \approx \sqrt{g/4n}$, where N_{nn} is the number of Carbons inside a sphere of radius r_{nn} for which we have assigned a conservative value of 4. For the concentration of Carbon-13 ($n \sim 1\%$), this ratio is much larger than one, supporting the validity of the current approximation. The approximation also relies on the relatively large interaction between the central spin (electron) and the bath, $\mathbf{A}_n$, when compared to the intra-bath interaction, $\mathbf{C}_{nm}$. The reason for this is that as the central spin gets disconnected from the bath (reducing $\mathbf{A}_n$), the decay occurs at later times τ and interactions of the order of τ^{-1} start to play a role. To illustrate this, consider the size of each subgroup scaling as $(g/n)^{1/3}$ where g is the size of the subgroup. Then, the

interaction between nearest neighbor groups scales as nC_{nn}/g where C_{nn} is the nearest neighbor nuclear interaction. The time at which this interaction is important goes as $t \sim g/nC_{nn} = g/\bar{C}$. If we require this time to be larger than the decoherence time ($t \gg T_2$), we find that the two types of interactions should satisfy $g\left(A_c/\bar{C}\right)^{1/2} \gg 1$ (for the present study this value is around 150). Therefore, when the interaction between the addressed spin and the bath is of the order of the intra-bath interactions, the approximation breaks down. This would be the case of the spin-echo signal for a nuclear spin proximal to the NV center[39] in which more sophisticated methods should be applied such as tree tensor networks[62].

2.6 Comparison with experiments

Many of the results presented in previous sections have been confirmed experimentally. In particular, Mizuochi et al.[66] confirmed the inverse proportionality dependence with the concentration of Carbon-13 (Equation 2.15). In addition, the measured and calculated values for the decoherence times agrees within 30%.

The dependence of T_2 on the angle θ between the magnetic field and NV-axis, described in Section 2.3.1 and Figure 2.6 has been confirmed by experiments performed by Paul Stanwix, My Linh Pham, and David Lesage in Ronald Walsworth's laboratory[32]. In addition, they measured the power n of the decay function,

$$E(\tau) \propto \exp -(\tau/T_2)^n. \tag{2.17}$$

As mentioned on Section 2.5, when the magnetic field is aligned with the NV axis, the decay is due to dipole-dipole interaction among Carbon-13's leading to a decay

with a power n varying between 3 and 4. Meanwhile, when the magnetic field is misaligned, the value for the decay should be around $n = 2$. THe measurements of Stanwix et al. agree with this analysis, finding higher values of n when the magnetic field is aligned with the NV axis and lower values of n when the magnetic field is at a non-zero angle. Interestingly, the values for n found at high angles are lower than values predicted by theory for a single NV center. This difference is due to an average effect present in ensemble measurements which is discussed as follow.

2.6.1 Ensemble measurements

In Section 2.3.1 we found that decoherence with an off axis magnetic field is primarily caused by one or two Carbon-13's nearby to the central NV spin. In an ensemble measurement, the strength of this interaction has a large variation since it is position dependent. For few NV centers in the ensemble, this interaction will be big, but for most NV centers it will be small. Therefore, it is necessary to average over the wide-ranging interactions experienced by all NVs in the ensemble to get the form of the measured echo signal[67, 68],

$$E(t) = \int f(b) \exp(-bt^2) db \tag{2.18}$$

where $f(b)$ is the probability distribution for having a value b of the NV-Carbon-13 interaction. From Section 2.3.1 we can approximate this value by the hyperfine interaction, A_k, between the nearest Carbon-13 nucleus and the central NV spin[67],

$$b = |A_k|^2. \tag{2.19}$$

In a cubic lattice with randomly distributed Carbon-13, this distribution is well approximated by (see Appendix A.3)

$$f_b(b) = 2b^{-3/2}\left(\frac{1}{\sqrt{b_{min}}} - \frac{1}{\sqrt{b_{max}}}\right). \tag{2.20}$$

where

$$b_{min} = \left(\frac{\mu_0}{4\pi}\gamma_e\gamma_n\right)^2 \frac{1}{r_{max}^6} \qquad b_{max} = \left(\frac{\mu_0}{4\pi}\gamma_e\gamma_n\right)^2 \frac{1}{a^6}. \tag{2.21}$$

Here, b_{min} is given by the size of the crystal (if very small) or the effective volume (r_{max}^3) we assign for the average Carbon-13 nucleus; and b_{max} is determined by the smallest distance between the nearest Carbn-13 nucleus and the central NV spin (set by the diamond lattice spacing a). If this probability distribution is used, we obtain the ensemble echo signals shown in Figure 2.7.

2.7 Conclusions

We have presented a method to evaluate the decoherence of a single spin in the presence of an interacting randomly-distributed bath. It properly incorporates the strong electron-nuclear dynamics present in NV centers and explains how it affects the decoherence. We also incorporates the dynamic beyond the secular approximation by including an enhanced nuclear g-factor that depend on the orientation of the external magnetic field relative to the NV-axis and by including an electron mediated nuclei interaction. Our results show that the spin echo signal for NV centers can present multiple time scales where the exponential decay produced by many small nuclei contributions can be coherently modulated by few strongly interacting nuclei. The

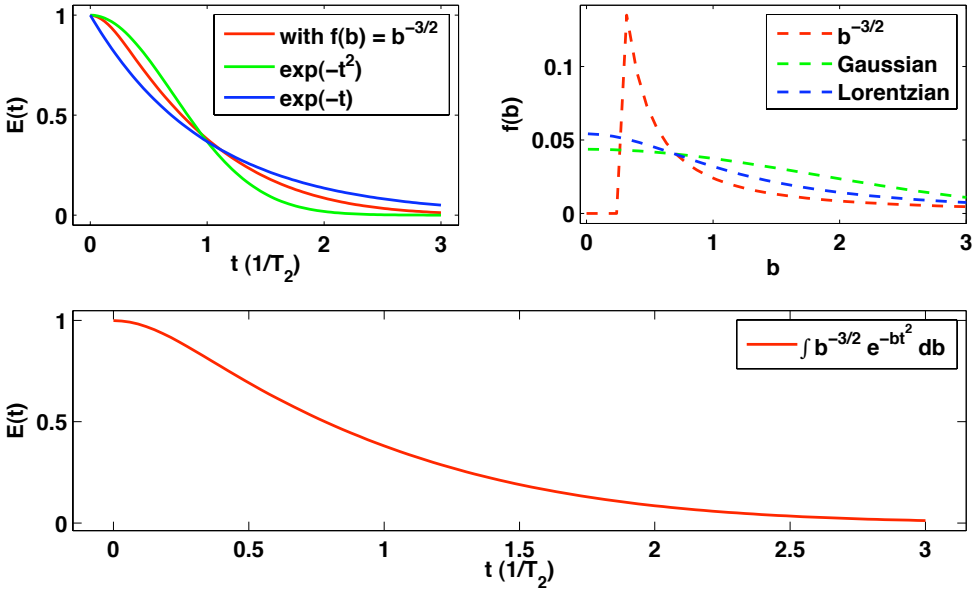

Figure 2.7: **Averaging individual distributions of the NV-Carbon-13 interaction.** a) Averaged signal (2.18) for several distributions $f(b)$. Note that the averaged signal obtained with $f(b) = b^{-3/2}$ looks like gaussian decay at short times but exponential decay at long times. b) Distributions $f(b)$ used to calculated the averaged signal in (a). c) Again averaged signal $E(t)$ using $f(b) = b^{-3/2}$ for better appreciation.

coherence times in ultra-pure diamond can be further improved by making isotopically pure diamond with low concentration in Carbon-13. This method may be used in other systems as long as the intra-bath interaction is smaller than the interaction between the central spin and the bath. These results have important implications, e.g., in magnetometry where long coherence times are important. For example, echo signals persisting for up to milliseconds can be used for nanoscale sensing of weak magnetic fields, as it was demonstrated recently[27].

Chapter 3

Magnetic field sensing with an individual electronic spin in diamond

3.1 Introduction

Sensitive solid-state magnetometers typically employ phenomena such as superconducting quantum interference in SQUIDs[34, 35] or the Hall effect in semiconductors[36]. Intriguing novel avenues such as magnetic resonance force microscopy (MRFM) are also currently being explored[37, 38]. Our approach to magnetic sensing[25] uses the coherent manipulation of a single quantum system, an electronic spin qubit. As illustrated in Figure 3.1, the electronic spin of an individual NV impurity in diamond can be polarized via optical pumping and measured through state-selective fluorescence. Conventional electron spin resonance (ESR) techniques are used to coherently ma-

nipulate its orientation. To achieve magnetic sensing we monitor the electronic spin precession, which depends on external magnetic fields through the Zeeman effect. This method is directly analogous to precision measurement techniques in atomic and molecular systems[42], which are widely used to implement ultra-stable atomic clocks[69, 70, 71] and sensitive magnetometers[72].

The principal challenge for achieving high sensitivity using solid-state spins is their strong coupling to the local environment, which limits the free precession time and thus the magnetometer's sensitivity. Recently, there has been great progress in understanding the local environment of NV spin qubits, including ^{13}C nuclear spins [51, 73, 53, 39, 74] and electronic spin impurities[75, 76, 77]. Here, we employ coherent control over a coupled electron-nuclear system[25, 53], similar to techniques used in magnetic resonance, to decouple the magnetometer spin from its environment. As illustrated in Figure 3.2, a spin-echo sequence refocuses the unwanted evolution of the magnetometer spin due to environmental fields fluctuating randomly on time scales much longer than the length of the sequence. However, oscillating external magnetic fields matching the echo period will affect the spin dynamics constructively, allowing sensitive detection of its amplitude.

The ideal preparation, manipulation and detection of an electronic spin would yield a so-called quantum-projection-noise-limited minimum detectable magnetic field[71]

$$\delta B_{min} \sim \frac{\hbar}{g\mu_B\sqrt{T_2 T}} \tag{3.1}$$

where T_2 is the electronic spin coherence time, T is the measurement time, μ_B is the Bohr magneton, $\hbar$ is Planck's constant, and $g \approx 2$ is the electronic Lande g-factor. In principle, for typical values of $T_2 \sim$ 0.1-1 milliseconds, sensitivity on the order of a few

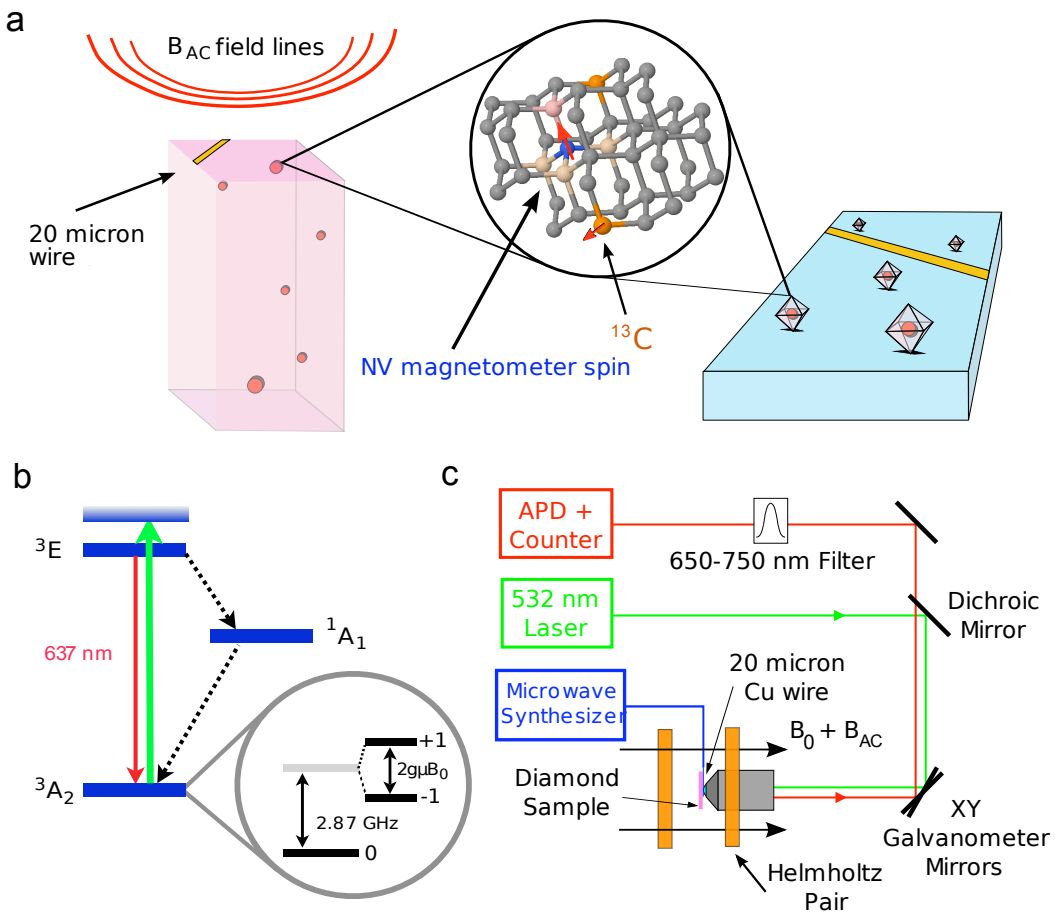

Figure 3.1: **Principles of the individual NV electronic spin diamond magnetic sensor.** (a) A single NV impurity proximal to the surface of an ultra-pure bulk single-crystal diamond sample (left) or localized within a diamond nano-crystal (right) is used to sense an externally-applied AC magnetic field (shown on the left). A 20 micron diameter wire generates microwave pulses to manipulate the electronic spin states (see Appendix B.3). (b) Level structure of the NV center. (c) Schematic of the experimental approach. Single NV centers are imaged and localized with ~ 170 nm resolution using confocal microscopy. The position of the focal point is moved near the sample surface using a galvanometer mounted mirror to change the beam path and a piezo-driven objective mount. A pair of Helmholtz coils are used to provide both AC and DC magnetic fields. Experiments are then performed on single NV centers as verified by photon correlations measurements.

nT/Hz$^{1/2}$ can be achieved with a single NV center. Although this is less sensitive than for state-of-the-art macroscopic magnetometers[33, 35], a key feature of our sensor is that it can be localized within a region of about ten nanometers, either in direct proximity to a diamond surface or within a nano-sized diamond crystal (Figure 3.1a). Sensitive magnetic detection on a nanometer scale can then be performed with such a system under ambient conditions. Figure 3.3 provides a comparison between magnetic field sensitivity and detector volume for several state-of-the-art magnetometers and the NV diamond systems demonstrated here.

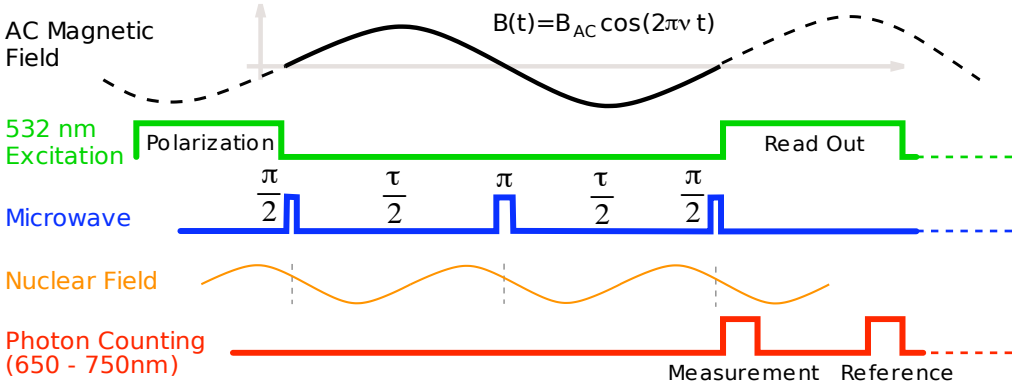

Figure 3.2: **Optical and microwave spin-echo pulse sequence used for sensing an AC magnetic field $B_{AC}(\tau)$.** An individual center is first polarized into the $m_S = 0$ sublevel. A coherent superposition between the states $m_S = 0$ and $m_S = 1$ is created by applying a microwave $\pi/2$ pulse tuned to this transition. The system freely evolves for a period of time $\tau/2$, followed by a π refocusing pulse. After a second $\tau/2$ evolution period, the electronic spin state is projected onto the $m_S = 0, 1$ basis by a final $\pi/2$ pulse, at which point the ground state population is detected optically via spin-dependent fluorescence. The DC magnetic field is adjusted to eliminate the contribution of the randomly phased field produced by ^{13}C nuclear spins (gold curve) by choosing $\tau = 2n/\omega_L$, for interger n.

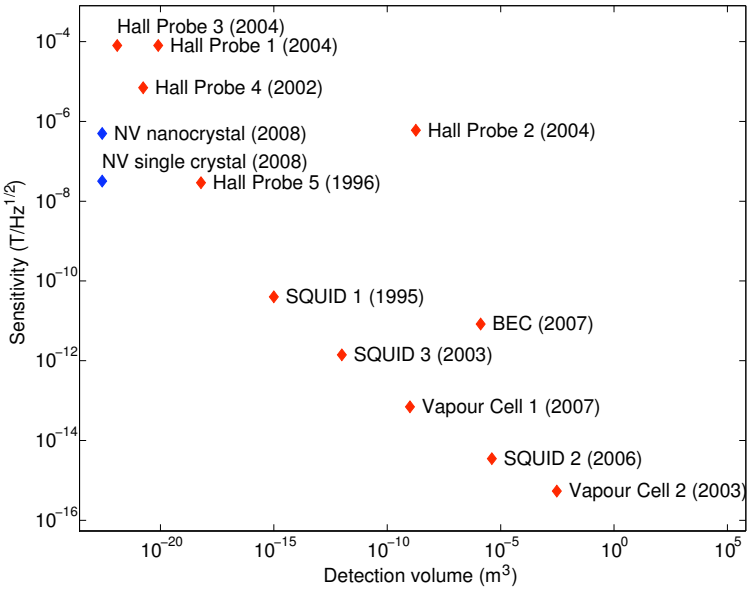

Figure 3.3: **Sensitivity versus detection volume for various kinds of magnetic sensors.** At cryogenic temperatures, SQUID 1-3[78, 79, 80]; at room temperature, Hall Probe 1-3[81, 82], BEC[83], NV nanocrystal (this work) and NV in ultra-pure diamond (projected from present bulk single-crystal studies); and at 100-200°C, Vapour Cell 1-2[84],[13].

3.2 Implementation of spin-based magnetometry using NV centers

To establish the sensitivity limits of a single electronic spin magnetometer, we carried out a series of proof-of-principle experiments involving single NV centers in bulk ultra-pure single crystal diamond and in commercially available diamond nanocrystals. Our experimental methodology is outlined schematically in Figure 3.1a; further detail about our experimental setup and diamond samples are given in Appendices B.1 and B.2. We first focus on the single crystal diamond bulk sample. Figure 3.4 shows a typical spin-echo signal observed from an individual NV center. The peri-

odic modulation of the echo is caused by a bath of spin-1/2 ^{13}C nuclei (1.1% natural abundance), which create an effective precessing magnetic field at the NV center of a few microtesla. In the presence of an applied static magnetic field B_{DC}, the periodic Larmor precession of the nuclear field causes the NV spin-echo signal to collapse and revive[53] at half the rate of the Larmor frequency of ^{13}C, $\omega_L = \gamma_{^{13}C} B_{DC}$, where $\gamma_{^{13}C}$ is the carbon gyromagnetic ratio. Note that substantial spin-echo revivals exist even after a free evolution of 0.6 ms. To detect an external AC magnetic field with the highest sensitivity, we must eliminate the contribution from the ^{13}C nuclear field. To this end, the revival rate of the spin-echo signal is adjusted by varying the strength of the applied DC magnetic field B_{DC}, such that the frequency of the echo revival peaks coincides with multiples of the AC field frequency ν to be detected.

As shown in Figure 3.5, the observed peak of the spin-echo signal varies periodically as the amplitude of the external AC field (B_{AC}) is increased. This signal variation results from phase accumulated by the NV spin due to the AC magnetic field and the resultant time varying Zeeman shift during the spin's precession; converting this phase into a spin population difference gives rise to variations in the detected fluorescence, which serves as the magnetometer signal. Note that the period of this signal oscillation depends on the spin-echo interval $\tau = 1/\nu$. For a given AC magnetic field strength B_{AC}, the phase accumulated by the electronic spin over one period will increase as the frequency of the external AC field decreases. At the conclusion of a single run of the magnetometry pulse sequence, the measurable spin-echo signal S_B is proportional to the probability of the NV spin being in the $m_S = 0$ state: $S_B \propto P_0(B_{AC}) = (1 + F(\tau)\cos(\delta\phi))/2$, where $\delta\phi = 4\gamma_e B_{AC}/2\pi\nu$ and $F(\tau)$

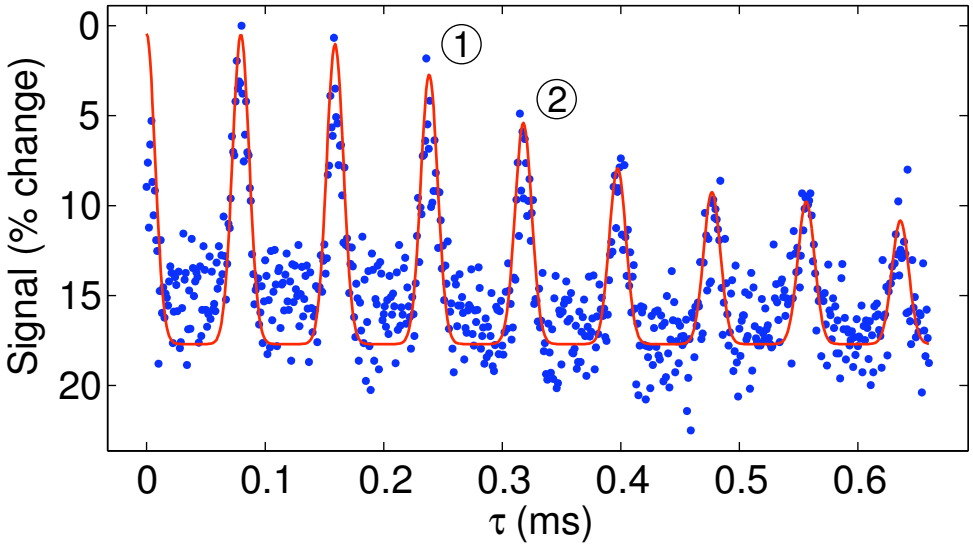

Figure 3.4: **Example electronic spin-echo measurement.** We plot the normalized echo signal corresponding to a fractional change of NV center fluorescence. Maximal signal corresponds to an average number of photons $\bar{n} = 0.03$ detected during the 324 ns photon counting window of a single experimental run. Collapses and revivals are due to interactions with a ^{13}C nuclear spin bath. The revivals occur at half the rate of the Larmor frequency of ^{13}C (here set by $B_{DC} = 22$ gauss). The spin-echo signal envelope was fitted with an exponential decay function modulated by a strongly interacting pair of nearby ^{13}C (for more information see Appendix B.4). Magnetometer sensitivity experiments are performed at spin-echo revival peaks to maximize signal.

is the amplitude of the spin-echo signal envelope in the absence of the external AC magnetic field (Figure 3.4).

The sensitivity of the NV magnetometer to small variations in B_{AC}, e.g., as depicted in the measurements shown in Figure 3.5, is given by $\delta B_{min} = \sigma_S^N / dS_B$, where σ_S^N is the standard deviation of the spin-echo measurement after N averages and dS_B is the slope of the spin-echo signal variation with B_{AC}. Since maximum sensitivity (i.e., smallest δB_{min}) occurs at maximum slope, all magnetometer sensitivity measurements were conducted at this point. This maximum slope is propor-

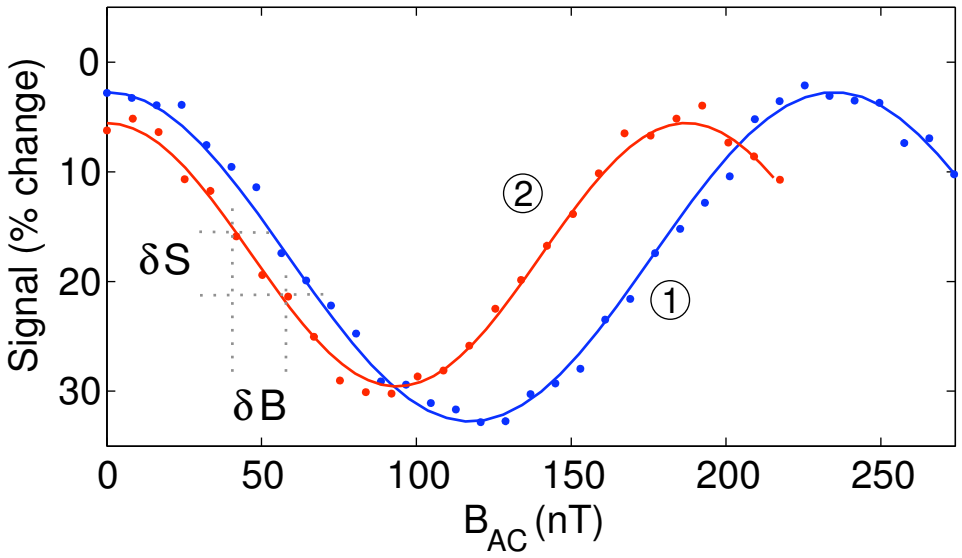

Figure 3.5: **Demonstration of spin-echo-based magnetometry with an individual NV electronic spin in a bulk diamond sample.** Examples of measured spin-echo signal as a function of applied AC magnetic field amplitude for two operating frequencies $\nu_1 = 3.15$ kHz (red) and $\nu_2 = 4.21$ kHz (blue), corresponding to revivals 1 and 2 indicated in Fig. 2a. Each displayed point is a result of $N = 7 \times 10^5$ averages of spin-echo sequences. The magnetometer is most sensitive to variations in the AC magnetic field amplitude (δB) at the point of maximum slope, with the sensitivity being limited by the uncertainty in the spin-echo signal measurement (δS). We note that the cosine behavior of the signal with respect to AC magnetic field amplitude can be changed to a sine by adjusting the phase of the third microwave pulse by 90 degrees. This change moves the point of maximum magnetometer sensitivity to near zero AC field amplitude.

tional to the spin-echo amplitude divided by the frequency of the oscillating field, $dS_B \propto F(1/\nu)/\nu$. For a shot-noise limited signal with uncertainty σ_S in a single measurement: $\sigma_S^N = \sigma_S/\sqrt{N}$, where $N = T/\tau$, T is the measurement time and τ is the length of the spin-echo sequence. Hence the magnetometer sensitivity is expected to scale as $\delta B_{min} \propto \sqrt{\nu}/F(1/\nu)$.

Figure 3.6a shows example measurements of the sensitivity δB_{min} after one second of averaging as a function of the AC magnetic field frequency $\nu = 1/\tau$. As this

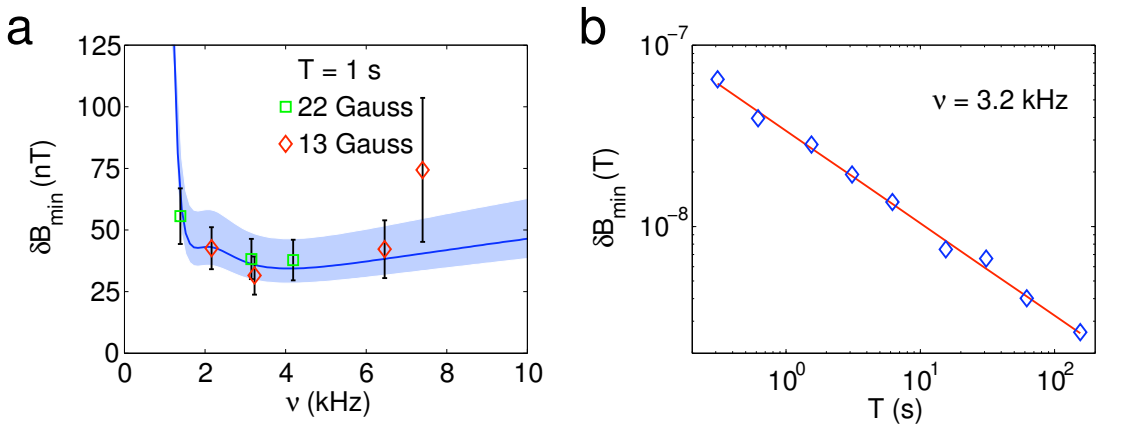

Figure 3.6: **Characterization of magnetometer sensitivity and minimum measurable AC magnetic field.** (a) Measured sensitivity of a single NV spin magnetometer in a bulk diamond sample over a range of frequencies for the external AC magnetic field after averaging for one second ($T = 1$ s). Error bars represent standard deviation (s.d.) for a sample size of 30. Also shown is the theoretically predicted sensitivity (solid blue line), with the shaded region representing uncertainty due to variations in photon collection efficiency (for more information see Appendix B.4). Measurements were carried out at two different DC fields, $B_{DC} = 13$ (in red) and 22 gauss (in green). (b) The minimum measurable AC magnetic field as a function of averaging time, for AC field frequency $\nu = 3.2$ kHz and $B_{DC} = 13$ gauss. Fit to this data (red curve) shows that the sensitivity improves as the square root of the averaging time and is consistent with theoretical estimates based on photon shot-noise limited detection.

frequency decreases, the accumulated Zeeman phase shift of the NV spin during one period increases. This makes the NV spin more sensitive to variations of B_{AC} as the frequency is reduced, until the point at which the NV spin decoheres during a single period of the external AC magnetic field's oscillation. This decoherence decreases the magnetometer's sensitivity by decreasing the contrast of the spin-echo signal ($F(1/\nu) \rightarrow 0$) and therefore the slope dS_B. At high frequencies or short times, $F(1/\nu) \rightarrow 1$, and the sensitivity scales as $\sqrt{\nu}$. Hence, the magnetometer sensitivity is optimized for frequencies comparable with the longest time for which

substantial echo signal is still observable. We note that it is possible to measure at higher frequencies without further loss of sensitivity by using multiple spin-echo pulses in a given measurement period [25]. Figure 3.6b shows examples of measured NV magnetometer sensitivity for a fixed AC magnetic field frequency ν as a function of measurement time T. The solid line is a fit to $\delta B_{min} \propto T^{-\alpha}$, where $\alpha = 0.5 \pm 0.01$, indicating that magnetic fields as small as few nanotesla are resolvable after 100 seconds of averaging.

As noted above, a key feature of our technique is that at specific times, determined by echo revivals, the NV electronic spin can be decoupled from ^{13}C nuclear spins to leading order. In practice, the decoupling is not perfect due to the internal dynamics of the electronic environment other than simple spin precession. In fact, the overall decay of the echo signal shown in Figure 3.4 does not follow the simple exponential decay associated with typical ESR on bulk samples. This can be understood by noting that the echo dynamics of a single NV center near its revivals is likely determined by a few nearby ^{13}C, which interact strongly with the electronic spin[73, 51, 53, 39, 85], yielding multiple characteristic time scales for echo decay (see Chapter 2 and Appendix B.4).

The absolute sensitivity of the NV magnetometer depends on the signal to noise ratio in the readout of the NV electronic spin state. In the present demonstration, this is limited by photon collection efficiency $\approx 0.1\%$. The resulting photon shot noise[33, 25] is about an order of magnitude larger than the ideal quantum projection noise limit given by Equation (3.1), resulting in a corresponding degradation of magnetometer sensitivity. Our theoretical prediction of magnetometer sensitivity (solid curve in Figure 3.6a) combines the NV coherence properties shown in Figure 3.4 with the

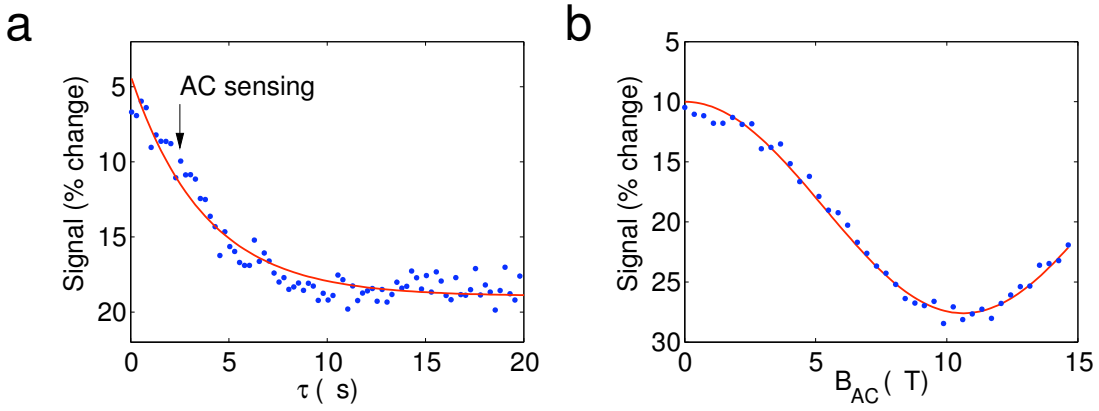

Figure 3.7: **Demonstration of magnetic sensing with a single NV electronic spin in a diamond nanocrystal.** (a) Example electronic spin-echo signal from a single NV center contained in a diamond nanocrystal with diameter of 34 ± 12 nm as determined by AFM. Maximum signal corresponds to an average number of photons $\bar{n} = 0.02$ counted during a 324 ns photon counting window. The arrow line indicates the time at which magnetic sensing is performed in Fig. 4b. (b) Example electronic spin-echo signal as a function of the applied AC magnetic field amplitude at a frequency of $\nu = 380$ kHz. For this data, $N = 2 \times 10^6$ averages of spin-echo sequences were used. The resulting standard deviation yields a magnetometer sensitivity of 0.5 ± 0.1 μT/Hz$^{1/2}$.

noise due to photon counting statistics and imperfect collection efficiency (for more information see Appendix B.4). This prediction is in excellent agreement with our experimental results, indicating that our magnetometer is photon-shot-noise limited.

3.3 Magnetic sensing using diamond nanocrystals

To demonstrate magnetic sensing within a nanoscale detection volume, we also performed similar experiments with single NV centers in diamond nanocrystals. We used commercially available nanocrystals that contain a large number of impurities, which shorten the electronic spin coherence time[86] to values ranging from 4 to 10

μs. Sensitive detection of AC magnetic fields is still possible as demonstrated experimentally in Figure 3.7. Here, the echo signal from a single NV center in a 30 nm size nanocrystal decays on the time scale of ~ 4 μs. The absence of characteristic collapses and revivals, associated with couplings to ^{13}C nuclear spins, indicates that the echo decay is likely due to other spin impurities such as paramagnetic substitutional nitrogen atoms containing unpaired electron spins. Magnetic sensing with such a nanocrystal at $\nu = 380$ kHz is demonstrated in Figure 3.7b. From these measurements we estimate a magnetometer sensitivity of $\delta B_{min} \sim 0.5 \pm 0.1$ μT/Hz$^{1/2}$ for this nanocrystal.

Improved magnetometer sensitivity for bulk and nanocrystal diamond may be achieved in several ways. By using isotopically pure diamond with low concentrations of both ^{13}C and nitrogen electron spin impurities, much longer coherence and interrogation times should be possible. For diamond nanocrystals, however, the ultimate sensitivity will eventually be limited by surface effects [76, 87]. Increases to the signal-to-noise ratio may also be possible by improving the measurement readout efficiency. Near single-shot readout of an electronic spin in diamond has been achieved with cryogenic cooling using resonant excitation[23]. Photon collection efficiency at room temperature can also be substantially improved using either conventional far-field optics or evanescent, near-field coupling to optical waveguides[88]. Finally, further improvements can likely be obtained by using magnetic sensing with multiple NV centers and by employing more complex pulse sequences[25].

3.4 Outlook and Conclusions

Our results demonstrate that electronic spins in diamond can be used for precision measurements of nanoscale magnetic fields. This approach opens a new regime of magnetic sensing, enabling detection of single electron and even nuclear spins separated from NV centers by a few tens of nanometers, see SI. For example, by combining our spin-echo based method with the recently demonstrated[28] transport and manipulation of nanocrystals using an atomic force microscope (AFM), a new kind of nanoscale scanning magnetic sensor may be created. Such a sensor could have a wide range of applications from biological and materials science to quantum information processing and fundamental tests of quantum mechanics. With the aid of field gradients, used for example in MRFM approaches[37, 38], NV diamond magnetometers may allow sensing and resolving of individual nuclear spins with applications in structural biology[25, 26]. It also provides an efficient method for measuring single electronic spins in various quantum computing architectures. Furthermore, this technique may allow non-destructive mapping of quantum states into NV centers, operating as a quantum magnetic "head" [89], with possibilities for mechanical transport of quantum information. Finally, we note that our technique could be used for detecting the quantum motion of magnetic mechanical resonators[90, 91], with new possibilities for creating nonclassical states of mechnical motion and for testing quantum mechanics on a macroscopic scale.

Chapter 4

Repetitive readout of a single electronic spin via quantum logic with nuclear spin ancillae

4.1 Introduction

Efforts have recently been directed towards the manipulation of several qubits in quantum systems, ranging from isolated atoms and ions to solid-state quantum bits [92, 93]. These small-scale quantum systems have been successfully used for proof-of-concept demonstrations of simple quantum algorithms [94, 95, 96, 97]. In addition, they can be used for potentially important practical applications in areas such as quantum metrology [92]. For example, techniques involving quantum logic operations on several trapped ions have been applied to develop an improved ion state readout scheme, resulting in a new class of atomic clocks [70, 98]. We demonstrate a

similar technique to enhance the readout of a single electronic spin in the solid state.

Our method makes use of quantum logic between a single electronic spin and nuclear spin qubits in its local environment for repetitive readout. While such nuclear spins are generally the source of unwanted decoherence in the solid-state, recent theoretical [99, 85, 100] and experimental [73, 39, 45, 77, 101, 102, 103] work has demonstrated that when properly controlled, the nuclear environment can become a very useful resource, in particular, for long-term quantum memory.

Our experimental demonstration makes use of a single negatively-charged nitrogen-vacancy (NV) center in diamond. The electronic ground state of this defect is an electronic spin triplet ($S = 1$) and is a good candidate for a logic qubit, on account of its remarkably long coherence times [104] and fast spin manipulation using microwave fields [105]. Furthermore, the center can be optically spin polarized and measured by combining confocal microscopy techniques with spin-selective rates of fluorescence [73]. In practice, the NV spin readout under ambient, room temperature conditions is far from perfect. This is because laser radiation at 532 nm for readout re-polarizes the electronic spin before a sufficient number of photons can be scattered for the state to be reliably determined.

4.2 Repetitive readout scheme

Our approach is to correlate the electronic spin logic qubit with nearby nuclear spins [106], which are relatively unperturbed by the optical readout, prior to the measurement process [74]. Specifically, we use one or more ^{13}C ($I = 1/2$) nuclear spins in the diamond lattice, coupled to the NV electronic spin via a hyperfine interaction,

as memory ancillae qubits. For example, a single ^{13}C nuclear spin has eigenstates $|\uparrow\rangle_{n_1}$ (aligned) or $|\downarrow\rangle_{n_1}$ (anti-aligned) with the local magnetic field. The composite electronic-nuclear system is first prepared in a fiducial state, $|0\rangle_e|\downarrow\rangle_{n_1}$, using a sequence of optical, microwave and radiofrequency (RF) pulses. Next, the electronic spin is prepared in an arbitrary state $|\Psi\rangle_e = \alpha|0\rangle_e + \beta|1\rangle_e$, where $|0,1\rangle_e$ denote electronic state with $m_s = 0, 1$. Before readout, we perform a sequence of gate operations resulting in the entangled electron-nuclear state $|\Psi\rangle_e |\downarrow\rangle_{n_1} \rightarrow \alpha |0\rangle_e |\downarrow\rangle_{n_1} + \beta |1\rangle_e |\uparrow\rangle_{n_1}$. The optical measurement process projects this state into either $|0\rangle_e |\downarrow\rangle_{n_1}$ or $|1\rangle_e |\uparrow\rangle_{n_1}$. When optically excited these two states fluoresce at different rates dependent on the value of m_S. Within a typical measurement period, less than one photon is counted before the electron spin is repolarized to $|0\rangle_e$, which indicates that the uncertainty of the electronic spin state measurement is quite large.

The nuclear spin can thus reveal the former electronic state because of the correlations established before the electronic spin was reset. To achieve this repetitive readout, we perform a controlled-not operation, which maps $|0\rangle_e |\downarrow\rangle_{n_1} \rightarrow |0\rangle_e |\downarrow\rangle_{n_1}$ and $|0\rangle_e |\uparrow\rangle_{n_1} \rightarrow |1\rangle_e |\uparrow\rangle_{n_1}$, and repeat the optical measurement. Fluorescence counting of these two states can be added to prior measurements to decrease the uncertainty for electronic spin state discrimination. If optical readout does not destroy the orientation of the nuclear spin, the uncertainty in the determination of the electronic spin can be reduced via repetitive measurements. In this way the overall signal-to-noise of the measurement process of our logic qubit can be increased. After multiple readout cycles and many quantum logic operations, the nuclear spin orientation will finally be destroyed. However, it is possible to further improve the readout scheme by using

a pair of ancillary nuclear spins and imprinting the electronic state into a GHZ-like state $|\Psi\rangle_e |\downarrow\rangle_{n_1} |\downarrow\rangle_{n_2} \rightarrow \alpha |0\rangle_e |\downarrow\rangle_{n_1} |\downarrow\rangle_{n_2} + \beta |1\rangle_e |\uparrow\rangle_{n_1} |\uparrow\rangle_{n_2}$. In such a case, the state of the first nuclear spin after repetitive readout sequences can be periodically "refreshed" using the information stored within the second nuclear spin. These schemes are closely related to a quantum non-demolition (QND) measurement [107, 108], as the nuclear spin population operators $\hat{I}_z^{n1,n2}$ do not evolve throughout the electronic spin readout and constitute "good" QND observables. While imperfect optical NV electronic spin detection precludes an ideal QND measurement, our scheme nevertheless allows substantial improvement in the spin readout.

4.3 Implementation with nearby ^{13}C ancillae

To implement the repetitive readout technique we use a single NV center in diamond coupled to nearby ^{13}C nuclear spins. These nuclear spins can be polarized, fully controlled and provide a robust quantum memory even in the presence of optical radiation necessary for electronic spin-state readout [39, 74]. This is achieved through a combination of optical, microwave, and RF fields (Figure 4.1) and discussed in Appendix C.1.

To control a single nuclear spin, we choose a NV center with a well-resolved ^{13}C hyperfine coupling near 14 MHz. The degeneracy of the $|m_s = \pm 1\rangle_e$ spin states is lifted by applying a $B_0 = 30$ gauss magnetic field along the NV axis. Under these conditions, the transitions of the electronic spin (**e**) within the subspace of $\{|0\rangle_e, |1\rangle_e\}$ can be selectively addressed, conditioned on a certain nuclear state. The

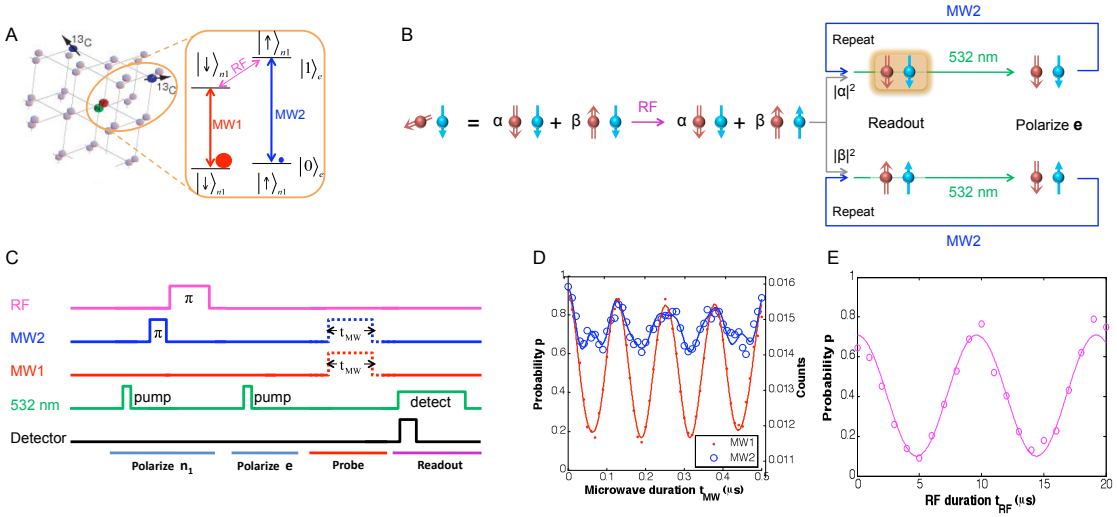

Figure 4.1: **Repetitive readout of an electronic spin.** (**A**) Illustration of the NV center and its proximal ^{13}C nuclear spins. Inset: Energy levels of the coupled spin system formed by the NV electronic spin (**e**) and the first proximal ^{13}C nuclear spin ($\mathbf{n}_1$). With a static magnetic field applied along the NV axis, spin $\mathbf{n}_1$ keeps the same quantization axis when spin **e** is $|0\rangle_e$ or $|1\rangle_e$ (see Appendix C.2). When spin $\mathbf{n}_1$ is $|\downarrow\rangle_{n_1}$ (or $|\uparrow\rangle_{n_1}$), the microwave field MW1 (or MW2) resonantly drives spin **e** between $|0\rangle_e$ and $|1\rangle_e$, which can implement the $\mathrm{C}_{n_1}\mathrm{NOT}_e$ gate. When spin **e** is $|1\rangle_e$, the radio-frequency RF field resonantly drives spin $\mathbf{n}_1$ between $|\downarrow\rangle_{n_1}$ and $|\uparrow\rangle_{n_1}$, which can implement the $\mathrm{C}_e\,\mathrm{NOT}_{n_1}$ gate. (**B**) Illustration of repetitive readout. The red down (up) arrow represents the electronic spin state $|0\rangle_e$ ($|1\rangle_e$), and blue down (up) arrow represents the nuclear spin state $|\downarrow\rangle_{n_1}$ ($|\uparrow\rangle_{n_1}$). (**C**) Experimental pulse sequences that polarize spin $\mathbf{n}_1$ to $|\downarrow\rangle_{n_1}$ and spin **e** to $|0\rangle_e$, followed by various probe operations, before fluorescence readout of spin **e**. (**D**) Measured electronic spin Rabi oscillations driven by MW1 and MW2 fields, for polarized spin $\mathbf{n}_1$. The small wiggles for MW2 are due to off-resonant driving of the majority population in the $|\downarrow\rangle_{n_1}$ state. The data is in agreement for finite detunings and microwave power (solid curves). The right vertical axis shows the average counts for a single readout. The left vertical axis shows the probability in the $|0\rangle_e$ state, obtained from the average counts (see Appendix C.1). (**E**) Measured nuclear spin Rabi oscillation driven by the RF field.

model Hamiltonian for this system (Figure 4.1A) is,

$$H = (\Delta + \gamma_e B_0)\hat{\mathcal{S}}_z + \gamma_C B_0 \hat{I}_z^{n1} + A\hat{\mathcal{S}}_z\hat{I}_z^{n1} \tag{4.1}$$

where $\Delta = 2\pi \times 2.87$ GHz is the zero field splitting, A is the hyperfine interaction,

and γ_e and γ_C are the electronic and nuclear spin gyromagnetic ratios. $\hat{\mathcal{S}}_z = \frac{1}{2}\hat{\mathbf{1}} + \hat{S}_z$ is a pseudo-spin one-half operator for the electronic spin subspace, $\hat{\mathbf{1}}$ is the identity matrix, and $\hat{I}_z^{n1}$ and $\hat{S}_z$ are the spin 1/2 angular momentum operators. Coherent oscillations between the $|0\rangle_e$ and $|1\rangle_e$ states, conditioned on a single proximal nuclear spin ($\mathbf{n}_1$) in $|\downarrow\rangle_{n_1}$ (or $|\uparrow\rangle_{n_1}$), are selectively driven by the microwave field MW1 (or MW2). To control nuclear spin $\mathbf{n}_1$ a resonantly tuned RF field to address the levels $|1\rangle_e|\downarrow\rangle_{n_1}$ and $|1\rangle_e|\uparrow\rangle_{n_1}$, which are energetically separated due to the hyperfine interaction (Figure 4.1A), is used.

Following the initialization of spin $\mathbf{e}$, spin $\mathbf{n}_1$ is polarized by applying MW1 and RF π pulses, which transfers the polarization from spin $\mathbf{e}$ to spin $\mathbf{n}_1$. Rabi oscillations of spin $\mathbf{n}_1$ are demonstrated (Figure 4.1E) by preparing spin $\mathbf{e}$ in the $|1\rangle_e$ state irrespective of the state of spin $\mathbf{n}_1$ (using MW1 and MW2 π-pulses) and increasing the RF pulse length.

This data indicates that we can achieve spin $\mathbf{n}_1$ preparation (polarization) and readout with combined fidelity $F \equiv \langle\downarrow|\rho'|\downarrow\rangle \geq 75\%$, where ρ' is the reduced density operator for spin $\mathbf{n}_1$.

We now turn to the demonstration of the repetitive readout technique. As illustrated in Figure 4.1D, the direct readout of electronic spin is imperfect. We define n^0 and n^1 as the total number of photons detected for the $|0\rangle_e$ and $|1\rangle_e$ states, respectively, during a single measurement interval. The signal is defined as the difference in average counts between the two spin states: $A_0 = n^0 - n^1 \approx 0.005$ (Figure 4.1D). Experimentally, photon shot-noise dominates the fluctuations in the counts. Because of this shot noise and the low average count ($n^0 \approx 0.016$), we need to average over

$N \sim 10^5$ experimental runs to obtain the data in Figure 4.1D.

To improve the signal, we use two spins: $\mathbf{e}$ and $\mathbf{n}_1$. Both spins are first polarized to the initial state $|0\rangle_e |\downarrow\rangle_{n_1}$. Next, we perform a unitary operation $U(t)$, which prepares the superposition state $|\Psi_1\rangle = (\alpha |0\rangle_e + \beta |1\rangle_e) |\downarrow\rangle_{n_1}$ that we would like to measure. Instead of immediately reading out the electronic spin, we use a controlled-not gate ($\mathrm{C}_e\mathrm{NOT}_{n_1}$, achieved by an RF π pulse) to correlate spin $\mathbf{e}$ with spin $\mathbf{n}_1$(Figure 4.2A). We then optically readout/pump spin $\mathbf{e}$, leaving the spin system in the post-readout state: $\rho_{\mathrm{post}} = |0\rangle\langle 0|_e \otimes \left(|\alpha|^2 |\downarrow\rangle\langle\downarrow| + |\beta|^2 |\uparrow\rangle\langle\uparrow|\right)_{n_1}$. The state of spin $\mathbf{n}_1$ via the electronic spin $\mathbf{e}$ by performing a controlled-not operation ($\mathrm{C}_{n_1}\mathrm{NOT}_e$, achieved by an MW1 or MW2 π pulse) is then readout. This completes a one-step readout of spin $\mathbf{n}_1$, which can be repeated.

As a direct illustration of the enhanced readout technique, Figure 4.2C shows the accumulated signal for Rabi oscillations of the electronic spin obtained by adding M subsequent repetitive readouts for each experimental run. This procedure results in a ten-fold enhancement of spin signal amplitude.

In order to further quantify the performance of this technique, the noise added with each additional repetitive readout must be considered. The repetitive readout spin signal is defined as a weighted sum of difference counts A_m associated with mth readout: $S_w(M) = \sum_{m=1}^{M} w_m A_m$. The average values of A_m are determined experimentally by measuring the difference in average counts associated with Rabi oscillations for each m-th repeated readout. The w_m allow us to weight the contribution of each repetitive readout to the overall signal. The noise corresponding to the repetitive readout signal is $\Delta S_w(M) = \sqrt{\sum_{m=1}^{M} w_m^2 \sigma_m^2}$. Here σ_m is the uncertainty of

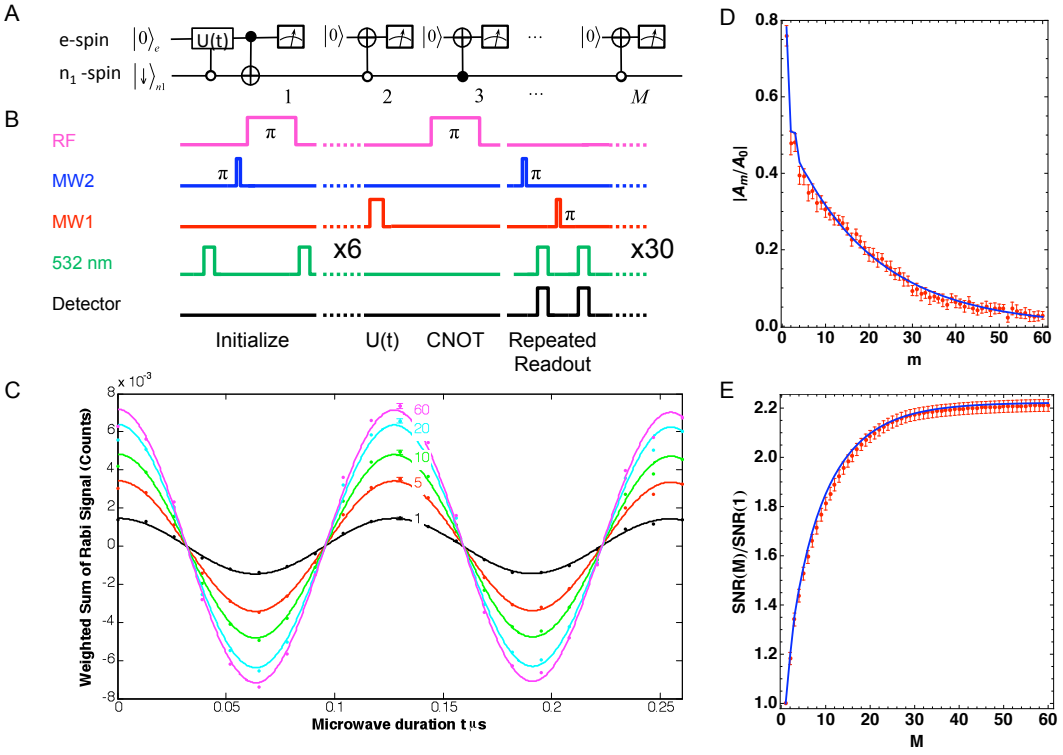

Figure 4.2: **Realization of repetitive readout.** (**A**) Quantum circuit for M-step repetitive readout scheme assisted by spin $\mathbf{n}_1$. (**B**) Operations and pulse sequences for $M = 60$. The initial state $|0\rangle_e |\downarrow\rangle_{n_1}$ is prepared with six-step pumping of spins $\mathbf{e}$ and $\mathbf{n}_1$. The MW1 pulse of duration t induces the Rabi rotation $U(t)$ of spin $\mathbf{e}$, whose parity information is imprinted to spin $\mathbf{n}_1$ with an RF π pulse (i.e., the $\mathrm{C}_e\mathrm{NOT}_{n_1}$ gate). After fluorescence readout of spin $\mathbf{e}$, $(M-1)$-repetitive readouts of spin $\mathbf{n}_1$ are performed by MW1 or MW2 π pulses (i.e., $\mathrm{C}_{n_1}\mathrm{NOT}_e$ gates) followed by fluorescence readout. Note the m=1 readout is not preceded by a MW1 pulse. (**C**) Cumulative signal obtained from repetitive readout measurements, summed from $m = 1$ to M, for $M = 1, 5, 10, 20, 60$ repetitions. Constant background counts are subtracted. (**D**) Amplitudes $|A_m|$ for Rabi oscillation measurements obtained from the m-th readout normalized to the signal amplitude without repetitive readout (A_0). (**E**) Improvement in SNR using the repetitive readout scheme. Blue curves in (D) and (E) are simulations with imperfection parameters estimated from independent experiments (see Appendix C.5).

the measurement of A_m. Experimentally, this uncertainty is found to be independent of m.

The signal-to-noise figure of merit is defined as $SNR(M) = S_w(M)/\Delta S_w(M)$. The w_m weights are chosen by noting that the larger values of A_m allow us to extract more information given the fixed uncertainty of each measurement, and we should emphasize these readouts more. As proven in Appendix C.4, the optimal choice of weights corresponds to $w_m = |A_m|/\sigma_m^2$ and the optimized SNR is given by:

$$\mathrm{SNR}_{opt}(M) = \sqrt{\sum_{m=1}^{M} \left| \frac{A_m}{\sigma_m} \right|^2} \tag{4.2}$$

In the ideal QND case, each repetitive readout would yield the same $|A_m|$ and the SNR would scale with $\sqrt{M}$. For our experiment, the SNR saturates (Figure 4.2E) due to the decay of the normalized amplitudes (Figure 4.3D). Nevertheless, the experimental data shown in Figure 4.2E indicate the enhancement of SNR by more than 220%.

In assessing this result, it is noted that various imperfections can affect the repetitive readout, which leads to the imperfect first readout $|A_1|\,/\,|A_0| < 1$, the sharp decrease in $|A_2|$, and the subsequent exponential reduction $|A_m| = |A_2|\eta^{(m-2)}$ with $\eta \approx 0.95$.

These behaviors can be attributed to three major imperfections (see Appendix C.5): errors from microwave pulses (about 7% error probability for each π pulse); imperfect optical pumping of the electronic spin after each readout; and most substantially, the depolarization of the nuclear spin memory under optical illumination

To quantify the latter process, we study the decay times for ^{13}C nuclear spins in the presence of optical illumination. For an illumination time t_L longer than 1 μs, the nuclear spin polarization decays exponentially, with a characteristic time $\tau_{n_1} = 13\,(1)$ μs (Figure 4.3B). Since τ_{n_1} is much longer than the time for optical readout and optical spin polarization of the NV electronic spin (350 ns), repetitive readout of **e**

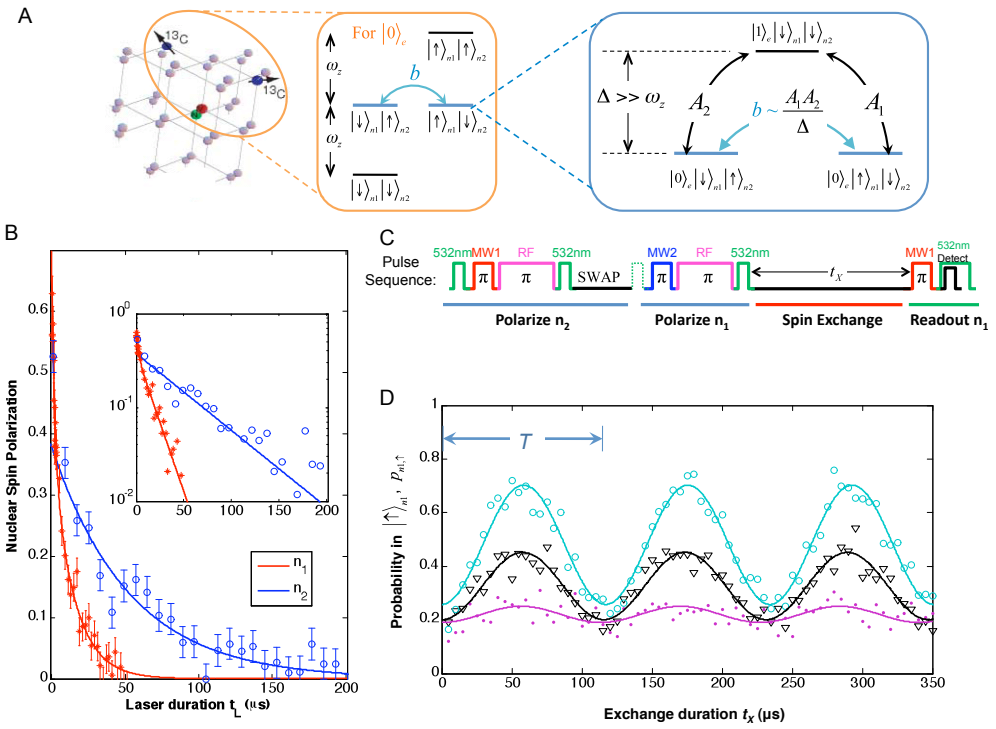

Figure 4.3: **Coherence and control of two nuclear spins.** (**A**) The coupled spin system formed by the NV electronic spin (**e**) and two proximal ^{13}C nuclear spins ($\mathbf{n}_1$ and $\mathbf{n}_2$). Middle inset: Energy levels for spins $\mathbf{n}_1$ and $\mathbf{n}_2$ when spin **e** is in the $|0\rangle_e$ state. Right inset: Schematic of flip-flop between spins $\mathbf{n}_1$ and $\mathbf{n}_2$, which is electron-mediated by the second-order hopping via $|1\rangle_e |\downarrow\rangle_{n_1} |\downarrow\rangle_{n_2}$. (**B**) Measured depolarization of spins $\mathbf{n}_1$ and $\mathbf{n}_2$ under optical illumination. For the duration of optical illumination t_L longer than 1 μs, the polarizations for spins $\mathbf{n}_1$ and $\mathbf{n}_2$ decay exponentially with characteristic times $\tau_{n_1} = 13\,(1)$ μs and $\tau_{n_2} = 53\,(5)$ μs, respectively. For t_L less than 1 μs, the decay is slightly faster, which is likely associated with dynamics of the spin-fluctuator model that describe optically induced depolarization of single nuclei (see ref. [74] and Appendix C.5). These decay times are much longer than the optical readout/pump time of the electronic spin (about 350 ns). Inset: Log-linear plot. (**C**) Operations and pulse sequence to probe dynamics between spins $\mathbf{n}_1$ and $\mathbf{n}_2$. (**D**) Measured spin flip-flop dynamics between spins $\mathbf{n}_1$ and $\mathbf{n}_2$. For three different preparations of the initial state ($|\downarrow\rangle_{n_1} |\uparrow\rangle_{n_2}$ (cyan), $|\downarrow\rangle_{n_1}$ and n_2 in thermal state (black), and $|\downarrow\rangle_{n_1} |\downarrow\rangle_{n_2}$ (purple)), the observed population, $p_{n_1,\uparrow}(t)$, oscillates with the same period $T = 117\,(1)$ μs. These observations verify the theoretical prediction, with flip-flop coupling strength $b = 4.27\,(3)$ kHz.

is possible. (In the absence of optical illumination, the ^{13}C nuclear spin decay times are $\gg 1$ ms [73, 39].) Despite the relatively long τ_{n_1}, after many cycles the nuclear spin depolarizes. This degrades the repetitive optical readout for larger m, yielding the overall exponential decay in the amplitude $|A_m|$ with increasing m (see Appendix C.4).

As an indication of how this limit can be circumvented, the use of two ancillary nuclear spins is considered. The state of spin $\mathbf{e}$ may be correlated with a more distant spin $\mathbf{n}_2$, in addition to proximal spin $\mathbf{n}_1$. As the decay time of spin $\mathbf{n}_2$ is longer than that of spin $\mathbf{n}_1$ due to a weaker interaction with spin $\mathbf{e}$, the information stored in spin $\mathbf{n}_2$ persists after spin $\mathbf{n}_1$ has been depolarized under optical illumination. This remaining $\mathbf{n}_2$ polarization can then be transferred to spin $\mathbf{n}_1$ and repetitively readout again.

Control of two nuclear spins is achieved by using the strongly coupled nuclear spin $\mathbf{n}_1$ as a probe for the second nearby ^{13}C nuclear spin $\mathbf{n}_2$, which cannot be directly observed via the NV center. By placing the NV electronic spin in $|0\rangle_e$ state, the hyperfine coupling is removed. This enables proximal ^{13}C nuclear spins with similar Zeeman energy to flip-flop and exchange spin population. Figure 4.3D shows that the nuclear population, $p_{n_1,\uparrow}(\tau)$, oscillates between $p_{n_1,\uparrow}(0) \approx 0.2$ and $p_{n_1,\uparrow}(T/2) \approx 0.5$ with a period of $T = 117\,(1)$ μs (Figures 3A & 3C). The relatively high contrast of these oscillations suggests an interaction with a second nuclear spin ($\mathbf{n}_2$), as the two nuclei "flip-flop" between the states $|\uparrow\rangle_{n_1}|\downarrow\rangle_{n_2}$ and $|\downarrow\rangle_{n_1}|\uparrow\rangle_{n_2}$. Such excitation exchange requires a similar Zeeman splitting for the two spins, indicating that the second nucleus is also a ^{13}C. We note that the nuclear spin-spin interaction strength

determined by our measurements, $b = \pi/T = 4.27\,(3)$ kHz, is several times that of a bare dipolar coupling (2 kHz for two ^{13}C nuclei separated by the nearest neighbor distance, 1.54 $\mathring{A}$) signifying that their interaction is mediated by the NV electronic spin (see inset of Figure 4.3A and Appendix C.2), which is described by the interaction hamiltonian $H_{int} = b(I_{1+}I_{2-} + I_{1-}I_{2+})$. This interaction can be used to effectively control the state of the second nucleus and of the entire three-spin system. Specifically, a half period of nuclear spin oscillation, $T/2$, constitutes a SWAP operation between the two nuclear spins. This operation can be used, e.g., to polarize the second nuclear spin (Figures 3C, 3D). In addition, by modifying the initial state of spin $\mathbf{n}_1$, we can prepare the initial state of the two nuclei in any of the four possible configurations: $\{\uparrow\uparrow, \uparrow\downarrow, \downarrow\uparrow, \downarrow\downarrow\}$ (see Appendix C.2). Further control is provided by putting the electronic spin into the $|1\rangle_e$ state, in which case the flip-flop dynamics between spins $\mathbf{n}_1$ and $\mathbf{n}_2$ disappears (see Figure C.3). This is because spins $\mathbf{n}_1$ and $\mathbf{n}_2$ typically have very distinct hyperfine splittings that introduce a large energy difference ($\Delta E \gg b$) between $|\uparrow\rangle_{n_1}|\downarrow\rangle_{n_2}$ and $|\downarrow\rangle_{n_1}|\uparrow\rangle_{n_2}$ and quench the interaction. Therefore, we can implement a controlled-SWAP operation between spins $\mathbf{n}_1$ and $\mathbf{n}_2$, enabling full control over spin $\mathbf{n}_2$. We further observe that spin $\mathbf{n}_2$ has decay time $\tau_{n_2} = 53\,(1)$ μs (Figure 4.3B inset) under optical illumination. Compared with spin $\mathbf{n}_1$, spin $\mathbf{n}_2$ is less perturbed by the optical transitions between different electronic states, as it has a weaker hyperfine coupling to the electron [74].

To demonstrate concatenated readout experimentally, both nuclear spins are initialized in the state $|\downarrow\rangle_{n_1}|\downarrow\rangle_{n_2}$ and a single NV electronic spin that we would like to detect is prepared in a superposition state $(\alpha|0\rangle + \beta|1\rangle)_e$. First, the operation

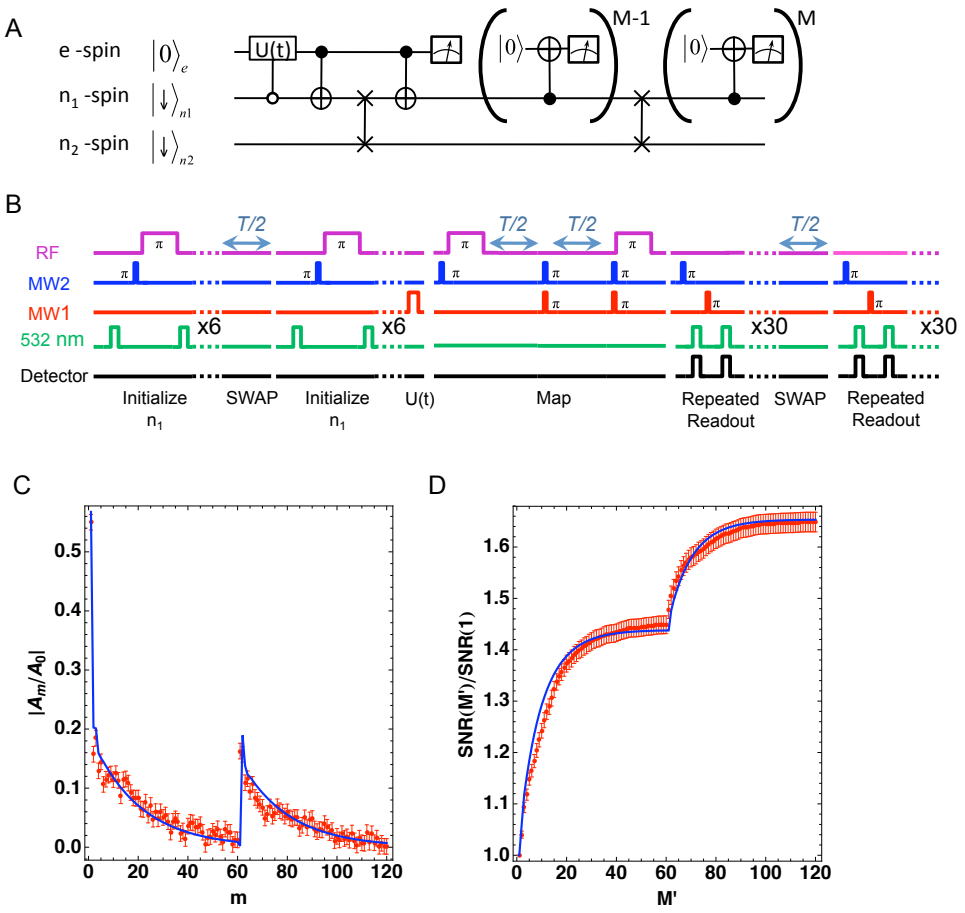

Figure 4.4: **Demonstration of two-level concatenated readout procedure.** (**A**) Quantum circuit for concatenated M-step repetitive readout scheme assisted by both spins $\mathbf{n}_1$ and $\mathbf{n}_2$. (**B**) Operations and pulse sequences for $M = 60$. Ideally, the GHZ-like state $\alpha\,|0\rangle_e\,|{\downarrow}\rangle_{n_1}\,|{\downarrow}\rangle_{n_2} + \beta\,|1\rangle_e\,|{\uparrow}\rangle_{n_1}\,|{\uparrow}\rangle_{n_2}$ with the parity information of spin **e** imprinted on both spins $\mathbf{n}_1$ and $\mathbf{n}_2$ is created before the first readout. After the first round of M-step repetitive readout, spin $\mathbf{n}_1$ is depolarized, but spin $\mathbf{n}_2$ maintains its polarization. The spin state of spin $\mathbf{n}_2$ is swapped to spin $\mathbf{n}_1$, which is then detected during the second round of M-step repetitive readouts. (**C**) Normalized amplitude $|A_m|\,/\,|A_0|$ obtained from the m-th readout. (**D**) Measured improvement in the SNR using the double repetitive readout scheme. The blue curves in (C) and (D) are simulations with imperfection parameters estimated from independent experiments (see Appendix C.5).

($C_e NOT_{n_1}$-SWAP-$C_e NOT_{n_1}$) is used to prepare the GHZ-type state $|\Psi\rangle = \alpha\,|0\rangle_e\,|\downarrow\rangle_{n_1}\,|\downarrow\rangle_{n_2}$ $+\ \beta\,|1\rangle_e\,|\uparrow\rangle_{n_1}\,|\uparrow\rangle_{n_2}$. Next, we optically readout/pump spin **e**, leaving the system in state $\rho'_{\text{post}} = |\alpha|^2\,|0\downarrow\downarrow\rangle\langle 0\downarrow\downarrow| + |\beta|^2\,|0\uparrow\uparrow\rangle\langle 0\uparrow\uparrow|$. $M-1$ repetitive readouts of spin $\mathbf{n}_1$ are then performed, in the manner described above, until spin $\mathbf{n}_1$ is depolarized. At this point, spin $\mathbf{n}_2$ is still directly correlated with the first measurement of the **e** spin. This information can be transferred to spin $\mathbf{n}_1$ by a nuclear SWAP gate. Thus, the parity information can be measured again by performing a second round of M-step repetitive readout. These operations are summarized in the quantum circuit (Figure 4.4A) and pulse sequences (Figure 4.4B).

Experimentally, the "revival" in the signal amplitude $|A_m|$ after the SWAP is demonstrated (Figure 4.4C), which leads to an associated jump in the SNR curve (Figure 4.4D) for $M' = 61$. This shows that the second nuclear spin can be used to further enhance the readout efficiency. While ideally the repetitive readout scheme assisted by two nuclear spins should improve the absolute SNR more than a single nuclear spin, in the present experimental realization this is not yet so, as more errors are accumulated for the two nuclear spin scheme due to initialization and pulse imperfections. These errors reduce the optical signal amplitudes for the readout assisted by two nuclear spins, compromising the overall SNR improvement. Nevertheless, the experiments clearly demonstrate that it is in principle possible to further boost the relative SNR using additional nuclear spins.

4.4 Outlook and Conclusions

While we have demonstrated an enhancement for coherent Rabi oscillations, any set of pulses acting on the electronic spin (e.g., a spin echo sequence) can be implemented. This should have immediate applications to NV-based nano-magnetometry [27, 28]. As the duration of the entire repetitive readout sequence ($\sim 150\mu s$ in Figure 4.2B) is shorter than the typical echo duration in pure diamond, SNR improvements directly translate into enhanced sensitivity and increased speed of nanoscale diamond magnetometer [25]. This may have important applications in probing time-varying processes in biophysical systems. The repetitive readout can also be used to achieve single-shot readout of NV centers. At room temperature, with optimized collection efficiency, an improvement in spin signal on the order of a few hundred is needed to achieved single-shot readout. Potentially this improvement can be obtained by using nuclei more robust to optical depolarization, such as the nitrogen nuclear spin of the NV center in isotopically pure ^{12}C diamond [104] and by using advanced control techniques [109, 110] to suppress the imperfections from microwave pulses. Furthermore, resonant optical excitations ($\lambda \approx 637$ nm) can be used for NV centers at cryogenic temperatures. Here the resolved spin structure of optical excited-states [111, 105, 112] can be exploited to readout the electronic spin much more efficiently with reduced perturbation to the nuclear spin [74]. Under these conditions, a ten-fold spin signal improvement may be sufficient to enable single-shot readout of the NV electronic spin. In turn, this can be employed to perform robust, adaptive QND measurements of nuclear spin qubits which will be of direct use for distributed quantum networks [106, 39]. Our experiments demonstrate that manipulation of several nuclear spin an-

cillae surrounding a central electronic spin can be used to implement useful quantum algorithms in solid-state systems.

Chapter 5

Imaging and manipulation of individual spins with nanoscale resolution

5.1 Introduction

Optical techniques constitute powerful tools for spin detection and manipulation that enable applications ranging from atomic clocks[40, 41] and magnetometers[42], to quantum information processors[43, 39, 44, 45] and novel sensors and imaging modalities for biological and life sciences[46, 25, 26, 27, 28, 104]. Several promising methods for fluorescence imaging have recently been developed to surpass the diffraction limit and are already being applied to important problems in biology and neuroscience[113, 114, 115] as well as sub-wavelength optical lithography[116, 117, 118]. For example, sub-diffraction imaging of fluorophores can be obtained by stimu-

lated emission depletion (STED) microscopy and related methods based on reversible saturable optical linear fluorescence transitions (RESOLFT)[119, 47, 120, 121]. Using optical fields with intensity zeros and steep spatial gradients, such as those provided by doughnut-shaped beams, one can transiently switch the fluorophores to a different state everywhere except for a small region near the vanishing optical intensity. In this case the emitters from that small region can be separated from neighbours closer than the diffraction limit. Since the emitters are switched to the designated (on or off) state provided the optical stimulation rate exceeds that of the spontaneous decay rate of that state, the ultimate resolution is, in principle, limited only by the applicable optical power[121].

Our new approach to sub-diffraction spin detection and manipulation is outlined in Figure 5.1. We consider an electronic spin system, such as the NV center in diamond, which can be polarized via optical pumping, coherently manipulated with resonant microwave radiation, and read-out with spin-state-dependent fluorescence. Improved spatial resolution is achieved by illuminating the sample with a doughnut-shaped optical beam just prior to optical spin readout. Spins positioned directly in the center of the doughnut beam are not affected by it. However, spins that are even a few nanometers away from the zero intensity position are re-polarized by the doughnut beam and thus contribute differently to the fluorescence signal, providing nanoscale imaging contrast. Moreover, selective coherent manipulation of a spin in the doughnut center can be achieved by simultaneous exposure to resonant microwave radiation and the optical doughnut beam (Figure 5.1c). The essence of this process is that all coherent spin transitions away from the doughnut center are inhibited by the

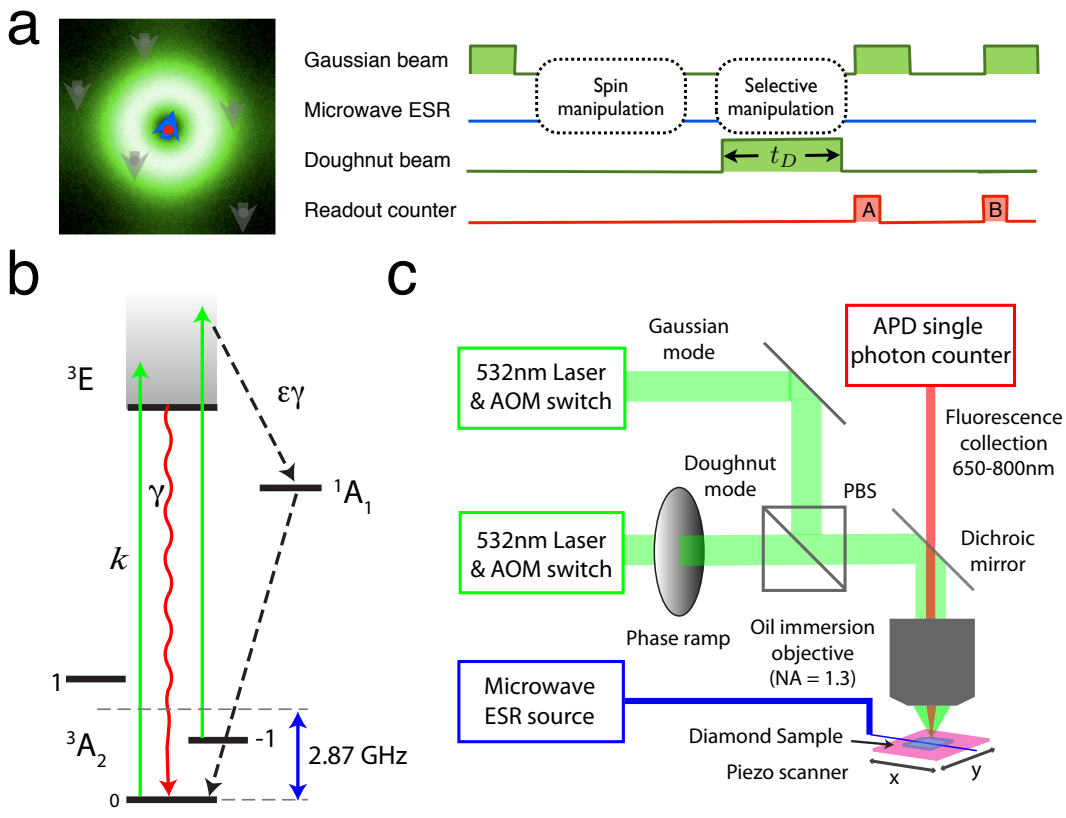

Figure 5.1: **Principles of sub-diffraction far-field optical imaging and magnetometry of individual NV electronic spins in diamond ("spin-RESOLFT").** **a**, Experimental sequence using pulsed optical and microwave excitation. NV spins are first optically pumped to $m_s = 0$ using a Gaussian beam at 532 nm followed by microwave manipulation. Application of 532 nm doughnut beam re-polarizes the outer ring to $m_s = 0$, allowing the spin-state of the central dark region to be independently read-out. **b**, Energy level diagram of NV center showing optical absorption (k) and fluorescence (γ) rates. NV electronic spins are optically pumped from $|m_s| = 1$ to $m_s = 0$ spin states through non-radiative relaxation via the metastable $^1A_1$ singlet state. Microwave fields at around 2.87 GHz coherently manipulate the NV spin states. The differential spin-state population is measured via spin-state-dependent fluorescence in the red. **c**, Schematic of experimental approach. NV centers are imaged using confocal microscopy by scanning the sample around the focal point using a 3-axis piezo stage (see Appendix D.2 for more details on the setup). The doughnut beam is generated by passing a Gaussian beam through a vortex waveplate (2π azimuthally varying phase ramp). See Appendix D.3 for more information on how to create the doughnut beam.

laser field due to a quantum Zeno-like effect[48], thereby allowing coherent rotation of an individual spin at the doughnut center.

5.2 Breaking the diffraction limit resolution

Before proceeding we note that STED and related RESOLFT techniques have been demonstrated to be effective in systems containing metastable states[47], although not spin states previously. A specific advantage of our present approach, which we refer to as spin-RESOLFT, stems from the exceptionally long lifetimes associated with spin sublevels of electronic ground states, which can reach seconds and exceed the lifetimes of electronic transitions by more than six orders of magnitude. Optical transitions involving such ground-state spin levels can be differentially saturated by scattering just a few photons. Therefore, spin-RESOLFT allows individual electronic spins associated with NV centers to be imaged on the nanoscale, with several orders of magnitude lower laser power than most other super-resolution imaging techniques. This offers a significant advantages in many applications, especially to biological systems. Alternatively, for a given power of the doughnut laser beam, spin-RESOLFT allows a dramatic improvement in resolution relative to STED and other RESOLFT approaches, potentially extending to sub-nanometer scales. We also note that another method for resolving closely spaced spins employs large magnetic field gradients[28], as in conventional magnetic resonance imaging. This method, however, requires detailed knowledge of the magnetic gradient topography and is only possible for spins that can be resolved spectrally in ESR or NMR measurements. In what follows we show that the present technique allows one to use far-field optical detection to

resolve individual spins spaced by sub-diffraction-limited distances, sense their local magnetic environment, and perform coherent spin manipulation, even when ESR or NMR measurements are not capable of resolving individual spins spectrally.

Our experimental demonstration makes use of individual NV centers on an ultra-pure single crystal bulk diamond grown by chemical vapour deposition (CVD). The centers were created by irradiating 10^9 cm^{-2} nitrogen ions with energy of 6 keV, corresponding to an estimated average implantation depth of 10 nm, as determined by simulations. The sample was then annealed at 800 °C, yielding an observed NV concentration of approximately 0.6 NV/μm^2. To reliably distinguish shallow implanted ions from natural NV centers, a rare isotope ^{15}N was used (see Appendix D.1 for more information on the implantation/annealing procedure). An electronic spin associated with the NV triplet ground state can be optically polarized, coherently manipulated using conventional electron spin resonance (ESR) techniques[93, 77], and read-out through spin-state-dependent fluorescence[23] (see Figure 5.1b). NV centers in ultra pure diamond display exceptional electron spin lifetimes (T_1), approaching seconds at room temperature[39, 104]. To realize sub-diffraction optical imaging and magnetometry using NV spins, we first polarize all NV centers in the field of view into the ground spin state $m_s = 0$ using a focused Gaussian beam; then drive ESR spin transitions to the $m_s = +1$ or -1 state, or to a coherent superposition of these states; and subsequently use an optical doughnut beam to selectively re-polarize the spins of nearby NV centers. NV centers located in regions of high intensity are optically pumped to the $|0\rangle$ ground state, whereas an NV center located at the central intensity zero remains unaffected and maintains its original state. Thus, spatial in-

formation associated with this central NV is encoded into its electronic spin state, which is subsequently determined by diffraction limited optical readout of the NV fluorescence. Scanning the sample with respect to the beams and repeating the above procedure allows sub-diffraction imaging of the NV centers in the field of view, as well as sensitive nanoscale magnetometry at the location of each NV center due to the Larmor precession of a coherent superposition of NV spin states (detectable via spin-state-dependent fluorescence)[25, 27].

Figure 5.2 shows example sub-diffraction optical images of an NV electronic spin in diamond, acquired using the spin-RESOLFT technique. A ten-fold improvement of 1D resolution was obtained for a fixed power of approximately 2 mW, focused to a diffraction limited spot of 0.07 μm^2, by increasing the duration of the doughnut beam pulse. A similar resolution improvement was achieved for much lower doughnut power of about 0.1 mW, provided the decrease in power is compensated by an increase in doughnut duration. These observations are in excellent agreement with predictions from a simple model of the imaging resolution Δr provided by our sub-diffraction spin detection technique (see Appendix D.4):

$$\Delta r \approx \frac{\lambda/2\mathtt{NA}}{\sqrt{1+\Gamma t_D}} \tag{5.1}$$

Here λ is the wavelength of the optical field, NA is the numerical aperture of the objective, Γ characterizes the maximum rate of optical excitation out of spin state $|1\rangle$, and t_D is the duration of the doughnut beam. Note that the spin imaging resolution is determined by the product of the power and duration of the doughnut beam: hence sub-diffraction-limited resolution can be achieved with a laser power that is well below optical saturation of the excited state (^3E), provided that t_D is sufficiently long. Since

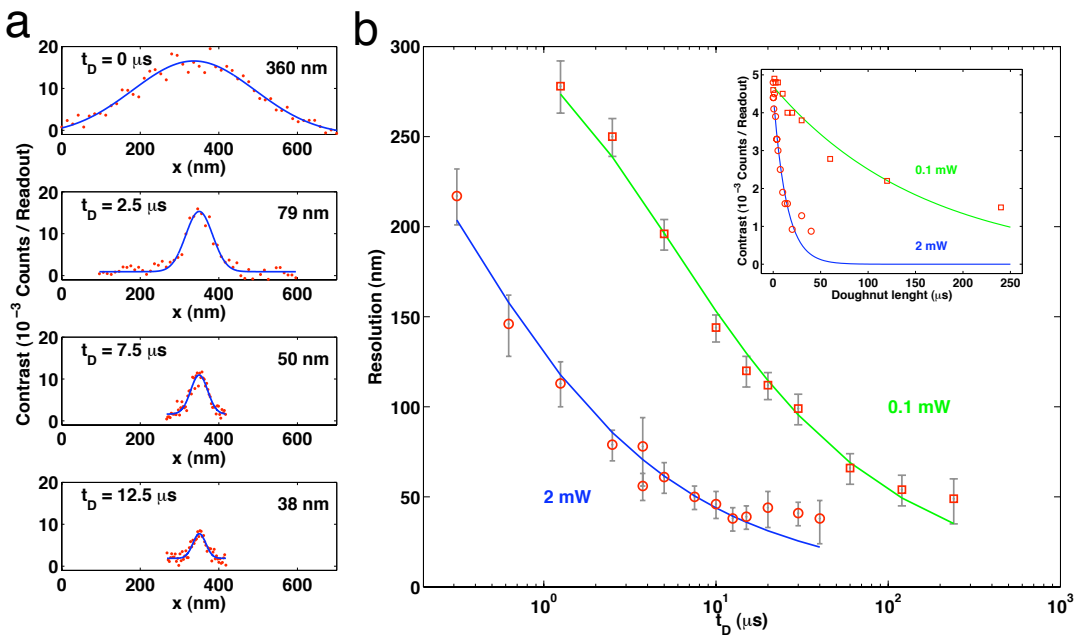

Figure 5.2: **Demonstration of sub-diffraction optical spin imaging.** **a**, Scanning 1D optical images of an NV electronic spin in diamond, for several values of doughnut pulse duration (t_D) at 2 mW total doughnut beam power. **b**, Resolution (FWHM) of 1D spin images as a function of doughnut pulse duration, for both 2 mW and 0.1 mW total doughnut beam power. Solid lines represent a fit to Equation (1). Equivalent resolution is achieved for lower power optical fields applied for longer duration. Long NV spin lifetimes (>10 ms) enables comparable resolution for the present spin-RESOLFT technique with ∼0.1% of the laser power used in STED imaging of NV centers [121]. Resolution is limited by imperfections of the doughnut intensity zero, and/or mechanical instability during doughnut application, which leads to loss of contrast for very large t_D (inset).

the maximum length of t_D is limited by spin state relaxation ($T_1 > 100$ ms) for spin-RESOLFT and by the electronic excited state lifetime (∼10 ns) for STED, we are able to realize sub-diffraction spin imaging using sub-mW doughnut beam power with comparable resolution to that of STED using about one Watt of doughnut power[121].

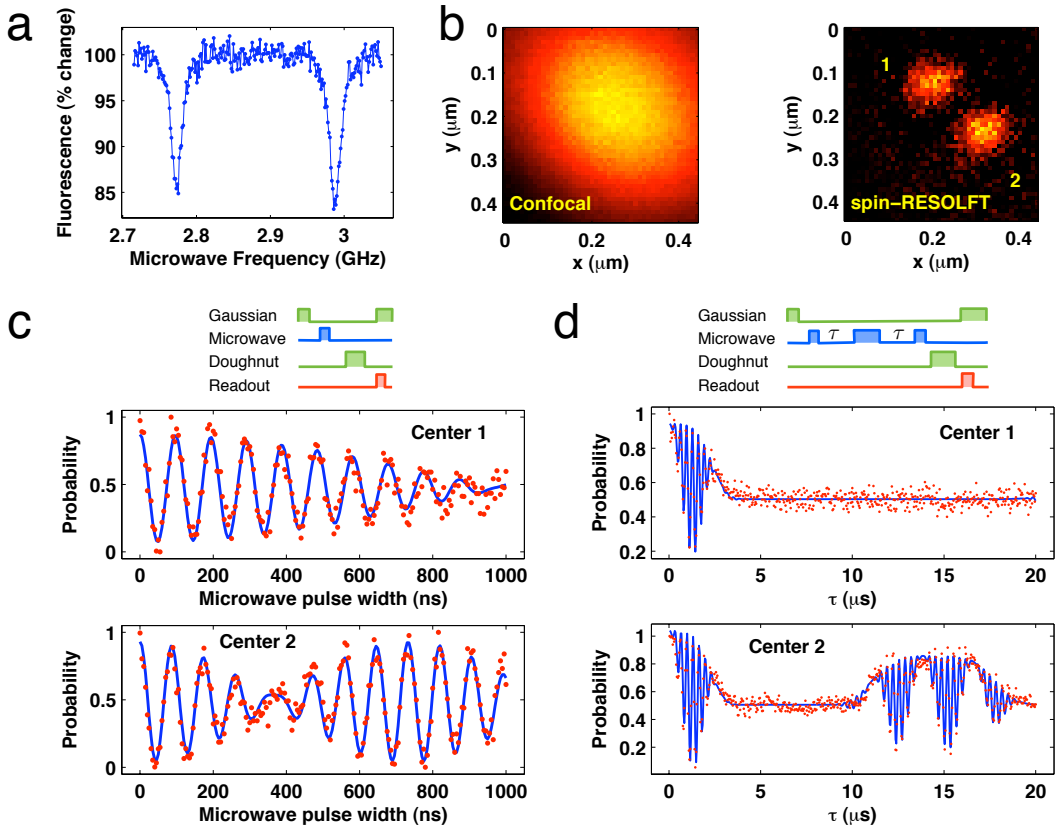

Figure 5.3: **Sub-diffraction optical magnetic sensing.** **a**, Multiple NV centers cannot be identified or distinguished by their optically-detected ESR spectrum, acquired using confocal fluorescence microscopy. **b**, A conventional confocal image does not resolve multiple NV centers; whereas 2D spin imaging using spin-RESOLFT reveals two NV centers separated by ∼150 nm. The conventional confocal image was taken with an objective lens of numerical aperture of 1.3, leading to a spatial resolution of ∼250 nm. **c**, spin-RESOLFT provides spatially-selective measurements of Rabi oscillations for the two neighboring NV spins, which display stark differences due to different local magnetic field environments. **d**, spin-RESOLFT also enables spatially-selective spin-echo measurements for the two NV spins, which reveal substantial differences in spin coherence times, indicating the presence of magnetic impurities in the local environment of NV Center 1. Solid lines in **c** and **d** are fits to a model that includes the electronic spin of the NV center and the nuclear spin of the center's ^{15}N atom.

5.3 High resolution spin imaging and magnetometry

To demonstrate simultaneous nanoscale spin imaging and magnetometry, we applied the spin-RESOLFT technique to NV centers in bulk diamond separated by less than the diffraction limit. Figure 5.3a shows sub-diffraction 2D imaging of two NV centers with identical ESR lines. In this case, it is not possible to identify the presence of multiple centers using conventional confocal imaging and ESR techniques alone. However, by using our new technique, the presence of two NV centers separated by ∼150 nm is directly revealed in a 2D sub-diffraction spin image (Figure 5.3b).

Detection of local magnetic fields with sub-diffraction resolution is presented in Figures 5.3c,d. Specifically, when imaged individually with spin-RESOLFT, each NV center exhibits a distinct modulation of its Rabi oscillation (Figure 5.3c), determined by a relative shift in the center's ESR transition frequency arising from small differences (< 1 G) in the static local magnetic field that each center experiences. Even more subtle differences in the local magnetic field environment of the two NV centers are revealed by sub-diffraction spin-echo measurements using spin-RESOLFT (Figure 5.3d). While at short times each of the centers display spin echoes modulated by Larmor precession of the ^{15}N nuclei in the applied static magnetic field, at longer times the echo signals are substantially different. Center 2 displays good coherent dynamics, evidenced by echo revivals exceeding 20 μs, whereas Center 1 shows no echo revival, due to a nearby ^{13}C nucleus[85] or other magnetic defects (see Appendix D.5). When NV centers have different crystallographic axes and therefore different ESR spectra,

the spin-RESOLFT technique can associate each spectral line with the corresponding location of an individual NV centers with sub-diffraction limited resolution (see Figure D.3 in Appendix D.4).

5.4 Coherent manipulation by inhibiting spin transitions

The spin-RESOLFT technique also enables selective coherent manipulation of individual NV spins separated from other nearby NV centers by less than the diffraction limit. Applying a strong optical doughnut field simultaneously with a resonant microwave field (Figure 5.4a) can suppress coherent spin transitions away from the laser intensity null, in analogy to the quantum Zeno effect of AMO physics[48].

We first demonstrated this effect for an individual, isolated NV center, initially polarized into its $m_s = 0$ state. To distinguish the optical suppression of microwave-driven spin transitions from the conventional optical process used above for re-polarization, we exploited the fact that the optical pumping from $m_s = \pm 1$ into $m_s = 0$ occurs via transition through a metastable singlet state on a timescale of about $\tau_s = 300$ ns. Therefore, we applied a microwave π pulse driving the $|0\rangle \rightarrow |1\rangle$ transition together with a simultaneous pulse of the green laser beam; after which we immediately (within $\tau_d \leq 50$ ns $\ll \tau_s$) optically measured the populations in the $m_s = 0, \pm 1$ and metastable singlet states. As shown in Figure 5.4a, as we increased the laser power, the population in each state (triangles) approached the values measured when no microwave pulse was applied (open circles). This demonstrates that at high laser power

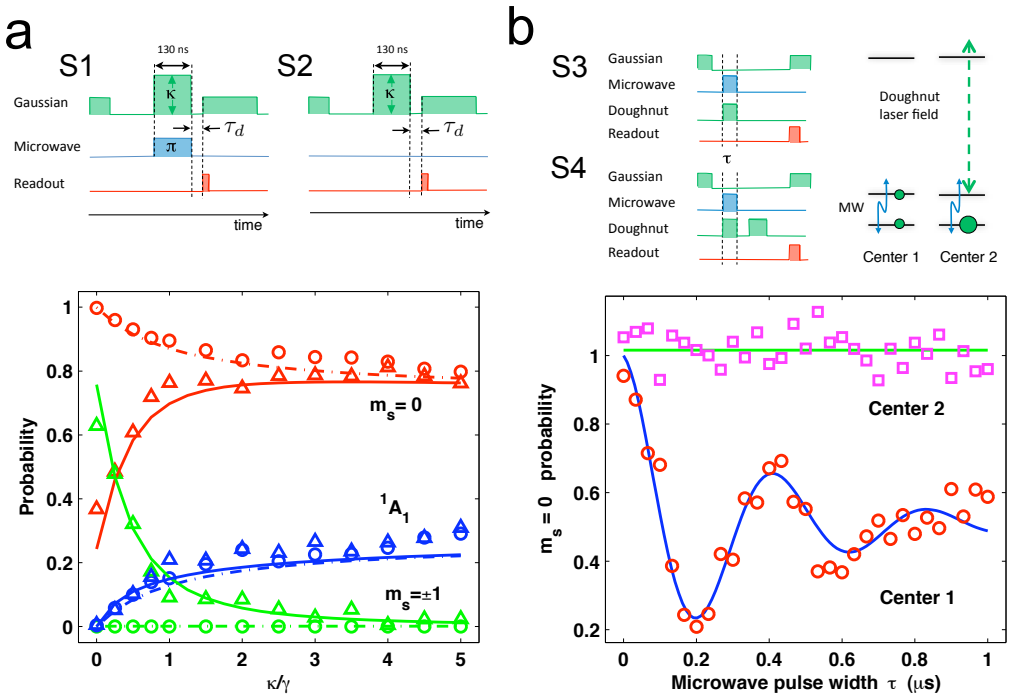

Figure 5.4: **Sub-diffraction coherent manipulation of spectrally indistinguishable NV spins using a quantum Zeno-like effect produced by green excitation light.** **a**, Suppression of a single, isolated NV center's spin transitions, driven by a resonant microwave pulse, as a function of Gaussian laser beam power (characterized by the NV optical excitation rate, κ). Using sequences S1 and S2, the populations of the $m_s = 0$ state (red), $m_s = \pm 1$ state (green), and $^1A_1$ state (blue) were measured with (triangles) and without (open circles) a resonant microwave π pulse of 130 ns duration, applied simultaneously with the Gaussian optical beam. The state populations were determined by recording the fluorescence right after microwave pulse application ($\tau_d < 50$ ns) and also after waiting for a time ($\tau_d = 5$ μs) much longer than the singlet deshelving time (300 ns). The comparison between these two measurements allows us to extract the populations of all states, including the singlet (see Appendix D.6). Solid lines are fits using the master equation described in Ref. [111]. **b**, Coherent spin transitions induced by resonant microwave radiation (MW) are inhibited for NV centers away from the central null of a simultaneously applied green doughnut beam. Selective Rabi oscillations are observed only for the NV spin in the doughnut null (Center 1); whereas NV Center 2, separated from Center 1 by 150 nm, is located outside the doughnut null, and is observed to remain in the ground state. $m_s = 0$ probability for Center 2 is obtained by subtracting measurements acquired with sequence S4 from those acquired with sequence S3.

no population transfer occurs between the $|0\rangle$ and $|1\rangle$ states. Since our experiment measured the populations before the metastable singlet could decay into the ground state $m_s = 0$, the data of Figure 5.4a directly confirms that the observed inhibition of population transfer was not due to repumping out of the $|m_s| = 1$ states. Instead, the observed population dynamics indicates that the $|0\rangle$ to $|1\rangle$ population transfer is suppressed by Zeno-like perturbations of the microwave spin transition induced by light[48], along with partial (small) population transfer into electronic excited states, in which microwave spin-changing transitions are also eliminated (For another realization of the quantum Zeno effect involving NV centers see[122]).

We next employed spin-RESOLFT for selective coherent manipulation of one of two closely spaced NV spins (Center 1 in Figure 5.3b), while the other NV spin (Center 2) was kept in its $m_s = 0$ state via the quantum Zeno-like effect. A pulsed strong doughnut beam was applied simultaneously with a microwave pulse of variable Rabi spin-flip angle, followed by optical measurement of the state of the NV spin at the doughnut center. In a separate calibration experiment, the states of both NV spins were measured together (no optical doughnut applied) as a function of microwave pulse length (Rabi spin-flip angle). The spin-RESOLFT and calibration measurements enabled us to determine the states of the two proximally spaced NV spins individually. As shown in Figure 5.4b, spin transitions are inhibited for the NV center outside the central null of the doughnut beam; whereas the central NV spin undergoes coherent evolution, i.e., Rabi oscillations, in excellent agreement with a theoretical model (blue and green curves in Figure 5.4b), as described in Appendix D.6.

As shown in these demonstration experiments, the far-field optical resolution for spin imaging and coherent manipulation is no longer limited by diffraction. We expect the resolution of the spin-RESOLFT technique to be even further improved by technical upgrades such as increasing the contrast between the intensity of the doughnut crest and that of the central minimum, i.e., perfecting the doughnut zero[121]. In addition, implementing relatively large values of Γt_D, where $\Gamma \sim 100$ MHz near optical saturation and t_D is on the order of the electronic spin lifetime T_1 (which ranges from 10 ms[39] to longer than a second in ultrapure diamond[104]), should allow more than a 1000 fold improvement of resolution below the diffraction barrier, making it feasible to attain sub-nanometer optical spin detection and manipulation, including sensitive measurement of magnetic fields. Finally, the low levels of light required for our technique will also facilitate the parallelization of this imaging process by replacing the scanning doughnut beam with moving arrays of lines or doughnuts of vanishing intensity. This modification should enable fast camera-based spin imaging over a large field of view.

5.5 Outlook and Conclusions

The capability to optically detect and manipulate individual spins with nanometer resolution opens the door to a number of powerful applications in both the physical and life sciences. For example, spin-RESOLFT could can be used for high fidelity addressing of individual spin qubits in an array composed from NV centers separated by distances in the range of 10-30 nm. In such a case, nearby electronic spins could be coupled directly via magnetic or optical dipole-dipole interactions, thereby enabling

high fidelity two-qubit operations. By encoding qubits into nuclear spins nearby to specific NV centers, and using spin-RESOLFT for sub-diffraction addressing of electronic spins and control of electron-nuclear systems, both readout and coherent manipulation could be enabled on nanometer scales, thereby opening a new route to a room temperature scalable quantum information processor (see also[123]). More specifically, the demonstrated Zeno-type inhibition of electronic Rabi oscillations (Figure 5.4b) allows for preparation, detection, and coherent manipulation of one nuclear spin (associated with the NV center in the zero of the green doughnut-shaped beam) without affecting qubits encoded in the nuclear spins of surrounding centers[74] (see Appendix D.6). Likewise, intriguing applications in bioscience can be foreseen for spin-RESOLFT, which combines high sensitivity magnetometry with sub-diffraction imaging resolution. Examples include the use of NV-diamond nanocrystals in living cells as photostable fluorescent biomarkers and sensors of nanoscale magnetic fields, e.g., for direct imaging of activity in neuronal networks and mapping the local concentration of reactive oxygen species and intra-cellular ions. In addition, by exploiting long-lived ground electronic spin states, spin-RESOLFT has the potential for reaching extraordinary imaging and sensing resolution with modest laser power levels, which may be of interest for a diversity of super-resolution imaging applications involving, in particular, biological systems. Finally, we expect that our approach can be applicable to a wide variety of spin systems, from trapped atoms and ions to quantum dots, which may enable a diverse range of interesting applications in quantum science and engineering.

Chapter 6

Group theoretical description of the nitrogen-vacancy center in diamond

6.1 Introduction

During the last five years nitrogen-vacancy (NV) centers have become potential candidates for a number of applications at ambient conditions ranging from magnetometry [25, 26, 27, 28] to high spatial resolution imaging[121] and to quantum computation[23]. At low temperature, the optical transitions of the NV center become very narrow and can be coherently manipulated. This can be used to explore interesting applications such as spin-photon entanglement generation[124] and all optical control[125]. For these applications to be efficiently implemented, it is crucial to have a detailed understanding of the excited state properties of this defect. Several studies

have addressed this issue both experimentally[111, 112] and theoretically[126, 127]. Furthermore, other atom-like defects can potentially be engineered in diamond[20] and other materials with similar or perhaps better properties suitable for the desired application. Therefore, it is of immediate importance to develop a formalism to analyze and predict the main properties of defects in solids.

Here we present such a formalism based on a group theoretical description. While we focus on applications to the nitrogen-vacancy center in diamond, our formalism can be applied to any point defect in solid state physics. Our method takes advantage of the symmetry of the states to properly treat the relevant interactions and their symmetries. We apply group theory to find out not only the symmetry of the eigenstates but also their explicit form in terms of orbital and spin degrees of freedom. We show that this is essential to build an accurate model of the NV center. In particular, we analyze the effect of the Coulomb interaction and predict that the ordering of the triplet and singlet states in the ground state configuration is $\{^3A_2, ^1E, ^1A_1\}$ and that the distance between them is on the order of the exchange term of the electron-electron Coulomb energy. This ordering has been debated over the last few years and our results agree with recent numerical calculations[128]. Our method is also used to analyze important properties of the center such as selection rules. The explicit form of the states helps us to realize a particularly useful lambda-type transition for spin-photon entanglement generation. We show that from the excited state $A_2(^3E)$ the electron can decay to the ground state $^3A_2$ $m_s = 1$ ($m_s = -1$) by emitting a right (left) circularly polarized photon. We demonstrate that this is a consequence of the spin-orbit interaction. This process is particularly robust due to the spin-spin inter-

action in the excited state. We also consider perturbations that lower the symmetry of a point defect, such as strain and electric field. In particular we show how the polarization properties are affected in the presence of strain. We also show that the non-axial spin-orbit interaction proposed in Ref. [129] should not mix the eigenstates of the center in a given multiplet as the spin-orbit interaction remain invariant under the symmetries of the C_{3v} point group. In particular, it should not mix the states of the lower branch of the excited state. Instead, we find that the spin-spin interaction is responsible for the spin state mixing of the excited as a result of the lack of inversion symmetry of the center. We analyze possible sources of mixing between the states. Finally, we analyze the effect of electric fields via the inverse piezoelectric effect and contrast with experimental findings. We show that this can be used to tune the polarization properties of optical transitions and the wavelength of emitted photons, which is of direct importance for photon-based communication between NV centers. Our study clarifies important properties of NV centers and provides the foundation for entanglement between electronic spins and photons in solid state physics.

Our manuscript is organized as follow. In Section 6.2 we present a general group theoretical formalism to calculate the electronic or hole representation of a point defect for a given crystal field symmetry and number of electrons contained in the defect. Next, we use group theory and the explicit form of the states to analyze the effect of the Coulomb interaction between electrons (Section 6.3) and spin-spin and spin-orbit interactions for the NV center (Sections 6.5 and 6.4, respectively). Next, we analyze the selection rules of the unperturbed defect in Section 6.6. Finally, in Section 6.7 we analyze the effect of strain and electric field perturbations.

6.2 State representation

We are particularly interested in quasi-static properties of defects in crystals where the complex electronic structure can be seen spectroscopically. In this limit one can apply the Born-Oppenheimer approximation to separate the many-body systems of electrons and nuclei. It relies on the fact that nuclei are much slower than electrons. In this approximation the nuclei are represented by their coordinates and the physical quantities of the electrons depend on these coordinates as (external) fixed parameters. A defect in a crystal breaks down the translational symmetry reducing the symmetry of the crystal to rotations and reflections. These symmetries form a point group which in general is a subgroup of the point group of the lattice. The loss of translational symmetry indicates that the Bloch-states are no longer the solution of the point defect. In fact, some states can be very well *localized* near the point defect. These defect states are particularly important in semiconductors and insulators when they appear within the fundamental band gap of the crystal.

In the tight binding picture, the electron system of the diamond crystal may be described as the sum of covalent-type interactions between the valence electrons of two nearest neighbor atoms. When defects involve vacancies, the absence of an ion will break bonds in the crystal, producing unpaired electrons or dangling bonds, σ_i, which to leading order can be used to represent the single electron orbitals around the defect. The particular combination of dangling bonds that form the single electron orbitals $\{\varphi_r\}$ is set by the crystal field of the defect and can be readily calculated by projecting the dangling bonds on each irreducible representation (IR) of the point

group of the defect[130],

$$\varphi_r = P^{(r)}\sigma_i = \frac{l_r}{h}\sum_e \chi_e^{(r)} R_e \sigma_i, \tag{6.1}$$

where $\chi^{(r)}(e)$ is the character of operation, e (element), for the IR, r, l_r is the dimension of the IR r and h is the order of the group (number of elements). A detailed application of Equation (6.1) for the case of the NV center can be found in Appendix E.1. There are two non-degenerate totally symmetric orbitals $a_1(1)$ ad $a_2(1)$ that transform according to the IR A_1, and there are two degenerate states $\{e_x, e_y\}$ that transform according to the IR E. At this stage, group theory does not predict the energy order of these states. However a simple model of the electron-ion Coulomb interaction can help to qualitatively get the order of the levels[131]. In Appendix E.1 we model the effect of this interaction on the single electron orbitals, φ_r, for the case of the NV center and find that the ordering of the states (increasing in energy) is $a_1(1), a_1(2)$ and $\{e_x, e_y\}$. Indeed, *ab initio* density functional theory (DFT) calculations revealed [63, 18] that the $a_1(1)$ and $a_1(2)$ levels fall deeper than the e_x and e_y levels which demonstrates the strength of group theory for *qualitative* predictions.

Once the symmetry and degeneracy of the orbitals is determined, the dynamics of the defect is set by the number of electrons available to occupy the orbitals. The orbitals with higher energy will predominantly set the dynamics of the defect. The spin character of the defect will be determined by the degeneracy of the orbitals and the number of electrons in them leading to net spins $S = \{0, 1, 2, ...\}$ if this number is even and $S = \left\{\frac{1}{2}, \frac{3}{2}, ...\right\}$ if odd.

In the case of the negatively charged NV center, each carbon atom contributes one electron, the nitrogen (as a donor in diamond) contributes two electrons and an extra

electron comes from the environment [18], possibly given by substitutional nitrogens [132]. The ground state configuration consists of four electrons occupying the totally symmetric states and the remaining two electrons pair up in the $\{e_x, e_y\}$ orbitals. In this single particle picture, the excited state configuration can be approximated as one electron being promoted from the $a_1(2)$ orbital to the $e_{x,y}$ orbitals[63].

If two more electrons were added to any of these configurations, the wavefunction of the defect would be a singlet with a totally symmetric spatial wavefunction, equivalent to the state of an atom with a filled shell [133, 134]. Therefore, the electronic configuration of this defect can be modeled by two holes occupying the orbitals $e_{x,y}$ in the ground state (e^2 electronic configuration) and two holes in the orbital $a_1(2)$ and $e_{x,y}$ for the excited state (ae electronic configuration). A third electronic configuration, a^2 can be envisioned by promoting the remaining electron from the orbital $a_1(2)$ to the orbitals $e_{x,y}$. Hole and electron representations are totally equivalent and it is convenient to choose the representation containing the smallest number of particles. If a hole representation is chosen, some care must be taken, as some interactions reverse their sign, such as the spin-orbit interaction [133]. In what follows, we choose a hole representation containing two particles (instead of an electron representation containing four particles), since it is more convenient to describe the physics of the NV center. However, the analysis can be applied to electrons as well.

The representation of the total n-electron wavefunction, including space and spin degrees of freedom, is given by the direct product of the representation of each hole and its spin $\Gamma_\Psi = \prod_n \left(\Gamma_{hn} \otimes D_{\frac{1}{2}}\right)$, where $D_{\frac{1}{2}}$ is the representation for a spin $\frac{1}{2}$ particle in the corresponding point group. The reduction or block diagonalization of

the representation Γ_Ψ gives the eigenstates of the hamiltonian associated with the crystal field potential and any interaction that remains invariant under the elements of the point group in question. These interactions include spin-orbit, spin-spin and Coulomb interactions, as well as expansions, contractions, and stress where their axes coincide with the symmetry axis of the defect. The eigenstates can be found by projecting any combination of the two electron wavefunction onto the irreducible representations of the group [130, 135],

$$\Psi^r = P^{(r)}\varphi_1\varphi_2 = \frac{l_r}{h}\sum_e \chi_e^{(r)*} R_e\varphi_1 R_e\varphi_2, \tag{6.2}$$

where φ_i can be any of the orbitals in Equation (6.1) and the subindex i refers to the hole i. In the case of the NV center, it is illustrative to note that the spin representation for the two particles can be reduced to $D_{1/2}\otimes D_{1/2} = A_1+A_2+E$, where A_1 corresponds to the singlet state, and A_2 and E to the triplet state with zero and non-zero spin projections, respectively. A list of the eigenstates and their symmetries for the two hole representation can be found in Table 6.1 for the ground state (e^2) and the excited state (ae). For completeness, we include the doubly excited state (a^2) electronic configuration although this state is not optically accessible in the excitation process of the NV center in experiments. Note that each electronic configuration might have singlet and triplet states. The calculation performed to obtain Table 6.1 is similar to the calculation made to find the eigenstates when two spin particles are considered. However, in this case one should use the Wigner coefficients of the corresponding irreducible representation of the point group under consideration.

Group theory can predict why the hyperfine interaction with the nuclear spin of the nitrogen in the excited state is more than an order of magnitude larger than in

the ground state for both nitrogen species: the non-zero spin density in the ground state wavefunction of the NV center is mostly concentrated in the orbitals $e_{x,y}$ which have no overlap with the nitrogen atom. On the other hand, in the excited state, when one electron is promoted from the $a_1(2)$ orbital to one of the $e_{x,y}$ orbitals, the non-zero spin density comes now from unpaired electrons occupying the orbitals $a_1(2)$ and $e_{x,y}$. As the orbital $a_1(2)$ occupies the nitrogen atom, a sizable contact term interaction between the electronic spin and the nuclear spin of the nitrogen is expected [18, 105, 136].

Up to now, eigenstates inside a given electronic configuration have the same energy, however the inclusion of the electron-electron Coulomb interaction will lift the degeneracy between triplets and singlets. This lifting can be of the order of a fraction of an eV and it is analyzed for the ground state configuration of the NV center in Section 6.3. Furthermore, the degeneracy inside triplet states is lifted by spin-orbit and spin-spin interactions of the order of GHz, where the crystal field plays an important role. These interactions will be treated in sections 6.4 and 6.5.

6.3 Ordering of singlet states

For a given eletronic configuration, the most relevant interaction is the electron-electron Coulomb interaction, which is minimized when electrons are configured in an antisymmetric spatial configuration. As the total wavefunction must be antisymmetric for fermionic particles, the spin configuration must be symmetric. As a result, the state with the largest multiplicity lies lower in energy. This analysis, known as the first Hund's rule, estimates that the ground state of the NV center should be

Table 6.1: Partner functions of each irreducible representation for the direct product of two holes. The first column show the electronic configuration and between parenthesis their triplet (T) or singlet (S) character. The last column shows the name of the states given and their symmetry. In the table $\alpha(\beta)$ reads spin $\uparrow(\downarrow)$ and $E_\pm = |ae_\pm - e_\pm a\rangle$, where $e_\pm = \mp(e_x \pm ie_y)$, $|X\rangle = (|E_-\rangle - |E_+\rangle)/2$ and $|Y\rangle = (|E_-\rangle + |E_+\rangle)i/2$.

Conf.	State	Name
e^2 (T)	$\|e_xe_y - e_ye_x\rangle \otimes \begin{cases} \|\beta\beta\rangle \\ \|\alpha\beta + \beta\alpha\rangle \\ \|\alpha\alpha\rangle \end{cases}$	$^3A_{2-}(E_1)$ $^3A_{20}(A_1)$ $^3A_{2+}(E_2)$
e^2 (S)	$\begin{cases} \|e_xe_x - e_ye_y\rangle \\ \|e_xe_y + e_ye_x\rangle \\ \|e_xe_x + e_ye_y\rangle \end{cases} \otimes \|\alpha\beta - \beta\alpha\rangle$	$^1E_1\ (E_1)$ $^1E_2\ (E_2)$ $^1A_1\ (A_1)$
ea (T)	$\|E_-\rangle \otimes \|\alpha\alpha\rangle - \|E_+\rangle \otimes \|\beta\beta\rangle$ $\|E_-\rangle \otimes \|\alpha\alpha\rangle + \|E_+\rangle \otimes \|\beta\beta\rangle$ $\|E_-\rangle \otimes \|\beta\beta\rangle - \|E_+\rangle \otimes \|\alpha\alpha\rangle$ $\|E_-\rangle \otimes \|\beta\beta\rangle + \|E_+\rangle \otimes \|\alpha\alpha\rangle$ $\|Y\rangle \otimes \|\alpha\beta + \beta\alpha\rangle$ $\|X\rangle \otimes \|\alpha\beta + \beta\alpha\rangle$	$A_1\ (A_1)$ $A_2\ (A_2)$ $E_1\ (E_1)$ $E_2\ (E_2)$ $E_y\ (E_1)$ $E_x\ (E_2)$
ea (S)	$\|a_1x + xa_1\rangle \otimes \|\alpha\beta - \beta\alpha\rangle$ $\|a_1y + ya_1\rangle \otimes \|\alpha\beta - \beta\alpha\rangle$	$^1E_x\ (E_1)$ $^1E_y\ (E_2)$
a^2 (S)	$\|a_1a_1\rangle \otimes \|\alpha\beta - \beta\alpha\rangle$	$^1A_1\ (A_1)$

the triplet $^3A_2$ state. We now address the question related to the order of singlets in the ground state electronic configuration e^2. The order of singlet states has a great significance in understanding the spin-flipping fluoresence of the NV center, and *ab initio* DFT calculations were unable to address this issue properly due to the many-body singlet states. Since we have the explicit form of the wavefunctions we can work out the ordering of the singlets in a given electronic configuration by analyzing the expectation value of the Coulomb interaction, which can be written in the general form,

$$C_{abcd} = \int dV_1 dV_2 a^\star(r_1) b^\star(r_2)\, V(|r_1 - r_2|)\, c(r_1)\, d(r_2)\,.$$

Using this expression we find that in the ground state electronic configuration (e^2), the Coulomb interactions for these states are

$$\begin{aligned} C(^3A_2) &= (C_{xyxy} - C_{xyyx} - C_{yxxy} + C_{yxyx})/2 \\ C(^1E_1) &= (C_{xyxy} + C_{xyyx} + C_{yxxy} + C_{yxyx})/2 \\ C(^1E_2) &= (C_{xxxx} - C_{xxyy} - C_{yyxx} + C_{yyyy})/2 \\ C(^1A_1) &= (C_{xxxx} + C_{xxyy} + C_{yyxx} + C_{yyyy})/2, \end{aligned} \tag{6.3}$$

where x, y correspond to e_x, e_y states. From this set of equations we find that the spacing between the singlets $^1A_1$ and $^1E_2$ is equal to the spacing between the singlet $^1E_1$ and the ground state $^3A_2$, i.e., $C(^1A_1) - C(^1E_2) = C(^1E_1) - C(^3A_2) = C_{xxyy} + C_{yyxx} \equiv 2e$, where the difference is the exchange energy. In addition, as $^1E_1$ and $^1E_2$ belong to the same irreducible representation E, it can be shown that $C(^1E_2) = C(^1E_1)$ (see Appendix E.2). Under this consideration, the ordering of the singlets is $\{^3A_2, ^1E, ^1A_1\}$ with relative energies $\{0, 2e, 4e\}$. It should be noted that, in this case, the most symmetric state has higher energy since the Coulomb interaction between two electrons is repulsive. This picture might be modified by the following effect. As the Coulomb interaction transforms as the totally symmetric IR, the matrix elements between states with the same symmetry are non-zero. The states $^1E(e^2)$ and $^1E(ae)$ can couple via the Coulomb interaction, increasing the gap between them. A similar effect happens with the states $^1A_1(e^2)$ and $^1A_1(a^2)$. We note that, even taking into account these corrections, our basic results here serve as a *qualitative* estimate for the energy of the levels. Furthermore, in Equation (E.1) we did not take into account the effect of the other electrons present in the system. Nevertheless, our approach provides useful insight into the structure of the NV center. A very recent many-body

perturbation theory (MBPT) calculation calculated the energy of singlet states [128] and supported our conclusion.

6.4 Spin-Orbit interaction

In the previous section the electronic spin did not directly enter into the equations. For instance, the energy of the $M_S = 0, \pm 1$ sublevels of the $^3A_2$ ground state would have exactly the same energy. However, if the electronic spin is taken into account, one can infer from Table 6.1 that in general the $M_S = 0$ and $M_S = \pm 1$ projections transform as functions of different IRs. For example, in the ground state $^3A_2$, the $M_S = 0$ projection transforms as the IR A_1, while the $M_S = \pm 1$ projections transforms as the IR E. This implies that the projections do not share the same eigenenergies of the system. Since these states are orbitally degenerate, the spin-spin and spin-orbit interactions may account for the splitting of orbitally degenerate states.

The spin-orbit interaction lifts the degeneracy of multiplets that have non-zero angular momentum and it is also responsible for transitions between terms with different spin states[133]. It is a relativistic effect due to the relative motion between electrons and nuclei. In the reference frame of the electron, the nuclear potential, ϕ, produces a magnetic field equal to $\nabla\phi \times v/c^2$. In SI units, this interaction is given by

$$H_{SO} = \frac{\hbar}{2c^2 m_e^2} \left(\nabla V \times p\right) \cdot \left(\frac{s}{\hbar}\right), \tag{6.4}$$

where $V = e\phi$ is the nuclear potential energy, m_e is the electron mass and p is the momentum. The presence of the crystal field breaks the rotational symmetry

of this interaction. Since ϕ is produced by the nuclear potential, it transforms as the totally symmetric representation A_1, and therefore $\nabla V = (V_x, V_y, V_z)$ transforms as a vector. For a given point group, it is possible to identify the IRs to which these components belong. In the case of C_{3v} symmetry, their components transform as (E_1, E_2, A_1). As p also transforms as a vector, the term $\nabla V \times p = (V_y p_z - p_y V_z, p_x V_z - V_x p_z, V_x p_y - p_x V_y) \propto (L_x, L_y, L_z)$ transforms as the IRs $(E_2, E_1, A_2) = (E, A_2)$. This implies that the expectation values for the orbital angular operators break into two classes: $\langle l_x \rangle = \langle l_y \rangle$ and $\langle l_z \rangle$. Therefore, the spin-orbit interaction has the following form:

$$H_{SO} = \lambda_{xy} \left(l_x s_x + l_y s_y \right) + \lambda_z l_z s_z. \tag{6.5}$$

The non-zero matrix elements of the angular momentum operators l_i in the basis $\{a, e_x, e_y\}$ can be determined by checking if $(\varphi_i, l_k, \varphi_f) \supset A_1$ and are shown in Table 6.2 where $A = \langle e_y | l_x | a \rangle$, $B = \langle e_x | l_z | e_y \rangle$ and $C = \langle e_x | l_x | a \rangle$. For a perfect T_d or spherical symmetry, $A = B$ and $C = 0$. It is also useful to think about $e_\pm$ as $p_\pm$ orbitals and $a_1(2)$ as p_z orbitals, where the angular momentum operators satisfy $l_\pm a_1(2) \propto e_\pm$[137].

Table 6.2: Matrix elements for orbital operators in the C_{3v} point group. For spherically symmetric potentials, $A = B$ and $C = 0$.

l_x	e_x	e_y	a
e_x	0	0	$-iC$
e_y	0	0	iA
a	iC	$-iA$	0

l_y	e_x	e_y	a
e_x	0	0	$-iA$
e_y	0	0	$-iC$
a	iA	iC	0

l_z	e_x	e_y	a
e_x	0	iB	0
e_y	$-iB$	0	0
a	0	0	0

Once it is known how spin-orbit acts on the orbitals, e_x, e_y and a, it is possible to calculate the effect of this interaction on the 15 states given in Table 6.1. An important effect is the splitting in the excited state triplet between the states A_1, A_2 and E_x, E_y

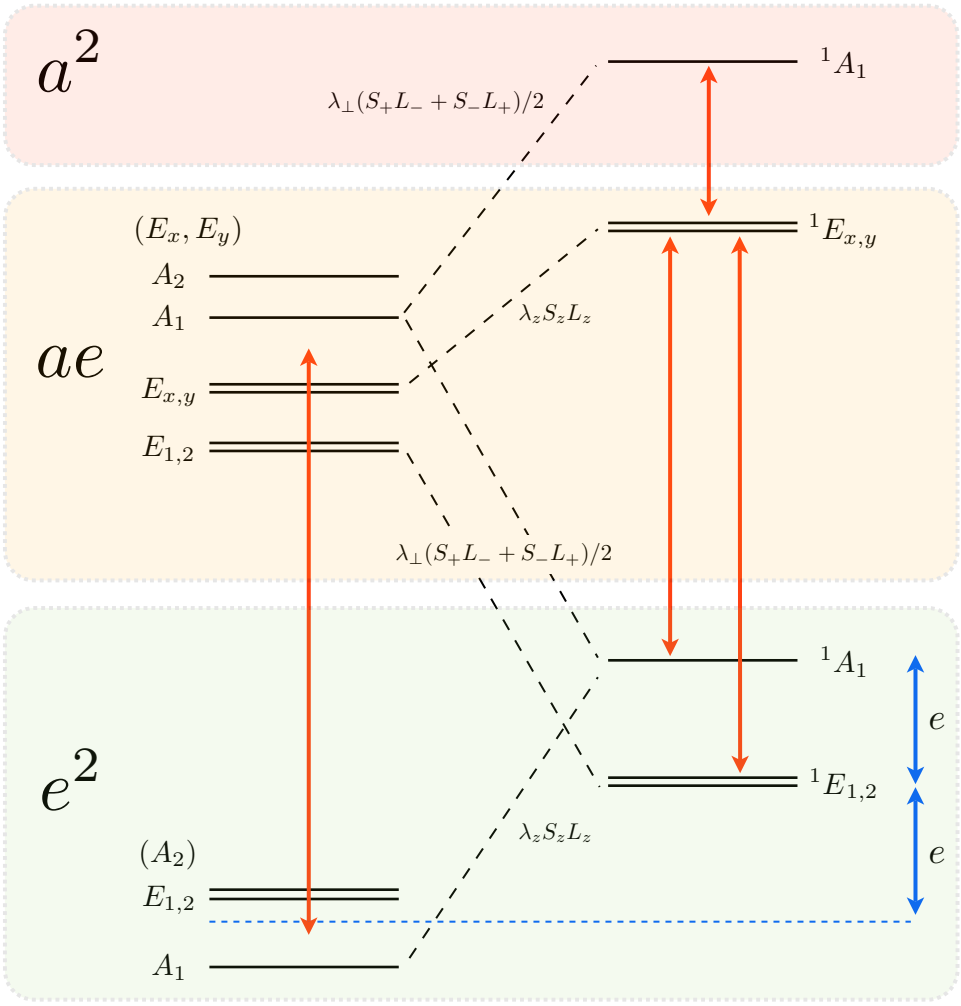

Figure 6.1: **Energy diagram of the unperturbed nitrogen-vacancy center in diamond.** Note that on each electronic configuration can contain triplets as well as singlets. Red arrows indicate allowed optical transitions via electric dipole moment. Dashed lines indicates possible non-radiate process assisted by spin-orbit interaction. In the ground state e^2 configuration, the distance between singlets and triplets is equal to the exchange energy of Coulomb interaction.

and between states E_x, E_y and E_1, E_2[126]. Another effect, relevant when treating non-radiative transitions, is that the axial part of the spin-orbit interaction (λ_z) links states with $m_s = 0$ spin projections among states of the same electronic configuration,

while the non-axial part ($\lambda_\perp$) links states with non-zero spin projections with singlets among different electronic configurations. In Figure 6.1 we show the states linked by the axial and the non-axial parts of the spin-orbit interaction, for which non-radiative transitions might occur. In addition to the well known transition between $A_1(ae) \rightarrow {}^1A_1(e^2)$, we find that this interaction might also link $E_{1,2}(ae) \rightarrow {}^1E_{1,2}(e^2)$ and in particular $E_{x,y} \rightarrow {}^1E_{x,y}(ae)$. The latter transition may play an important role, as recent *ab initio* calculations have shown that the singlets ${}^1E_{x,y}$ might lie very close in energy to the excited state triplet [128]. In our model, the non-axial part of the spin-orbit interaction, $\lambda_\perp \left(l_+ s_- + l_- s_+\right)$, does not mix the states of the excited state triplet with different spin projections because the raising and lower operators, l_- and l_+, link states of different electronic configurations.

We have numerically evaluated the ratio between the axial part and transverse part of spin-orbit, $\lambda_z/\lambda_{xy} = B/A = 0.75$ using the functions e_x and e_y and $a_1(2)$ from *ab initio* calculations (see Appendix E.5). This suggest that if the axial part of spin-orbit is 5.5 GHz [112], the non-transverse part should be on the order of 7.3 GHz. We also have numerically confirmed that the non-axial part of spin orbit does not mix the states on the excited state triplet, as the matrix elements of the raising and lowering angular momentum operator applied over the states $\{e_x, e_y\}$ is zero, i.e. $\langle e_i | l_{x,y} | e_j \rangle = 0$.

6.5 Spin-spin interaction

The spin-spin interaction between electrons is usually not present in systems with spherical symmetry, due to the traceless character of the magnetic dipole-dipole in-

teraction. However, if the electron wavefunction is not spherically distributed, this interaction does not average out. Here we would like to describe its effect on the excited state triplet of the NV center as well as to provide numerical estimation for its strength. The spin-spin interaction can be written (in SI units) as,

$$h_{ss} = -\frac{\mu_0}{4\pi}\frac{g^2\beta^2}{r^3}\left(3(\mathbf{s}_1\cdot\hat{r})(\mathbf{s}_2\cdot\hat{r})-\mathbf{s}_1\cdot\mathbf{s}_2\right), \tag{6.6}$$

where $\mathbf{s}_i = \frac{1}{2}[\sigma_x,\sigma_y,\sigma_z]$ is the spin operator of particle i and σ are the Pauli matrices, β is the Bohr magneton, g is the Landé-factor for the electron and μ_0 is the magnetic permeability of free space[1]. In order to analyze the effect of this interaction in the defect it is useful to write the spatial and spin parts separately in terms of the irreducible representations of the point group. Then, it is straightforward to express this interaction in terms of the eigenstates of the defect (see Appendix E.3),

$$\begin{aligned} H_{ss} = {} & \Delta\left(|A_1\rangle\langle A_1| + |A_2\rangle\langle A_2| + |E_1\rangle\langle E_1| + |E_2\rangle\langle E_2|\right) \\ & -2\Delta\left(|E_x\rangle\langle E_x| + |E_y\rangle\langle E_y|\right) \\ & +2\Delta'\left(|A_2\rangle\langle A_2| - |A_1\rangle\langle A_1|\right) \\ & \Delta''\left(|E_1\rangle\langle E_y| + |E_y\rangle\langle E_1| - i|E_2\rangle\langle E_x| + i|E_x\rangle\langle E_2|\right). \end{aligned} \tag{6.7}$$

Figure 6.2 shows the effect of spin-orbit and spin-spin interactions on the excited state manifold. In particular, we find that the state A_2 has higher energy than the state A_1 contrary to previous estimations[126],[2]. In addition, we find that the spin-spin interaction mixes states with different spin-projections. This effect is the result

[1]The contact term does not contribute due to the Pauli exclusion principle.

[2]Recently, this was indirectly experimentally confirmed. The lower energy state A_1 was observed to have a shorter lifetime than the state A_2[124]. This is as expected since the state A_1 decays non-radiatevely to the singlet $^1A_1$ via non-axial spin-orbit.

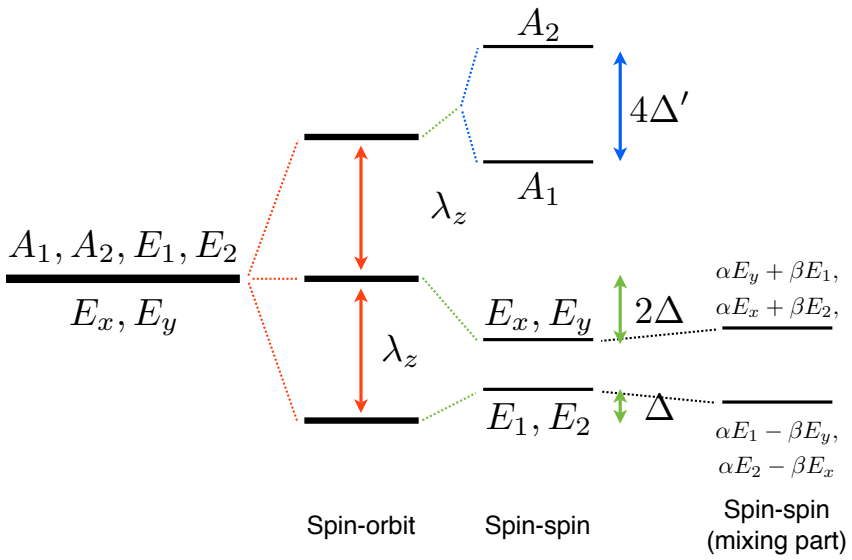

Figure 6.2: **Splitting due to spin-orbit and spin-spin interaction in triplet *ae*.** In addition to the splitting between different spin projections, spin-spin splits states $A_{1,2}$. Our theory predicts the A_2 state over the A_1 state. As state A_1 has an additional non-radiative decay channel, it is possible to confirm this finding by measuring the lifetime of the state. Note that the splitting between A_1 and A_2 is a direct consequence of spin-orbit mixing the spatial and spin part of the wavefunction.

of the lack of inversion symmetry of the NV center and it is not present in systems with inversion symmetry such as free atoms or substitutional atoms in cubic lattices. This has no contradiction with group theory as the mixed states transform according to the same IR (e.g. the E_1 and E_y states transform both according to the IR E_1, see Table 6.1). The gaps between the $m_s = \pm 1$ and $m_s = 0$ projections and between A_1 and A_2 states are given by

$$3\Delta = 3\frac{\mu_0}{4\pi} g^2 \beta^2 \left\langle X \left| \frac{1 - 3\hat{z}^2}{4r^3} \right| X \right\rangle = -\frac{3}{4} D_{zz} \tag{6.8}$$

$$4\Delta' = 4\frac{\mu_0}{4\pi} g^2 \beta^2 \left\langle X \left| \frac{3\hat{x}^2 - 3\hat{y}^2}{4r^3} \right| X \right\rangle = D_{x^2-y^2}, \tag{6.9}$$

while the mixing term is given by

$$\Delta'' = \frac{\mu_0}{4\pi} g^2 \beta^2 \left\langle X \left| \frac{3\hat{x}\hat{z}}{2\sqrt{2}r^3} \right| X \right\rangle . \tag{6.10}$$

We have evaluated numerically the values for this interaction using the orbitals e_x and e_y from *ab initio* calculations (see Appendix E.5). To avoid numerical divergences when $r = 0$, we estimate Equations (6.8) and (6.9) in reciprocal space following reference [138]. We find that the zero field splitting on the ground state is 2.2 GHz compared to the 2.87 GHz found experimentally. Meanwhile, for the excited state, we find that $3\Delta = 0.2$ GHz and $4\Delta' = 2.5$ GHz. This is compared with the experimental values 1.4 GHz and 3.3 GHz measured in [112].

We emphasize that, contrary to the ground state of the NV center, the splitting between A_1 and A_2 in the excited state exists because the spin-orbit interaction mixes the spin and spatial parts. In fact, at high temperatures, where the spin-orbit interaction averages out [127], and if the spatial part is given by $|X\rangle\langle X| + |Y\rangle\langle Y|$, it can be checked by looking at Equation (E.5) that only the zero field splitting Δ_{es} survives from the electronic spin-spin interaction, as confirmed by experiments [105, 127].

6.6 Selection rules and spin-photon entanglement schemes

Group theory tells us which transitions are dipole allowed by checking if the matrix element contains the totally symmetric IR, $\langle \varphi_f | \hat{e} | \varphi_i \rangle \supset A_1$. In the case of the NV center (C_{3v}), the only non-zero matrix elements are $\langle a | \hat{x} \cdot r | e_x \rangle$ and $\langle a | \hat{y} \cdot r | e_y \rangle$, from

which it is straighforward to calculate the selection rules among the 15 eigenstates given in Table 6.1 for the unperturbed center. This is shown in Table 6.3. These matrix elements have been confirmed by our first principles calculations of these matrix elements in the velocity representation as well as by other authors only for the triplet transition [139]. Interestingly, since the excited state triplet has non-zero angular momentum, photons emitted to the ground state must have left or right circular polarization in order to preserve total angular momentum. In addition to the well known triplet-triplet transition [140], transitions are allowed between singlets of different electronic configurations. We remark that the transition between singlet $^1A_1(e^2)$ and singlet $^1E(e^2)$ is not strictly forbidden by group theory in the first order, but since both states belong to the same electronic configuration, no dipole moment exists between them and the probability of radiative transition is extremely low. The ratio between the dipole transition matrix elements associated with the triplet states and those of the singlet states is about $5{\times}10^{-9}$, according to our calculations with the use of wave functions from first principles calculations. This transition might be allowed by phonons or mixing of the states with singlets of different electronic configurations. Regarding recent experiments by Rogers *et al.*, where they identified an emission from singlet to singlet[127], we think it is related to the $^1E(ae) \rightarrow ^1 A_1(e^2)$ transition. The transition $^1A_1(e^2) \rightarrow ^1 E(e^2)$ might be possible for the reasons described above, but it is unlikely to be sizable. A recent MBPT calculation supports our conclusion [128]. A suitable experiment to unravel this issue will be to look at the presence of this emission under resonant excitation. In this case, if the state $^1E(ae)$ is above the excited state triplet, the state $^1E(ae)$ will be hardly populated

and therefore no singlet-singlet transition should be observed.

Once the selection rules are known for the defect, it is possible to realize interesting applications such as spin-photon entanglement generation[141]. In the case of the NV center, the system can be prepared in the $A_2(ae)$ state. Next, by spontaneous decay, the electron can decay to the ground state ${}^3A_{2-}$ by emitting a photon with σ_- (left circular) polarization or to the state ${}^3A_{2+}$ by emitting a σ_+ polarized photon. As a result, the spin of the electron is entangled with the polarization (spin) of the photon. The implementation of this scheme suffers from strain, which will be analyzed in Section 6.7. However, in Section 6.7.1, we recognize that the application of an electric field can be used to overcome some of these issues and facilitate the next step, the entanglement between two NV centers.

Table 6.3: Selection rules for optical transitions between: the triplet excited state (ae) and the triplet ground state (e^2), the singlets (ae) and the singlets (e^2), and the singlet (a^2) and the singlets (ae). Linear polarizations are represented by $\hat{x}$ and $\hat{y}$, meanwhile circular polarization are represented by $\hat{\sigma}_\pm = \hat{x} \pm i\hat{y}$. As an example, a photon with σ_- polarization is emitted when the electron decays from state $A_2(ae)$ to state ${}^3A_{2-}(e^2)$.

$\hat{e}$	A_1	A_2	E_1	E_2	E_x	E_y
${}^3A_{2-}$	$\hat{\sigma}_-$	$\hat{\sigma}_-$	$\hat{\sigma}_+$	$\hat{\sigma}_+$		
${}^3A_{20}$					$\hat{y}$	$\hat{x}$
${}^3A_{2+}$	$\hat{\sigma}_+$	$\hat{\sigma}_+$	$\hat{\sigma}_-$	$\hat{\sigma}_-$		

$\hat{e}$	${}^1E_x$	${}^1E_y$
${}^1A_1$	$\hat{x}$	$\hat{y}$
${}^1E_1$	$\hat{x}$	$\hat{y}$
${}^1E_2$	$\hat{y}$	$\hat{x}$

$\hat{e}$	${}^1A_1$
${}^1E_1$	$\hat{x}$
${}^1E_2$	$\hat{y}$

6.7 Effect of strain

Strain refers to the displacement Δu of the atomic positions under stretch Δx[137]. It is a dimensionless tensor expressing the fractional change under stretching, $e_{ij} =$

$\frac{\partial \delta R_i}{\partial x_j}$, and it can be produced by stress (forces applied to the solid structure), electric field and temperature [142]. Systematic study of strain can be used to unravel the symmetry of defects and explore their properties[143]. Strain can shift the energy of the states as well as mix them. It reduces the symmetry of the crystal field by displacing the atoms. However, not all nine components of strain change the defect in a noticeable way. The antisymmetric part of e_{ij} transforms as a generator of the rotational group and therefore only rotate the whole structure. The symmetry and energies of the unperturbed states do not change upon rotation. Only the symmetric part of strain, $\epsilon = e + e^T$ affects the structure of a defect[137]. As any other element of the theory, strain can be expressed in terms of matrices that transform according to the IRs of the point group under consideration. These matrices can be found by projecting a general strain matrix on each IR,

$$\epsilon_r = \frac{l_r}{h} \sum_e \chi_e^* R_e^\dagger \epsilon R_e. \tag{6.11}$$

In Appendix E.4 we show in detail how to find the effect of strain on the eigenstates of the defect. For simplicity, in the case of the NV center we only write the effect of strain in the manifold $\{e_x, e_y, a(1)\}$,

$$\Sigma_s = \delta^a_{A1} A^a_1 + \delta^b_{A1} A^b_1 + \delta^a_{E1} E^a_1 + \delta^a_{E2} E^b_2 + \delta^a_{E1} E^a_1 + \delta^b_{E2} E^b_2 \tag{6.12}$$

where $\delta^a_{A1} = (e_{xx} + e_{yy})/2$, $\delta^b_{A1} = e_{zz}$, $\delta^a_{E1} = (e_{xx} - e_{yy})/2$, $\delta^a_{E2} = (e_{xy} + e_{yx})/2$, $\delta^b_{E1} = (e_{xz} + e_{zx})/2$, $\delta^b_{E2} = (e_{yz} + e_{zy})/2$ and

$$\begin{aligned} A^a_1 &= \begin{pmatrix} 1 & 0 & 0 \\ 0 & 1 & 0 \\ 0 & 0 & 0 \end{pmatrix} \quad E^a_1 = \begin{pmatrix} 1 & 0 & 0 \\ 0 & -1 & 0 \\ 0 & 0 & 0 \end{pmatrix} \quad E^a_2 = \begin{pmatrix} 0 & 1 & 0 \\ 1 & 0 & 0 \\ 0 & 0 & 0 \end{pmatrix} \\ A^b_1 &= \begin{pmatrix} 0 & 0 & 0 \\ 0 & 0 & 0 \\ 0 & 0 & 1 \end{pmatrix} \quad E^b_1 = \begin{pmatrix} 0 & 0 & 1 \\ 0 & 0 & 0 \\ 1 & 0 & 0 \end{pmatrix} \quad E^b_2 = \begin{pmatrix} 0 & 0 & 0 \\ 0 & 0 & 1 \\ 0 & 1 & 0 \end{pmatrix}, \end{aligned} \tag{6.13}$$

in the manifold $\{e_x, e_y, a_1(2)\}$. The effect of strain on the orbitals $a_1(2), e_x, e_y$ is easy to see. A_1^a will shift equally the energies of the states e_x and e_y, while A_1^b will shift the energy of states a_1. Note that both are axial stresses: the former leaves the e^2 electronic configuration unaffected and the latter leaves the ea configuration unaffected. Either one produces relative shifts between both configurations, resulting in an inhomogeneous broadening of the optical transitions. However, they do not change the selection rules. Only the stress $A_1^a + A_1^b$, corresponding to either expansion or contraction, leaves all relative energies unaffected. E_x^a splits the energy between e_x and e_y and E_y^a mixes the two states. Finally, E_x^b and E_y^b mixes the states e_x and a_1 and e_y and a_1, respectively. In the case of the NV center, the effect of the matrices $E_{x,y}^b$ can be neglected thanks to the large gap between orbitals $a_1(2)$ and $e_{x,y}$. Therefore, in what follows we do not consider them further.

Recent work has been done to analyze how strain affects the excited state structure of the NV center [127, 112]. Here we derive the explicit form of strain affecting the different electronic configurations and look at two important consequences of strain that are relevant for experiments: first, how strain affects the selection rules described in Section 6.6 and second, how strain affects the gap among the states of the lower branch of the triplet excited state making them vulnerable to small local perturbation.

The relevant strain matrices we will consider are E_x^a and E_y^a, for which the hamiltonian is,

$$H_{strain} = \delta_{E1}^a \left(|e_x\rangle\langle e_x| - |\, e_y\rangle\langle e_y|\right) + \delta_{E2}^b \left(|e_x\rangle\langle e_y| + |e_y\rangle\langle e_x|\right). \tag{6.14}$$

This mostly affects the singlet and excited state configurations in the following form,

$$\left(\begin{array}{cc|cc|cc} & & & & \delta_x & -i\delta_y \\ & & & & -i\delta_y & \delta_x \\ \hline & & \delta_x & \delta_y & & \\ & & \delta_y & -\delta_x & & \\ \hline \delta_x & i\delta_y & & & & \\ i\delta_y & \delta_x & & & & \end{array}\right) \left(\begin{array}{ccc} & & 2\delta_x \\ & & 2\delta_y \\ 2\delta_x & 2\delta_y & \end{array}\right) \left(\begin{array}{cc} \delta_x & \delta_y \\ \delta_y & -\delta_x \end{array}\right), \tag{6.15}$$

for the bases $\{A_1, A_2, E_x, E_y, E_1, E_2\}$, $\{{}^1E_1, {}^1E_2, {}^1A_1\}$ and $\{{}^1E_x, {}^1E_y\}$, respectively. The ground state, due to its antisymmetric combination between e_x and e_y, is stable under the perturbation H_{strain}. This can be checked by applying the ground state given in Table 6.1 to Equation (6.14). The effect on the excited state triplet can be seen in Figure 6.3a, where the unperturbed states are mixed in such a way that, in the limit of high strain, the excited triplet structure splits into two triplets with spatial wavefunction E_x and E_y. When strain overcomes the spin-orbit interaction ($\delta_x > 5.5$ GHz), the spin part decouples from the spatial part and total angular momentum is no longer a good quantum number. Transitions from the excited state triplet to the ground state triplet are linearly polarized, where the polarization indicates the direction of strain in the xy plane.

Figure 6.3c shows how the polarization of the emitted photon from the state A_2 to the ground state ${}^3A_{2-}$, varies from circular to linear as a function of strain. In the case of δ_y strain, the effect is similar but now the mixing is different. As shown in Figure 6.3, A_2 mixes with E_1 and the photons become polarized along $x - y$. *Note that, in the limit of low strain, in both cases the polarization remains*

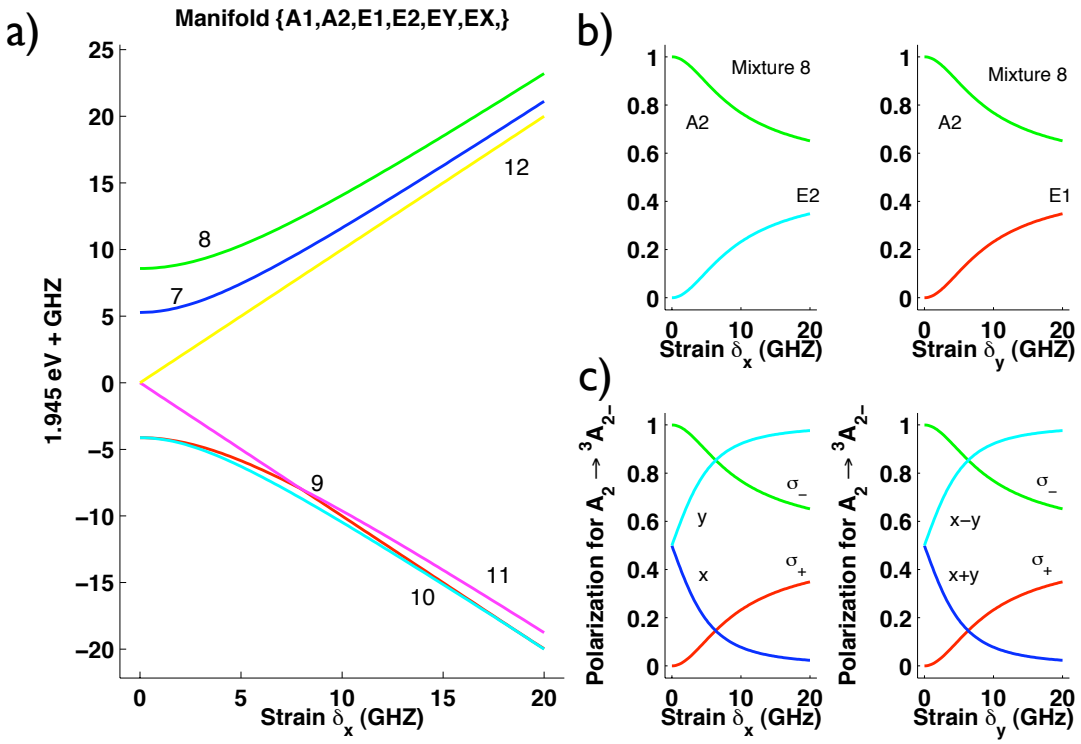

Figure 6.3: **Excited state structure as a function of strain.** a) Eigenvalues of the excited state triplet as a function of δ_x strain. b) Mixture of the eigenstate with higher energy (corresponding to A_2 in the limit of low strain) and c) the polarization of dipolar radiation under transitions from this state to the ${}^3A_{2+}$ state of the ground state. Note that in both cases the circular polarization character of radiation remains. On the other hand, the linear polarization rotates 90° for strain along δ_y with respect to that of strain along δ_x.

right circularly polarized for the transition between the excited state $A_2(ae)$ *to the ground state* ${}^3A_{2-}(e^2)$*, while the polarization remains left circular for the transition between the excited state* $A_2(ae)$ *to the ground state* ${}^3A_{2+}(e^2)$. The fact that at lower strain the character of the polarization remains circular has been succesfully used in entanglement schemes [124]. The polarization properties of the states $E_{x,y}$ are similar to those of the states $A_{1,2}$ but with the opposite polarization.

It is important to note that the effect of external strain depends on the gap between

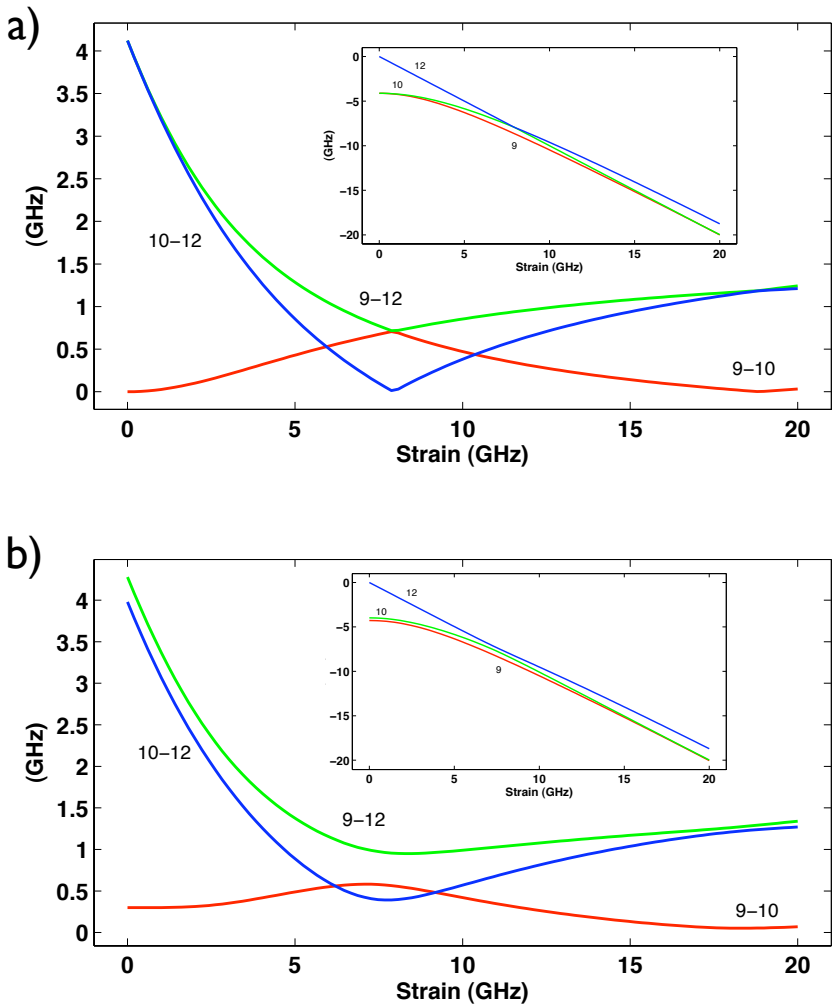

Figure 6.4: **Energy gap among states in the lower branch of the triplet excited state under strain.** a) Energy between mixtures 10 and 12 goes to zero at $\delta_x = 7$ GHz as well as the difference between mixtures 9-10 at 19 GHz. For such small gaps any external interaction involving spin might mix the states. b) In particular, an external magnetic field of 30 Gauss can mix the two states and create the observed anticrossing levels [129]. Also, the nuclear spin interaction can cause a similar effect [144].

states. As an example, we analyze the gap between states of the lower branch of the excited state triplet under strain. On Figure 6.4, we show the gap among the states $\{E_x, E_1, E_2\}$ as a function of strain. Notice that at $\delta_x = 7$ GHz the gap between states

E_x and E_1 reduces to zero and the states cross each other. At this point any small perturbation that mixes the states can transform this crossing into an anticrossing point. In particular, we have shown that the spin-spin interaction can mix the states and also the addition of an external magnetic field or the interaction with the nuclear spin of the nitrogen [144] can cause this effect. For low magnetic field, the interaction the most contribute to the mixing of the states and, therefore, to non-spin-preserving transitions is the spin-spin interaction. This effect is enhanced when strain reduces the gap between states. We emphasize that the non-axial spin-orbit interaction cannot cause this mixing as it is invariant under C_{3v} and it only mixes states from different electronic configurations.

6.7.1 Strain and Electric field

The application of an electric field to a defect leads to two main effects. The first effect, the *electronic effect*, consists of the polarization of the electron cloud of the defect, and the second one, the *ionic effect*, consists of the relative motion of the ions. It has been shown that both effects are indistinguishable, as they have the same symmetry properties[145]. The ionic effect is related to the well-known piezoelectric effect. When a crystal is under stress, a net polarization $P_i = d_{ijk}\sigma_{jk}$ is induced inside the crystal, where d_{ijk} is the third-rank piezoelectric tensor and σ_{jk} represents the magnitude and direction of the applied force. Conversely, the application of an electric field might induce strain given by $\epsilon_{jk} = d_{ijk}E_i$, where E_i are the components of the electric field[142]. The tensor d_{ijk} transforms as the coordinates $x_i x_j x_k$ and, therefore, group theory can be used to establish relations between its components

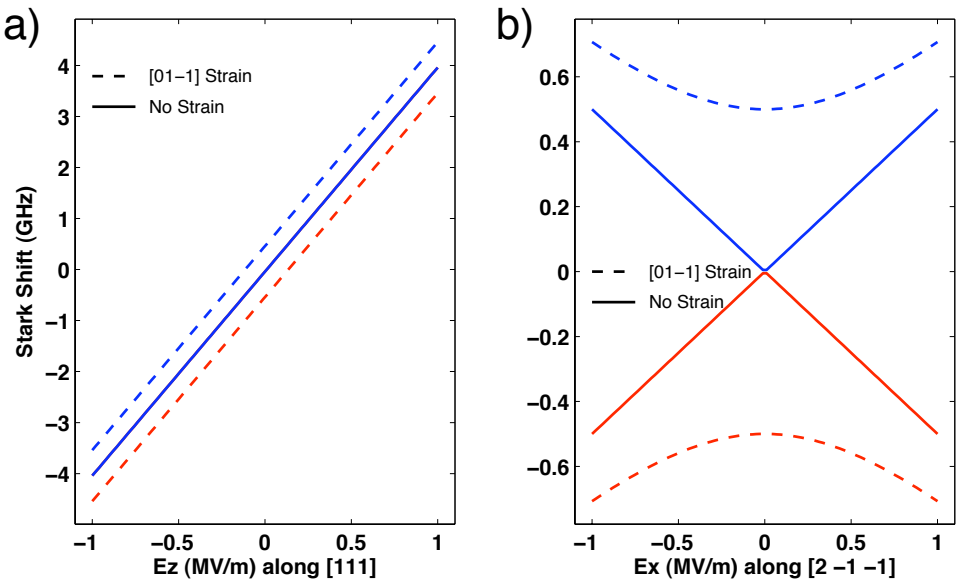

Figure 6.5: **Piezo electric response of optical transitions.** (a) response to electric fields along the NV-axis ([111] orientation or equivalents). The defect only shows linear Stark Shift independent on the initial strain. (b) electric field is applied perpendicular to the NV-axis in the absence of strain (solid lines). The optical transitions ${}^3A_2(m_s = 0) \rightarrow E_x(m_s = 0)$ and ${}^3A_2(m_s = 0) \rightarrow E_y(m_s = 0)$ are split linearly and evenly. In the presence of strain along the $\hat{y}$ direction (dashed lines), the response is quadratic due to the splitting between E_x and E_y states in the excited state. Our numerical results are in fair agreement with experimental results[146].

for a given point group. In particular, the non-zero components should transform as the irreducible representation A_1. By projecting d_{ijk} (or $x_i x_j x_k$) onto the irreducible representation A_1, we can determine the non-zero free parameters of the tensor d and determine the effect of electric field on the eigenstates of the unperturbed defect (see Appendix E.4). In the case of the NV center, the effect on the excited state triplet is given by following matrix,

$$H_E = (b+d)E_z + a \left(\begin{array}{cc|cc|cc} & & & & E_x & -iE_y \\ & & & & -iE_y & E_x \\ \hline & & E_x & E_y & & \\ & & E_y & -E_x & & \\ \hline E_x & iE_y & & & & \\ iE_y & E_x & & & & \end{array}\right), \tag{6.16}$$

in the basis $\{A_1, A_2, E_x, E_y, E_1, E_2\}$, while the effect on the ground state triplet is

$$H_E = 2bE_z, \tag{6.17}$$

in the basis $\{{}^3A_{2+}, {}^3A_{20}, {}^3A_{2-}\}$. Comparing Equations (6.16) and (6.17), we note that the linear response of the excited state and ground state are in principle different. The use of an electric field along the $\hat{z}$ (NV-axis) can be used to tune the optical transition without distorting the C_{3v} symmetry of the defect, provided $b \neq d$. In Figure 6.5a we show the linear response of NV centers under electric field parallel to the NV-axis. In this case, the linearity is not affected by the presence of strain. Our estimations for the ionic effect, based on the response of the lattice defect to electric field and the response of the orbital energies to strain (see Appendix E.4), indicate that the relative shift between the ground and excited state is about 2 GHz / MV/m. This could be very important to entangle two NV centers optically as the wavelength of the photons emitted from each NV center need to overlap[Reference here]. In addition, an electric field with components $E_{x,y}$ can be used to completely restore the C_{3v} character of the defect. In Figure 6.5b, we show the response of optical transitions under an electric field perpendicular to the NV axis. In this case,

the response is linear if strain is absent and quadratic if strain is non-zero. Dashed lines show the response to a 0.5 GHz strain along the [01-1] axis.

6.8 Conclusions

We have used group theory to identify, analyze and predict the properties of NV centers. This analysis can be extended to deep defects in solids. A careful analysis of the properties of a defect via group theory is essential for realization of spin-photon entanglement generation and to control the properties of NV centers such as undesired strain. We have shown that group theoretical approaches can be applied to determine the ordering of the singlets in the (e^2) electronic configuration and to understand the effect of spin-orbit, spin-spin and strain interactions.

Chapter 7

Conclusions and Outlook

Control over individual NV centers have enabled us to understand many aspects of many body dynamics associated with solid-state environments. The ability to explore individual centers by confocal microscopy provides a great amount of information, not only on how the center can coherently interact with its nearby environment, but also on how aggregation of individual NV systems build up the signal from ensemble measurements[68, 32]. It is also now well understood how important it is to have control of the isotopic composition of the diamond lattice. Reducing the concentration of Nitrogen impurities and Carbon-13 greatly improves the coherence times of the NV electronic spin[104] and therefore the performance of a number of applications: e.g., recall that NV magnetic field sensitivity scales inversely proportional to the coherence time, T_2^{-1}, see Chapter 3. Thus a future challenge is to increase the number of sensing NV defects without increasing the number of Nitrogen impurities,which can provide the means for NV spin decoherence. Finding the right balance of NV concentration is crucial to enable high sensitivity magnetometry using large numbers of sensing spins.

In the case of shallow implanted defects, there is still much to understand about how they interact with impurities or localized states at the surface of the material, which seem to rapidly decohere the NV electronic spin. It is crucial to control these undesired effects to employ NV centers as feasible candidates for short distance ($\sim$ 10 nm) spin detection and magnetic imaging of biological samples.

Magnetic sensing combined with the high spatial resolution technique presented in Chapter 5 may have many interesting applications. For example, NV centers could be used to directly image the activity of neuronal networks, or map the local concentration in living cells of paramagnetic molecules such as nitric oxide (NO) and other reactive oxygen species. Our spin-RESOLFT technique is particularly useful for biological samples as it uses considerable less laser power than conventional STED techniques and therefore should be less harmful to living cells.

Although we generally think of nuclear spins (primarily Carbon-13 in diamond) as impurities that cause NV spin-decoherence, we have seen in Chapter 4 that nearby nuclear spins are not always harmful to NV properties when they can be isolated from their environment[39]. Our results show that NV centers in diamond can effectively implement useful quantum control algorithms in solid-state systems by manipulating several nuclear spins proximal to an NV center. In addition, we showed that NV centers can be used for coherent non-destructive mapping of states from other quantum systems such as nearby nuclear spins or electronic spins. This property may be combined with transport of nanocrystals on cantilevers[46], enabling a powerful tool for quantum information transport or with high spatial resolution and coherent control (see Chapter 5) of an array of NV centers. The latter modality may be a

feasible way to realize room temperature quantum computation in which an array of NV centers separated by 10-30 nm from each other can coherently interact via spin dipole-dipole to enable high fidelity two-qubit operations. The nuclear spin of the NV center can then serve as a qubit memory that can be addressed individually by using the spin-RESOLFT technique.

The stability of a defect is determined by how the level structure of the defect behaves under perturbations such as vibrations and crystal deformation. As an example, the ground state of the negatively charged NV center is stable under static Jahn-Teller distortions of the lattice[147] because it has the two degenerate energy levels are fully occupied. Many of these properties/characteristics are well understood when the problem is approached from group theory. In fact, in the case of the NV center the crystal field produces a robust excited state for spin-photon entanglement schemes (see Chapter 6) thanks to how the crystal field sets the way spin-spin and spin-orbit interactions manifest. Looking at the symmetry of the crystal field not only successfully predicts this behavior but also provide the tools to analyze the performance of this scheme under perturbations that reduce the symmetry. In this regard, there is still much work to do to understand how the different vibrations are coupled to the defect. An accurate group theoretical analysis can be used to predict the properties of other centers and more importantly engineer defects with desired properties.

We have seen that the properties of nitrogen-vacancy centers have enabled a number of interesting applications that exploit the quantum manipulation of spin and

orbital degrees of freedom. Many of these applications, such as magnetic sensing, are just starting to become efficient; and although there is still much to understand about the complex structure of this center and its environment, the community has gained a great deal of experience and at the same time been surprised about the NV center's outstanding properties at room temperature, enabled by symmetry and by the large band gap of diamond. Present technology has enabled researchers to explore in exquisite detail the structure and environment of the NV center, though there is still work to do and perhaps surprises awaiting in the ultra fast dynamics of the NV center. Finally, the fortuitous properties of the NV center might not be unique to it. We should also be open to explore not only other types of point defects but also delocalized ones, where an ensemble of quantum degrees of freedom might join to build a robust quantum manifold.

Appendix A

Supporting material for Chapter 2

A.1 Phenomenological models for decoherence

When the details of the interaction between the central spin and the environment and the properties of the latter are not known or difficult to model, the effect of the environment on the central spin can be model by a random fluctuating field $b(t)$ with mean value zero and some spectral density $S_b(\omega)$. In the case of the NV center, the relevant hamiltonian for this approach is

$$H = \Delta S_z^2 + B \cdot S + b \cdot S \tag{A.1}$$

where Δ is the zero field splitting, B is the static external magnetic field. To second order perturbation theory (see Section A.4 in this Appendix), hamiltonian (A.1) can be written as

$$H = \Delta S_z^2 + B \cdot S + b_z S_z + \sum_m |m\rangle\langle m| \left(\alpha_m b_\perp + \beta_m b_\perp^2\right) \tag{A.2}$$

where $\alpha_m = (3m^2-2)B_\perp/2\Delta$ and $\beta_m = (3m^2-2)/\Delta$. The free induction decay (fid) and echo signals of an initial state $\varphi_i = |a\rangle + |b\rangle$ is proportional to

$$p = \frac{1}{2} + \frac{1}{2}\exp\left(-\langle\Phi^2\rangle/2\right) \tag{A.3}$$

where $\Delta\phi = \delta\phi(0,\tau)$ and $\Delta\phi = \delta\phi(-\tau/2,0) - \delta\phi(0,\tau/2)$, respectively. $\delta\phi(t_1,t_2) = \phi_a(t_1,t_2) - \phi_b(t_1,t_2)$ and $\phi_m(t_1,t_2) = \int_{t_1}^{t_2} dt\langle m|H/\hbar|m\rangle$. It is clear from Equation (A.2) that there will be a dependence on the angle θ between the NV axis and the magnetic field. However, in this section, our aim is not to study this dependence but the effect of the environment via the stochastic variable b. Therefore, in what follows we will neglect the angular dependence and consider only,

$$\phi_m(t_1,t_2) = m\int_{t_1}^{t_2} b(t)dt \tag{A.4}$$

For $\phi(t_1,t_2) = \int_{t_1}^{t_2} b(t)dt$ and b a random variable, it can be shown that

$$\langle\Phi^2\rangle_{fid} = \frac{2}{\pi}\int_0^\infty d\omega\frac{S_b(\omega)}{\omega^2}\sin^2\left(\frac{\omega\tau}{2}\right) \qquad \langle\Phi^2\rangle_{echo} = \frac{8}{\pi}\int_0^\infty d\omega\frac{S_b(\omega)}{\omega^2}\sin^4\left(\frac{\omega\tau}{4}\right) \tag{A.5}$$

and $S_b(\omega)$ is the spectral density which is characterize by the average power P of the random field, $P = \frac{1}{2\pi}\int_0^\infty S_b(\omega)d\omega = \frac{1}{T}\int_{-\infty}^{\infty}\langle x_T(t)^2\rangle dt$.

Table A.1: Various types of spectral densities and its corresponding echo decay. The spectral density is given by $S_b(\omega)$ between the range of frequencies ω_a and ω_b and 0 otherwise.

Noise	$S_b(\omega)/\mathcal{N}P$	$\mathcal{N}$	$\langle\Phi^2\rangle_{echo}/2\mathcal{N}P$
White	1	$\frac{2\pi}{(\omega_b-\omega_a)}$	$\frac{1}{4}\tau$
$1/f$	ω^{-1}	$\frac{2\pi}{\log(\omega_b/\omega_a)}$	$\frac{\log(2)}{4\pi}\tau^2$
$1/f^2$	ω^{-2}	$\frac{2\pi\omega_a\omega_b}{(\omega_b-\omega_a)}$	$\frac{1}{24}\tau^3$

Spectral densities that transform as ω^{-n} are not realistic for low frequencies. Instead, many experiments show a constant spectral density for frequencies between 0 and some particular cut-off ω_c[148]. For frequencies above this cut-off, the spectral density can be modeled by the spectral densities given in Table A.1. In most of the cases, this constant part of the spectral density leads to decoherence in fid signals giving the characteristic decay $\exp(-\tau^2)$. In these cases, $\omega\tau \ll 1$ for the relevant frequencies that contributes to the decay. On the other hand, in cases where the large frequency components contributes as much as the low frequencies, the fid signal decays exponentially, $\exp(-\tau)$, revealing an environment with a fast dynamics.

For these reasons, a lorentzian spectral density is used to model both, fid and echo decays,

$$S_b(\omega) = \frac{P\tau_c}{1+\omega^2\tau_c^2} \tag{A.6}$$

where τ_c is the correlation time of the environment,

$$\langle b(\tau+t)b(t)\rangle = P\exp(-\tau/\tau_c) \tag{A.7}$$

For times $\tau \leq \tau_c$, we find that the signal is given by,

$$p_{fid} = \frac{1}{2}\left(1+\exp-(\tau/T_2^*)^2\right) \qquad p_{fid} = \frac{1}{2}\left(1+\exp-(\tau/T_2)^4\right) \tag{A.8}$$

where $T_2^* = \sqrt{2/P}$, $T_2 = (2\tau_c^2/\alpha P)^{1/4}$ and $\alpha = (4-\pi)/2\pi$. Leading to the well-known relation,

$$T_2 = \sqrt{1.6\tau_c T_2^*}. \tag{A.9}$$

A.2 Decoherence due to off-axis magnetic field

When the magnetic field is not aligned with the NV axis, the electronic spin echo signal decoheres. This effect is solely due to the interaction between the central spin and the bath of nuclear spins and not due to the interaction among spins in the bath. As explained in Chapter 2, revivals occur because all nuclei precess with the same frequency when the electron is in its 0 state. If only one nucleus precess at a different rate, the center decoheres. In this section we will analyze the form of this decoherence. The contribution to the echo signal of one nucleus is

$$S_n(\tau) = 1 - 2|\hat{\Omega}_0 \times \hat{\Omega}_1|^2 \sin^2 \frac{\Omega_0^n \tau}{2} \sin^2 \frac{\Omega_1 \tau}{2}. \tag{A.10}$$

The Larmor frequency of a single nucleus can be enhanced by the electron due to virtual process (see Section A.4 in this Appendix) and therefore the nucleus might precess at a different rate rather than at the bare Larmor frequency Ω_0, i.e., $\Omega_0^n = \Omega_0 + \delta\Omega_0^n$. At the revivals we have that $\sin \Omega\tau/2 = 0$ and consequently,

$$\begin{aligned} \sin \frac{\Omega_0^n \tau}{2} &= \sin \frac{(\Omega_0 + \delta\Omega_0^n)\,\tau}{2} = \sin \frac{\Omega_0 \tau}{2} \cos \frac{\delta\Omega_0^n \tau}{2} + \sin \frac{\delta\Omega_0^n \tau}{2} \cos \frac{\Omega_0 \tau}{2} \\ &= \sin \frac{\delta\Omega_0^n \tau}{2} \end{aligned} \tag{A.11}$$

Therefore, the pseudo spin at the revivals is given by

$$S_n^{\mathtt{env}}(\tau) = 1 - 2|\hat{\Omega}_0 \times \hat{\Omega}_1|^2 \sin^2 \frac{\delta\Omega_0^n \tau}{2} \sin^2 \frac{\Omega_1 \tau}{2} \tag{A.12}$$

If now we consider that $\delta\Omega_0$ is small and Ω_1 is large we can do the following approximations

$$\sin^2 \frac{\delta\Omega_0^n \tau}{2} \approx \frac{\delta\Omega_0^{n2} \tau^2}{4} \qquad \sin^2 \frac{\Omega_1 \tau}{2} \approx \frac{1}{2}, \tag{A.13}$$

which leads to the following envelope for the echo signal

$$S_n^{\text{env}}(\tau) \approx 1 - |\hat{\Omega}_0 \times \hat{\Omega}_1|^2 \frac{\delta\Omega_0^{n2}\tau^2}{4}. \tag{A.14}$$

In addition, it is not difficult to see that to leading order in θ (the angle between the NV axis and the magnetic field), $\delta\Omega_0^n \propto \theta$. At this point we can approximate the signal by

$$S_{\text{env}}^{\text{off-axis}}(\tau) \approx \exp\left(-\alpha\theta^2\tau^2\right). \tag{A.15}$$

The envelope now decays as a Gaussian.

A.3 Ensemble measurements

It is found that on ensemble measurements the decay of the echo signal does not follow the predicted decay of single defects ($\exp(-\tau^n)$ with $n = 3-4$). Instead, the signal falls off with lower n's looking even exponential. In dilute samples, where average distance between NV centers is large enough so that the interaction between them is neglected, this effect is just the average of many single echo signals with different decay rates. As explained in Chapter 2, when the magnetic field is off axis, the ensemble signal is the average of many gaussian decays with different rates,

$$E(\tau) = \int f(b) \exp\left(-b\tau^2\right) db. \tag{A.16}$$

In this section, we show that the distribution for the parameter b is $f(b) = b^{-3/2}$.

It is clear from Section A.2 that the parameter b in Equation (A.16) is proportional to the hyperfine interaction squared between the central spin and the nearby nucleus

n,

$$b = A_n^2 = \left(\frac{\mu_0}{4\pi}\gamma_e\gamma_n\right)^2 \frac{1}{r^6} \tag{A.17}$$

where r is the distance between the central spin and nucleus n. On a cubic lattice, this distance is given by $r^2 = a^2\left(i^2 + j^2 + k^2\right)$ where a is the nearest neighbor distance and $\{i, j, k\}$ are indices running from $-I$ to I. The position $i = j = k = 0$ is excluded since it correspond to the position of the central spin. The distribution for the distance is clearly $f_r(r) = 4\pi r^2$. And the distribution for the variable b can be calculated following recipes from statistical analysis as follow. The cumulative probability distribution for the variable b is given by

$$F_b(b) = \int_{b \leq r^{-6}} f_r(r)dr \propto r^3|_{b^{-1/6}}^{r_{max}} = cte - b^{-1/2} \tag{A.18}$$

and therefore,

$$f_b(b) = \frac{\partial F_b(b)}{\partial b} = b^{-3/2}, \tag{A.19}$$

which needs to satisfy $\int f(b) = 1$. b can vary between

$$b_{min} = \left(\frac{\mu_0}{4\pi}\gamma_e\gamma_n\right)^2 \frac{1}{r_{max}^6} \qquad b_{max} = \left(\frac{\mu_0}{4\pi}\gamma_e\gamma_n\right)^2 \frac{1}{a^6} \tag{A.20}$$

and therefore the normalized distribution is

$$f_b(b) = 2b^{-3/2}\left(\frac{1}{\sqrt{b_{min}}} - \frac{1}{\sqrt{b_{max}}}\right). \tag{A.21}$$

A.4 Non-Secular Correction

The most common approximation in central spin problems is the so called secular approximation which consists on neglecting off diagonal elements of the central spin

manifold. However, experiments have proven that this approximation is not enough to account for all observations. A clear example is the Knight shift. Also observed is the enhanced coupling between two other spins that interact via virtual transitions with the central spin. All this phenomena can be explained by perturbation theory. In this appendix we work in detail the perturbation contribution of non-secular terms to the dynamics of the nuclear bath for a central spin 1 (NV case) and for a central spin 1/2.

Elements of perturbation theory

Consider the hamiltonian of a central spin S in the presence of a nuclear spin bath $\{I_n\}$,

$$H = \Delta S_z^2 - \gamma_e \mathbf{B}\cdot\mathbf{S} - \sum_n \gamma_n \mathbf{B}\cdot\mathbf{I}_n - \sum_n \mathbf{S}\cdot\mathbf{A}_n\cdot\mathbf{I}_n - \sum_{n>m} \mathbf{I}_n\cdot\mathbf{C}_{nm}\cdot\mathbf{I}_m \quad \text{(A.22)}$$

or

$$H = \Delta S_z^2 - \gamma_e \mathbf{B}\cdot\mathbf{S} - \sum_n \gamma_n \mathbf{B}\cdot\mathbf{I}_n - \sum_{n,i,j} S_i A_{ij}^n I_j^n - \sum_{n>m,i,j} I_i^n C_{ij}^{nm} I_j^m$$

where the index n runs over the nuclear bath, $i,j = \{x,y,z\}$. The first term is the zero field splitting only relevant when $S > \frac{1}{2}$, the second and third term are the Zeeman interactions for the central spin and nuclear bath, respectively, the fourth term is the hyperfine interaction between the central spin and the nuclear bath and the last term is the dipole-dipole interaction among nuclear spins. In order to approach this problem perturbatively, we identify the secular H_0 and non-secular V part of the hamilonian,

$$H_0 \;= \Delta S_z^2 - \gamma_e B_z S_z - \textstyle\sum_n \gamma_N \mathbf{B}\cdot\mathbf{I}_n - \sum_{nj} S_z A_{zj}^n I_j^n, \tag{A.23}$$

the non-secular one, which will be treated as a perturbation,

$$V \;= -\tfrac{1}{2}\left(\gamma_e\left(B_- S_+ + B_+ S_-\right) + \textstyle\sum_{nj}\left(S_+ A_{-j}^n I_j^n + S_- A_{+j}^n I_j^n\right)\right). \tag{A.24}$$

The hamiltonian of the nuclear bath will not be relevant for the purpose of this appendix,

$$H_{nuc} = -\sum_{n>m} \mathbf{I}_n \cdot \mathbf{C}_{nm} \cdot \mathbf{I}_m. \tag{A.25}$$

Second order perturbation theory states that[149],

$$E_i^{(2)} = \langle\phi_i|VQ\frac{1}{E_i^{(0)} - H_0}QV|\phi_i\rangle \tag{A.26}$$

where $\{|\phi\rangle\}$ is the unperturbed state manifold of the central spin, $Q = 1 - P$ and $P = |\phi_i\rangle\langle\phi_i|$.

Perturbation for $S = 1$ central spin

For the case of $S = 1$ we have that to second order the corrections for the energies are

$$E_{\pm1}^{(2)} \;=\; \frac{\langle\pm1|V|0\rangle\langle 0|V|\pm1\rangle}{E_{\pm1}^{(0)} - E_0^{(0)}} \tag{A.27}$$

$$E_0^{(2)} \;=\; \frac{\langle 0|V|-1\rangle\langle -1|V|0\rangle}{E_0^{(0)} - E_{-1}^{(0)}} + \frac{\langle 0|V|1\rangle\langle 1|V|0\rangle}{E_0^{(0)} - E_1^{(0)}} \tag{A.28}$$

where $E_0^{(0)} - E_{\pm1}^{(0)} = -\Delta \pm \gamma_e B_z$ and

$$\langle 0|V|\pm\rangle \;=\; -\frac{1}{\sqrt{2}}\left(\gamma_e B_\pm + \sum_n \mathbf{A}_{\pm n}\cdot\mathbf{I}_n\right) \tag{A.29}$$

It is straightforward to calculate

$$E^{(2)}_{m_s} = \frac{(3m_s^2-2)\,\Delta + m_s\gamma_e B_z}{2\,(\Delta^2-\gamma_e^2 B_z^2)}\hat{M} + \frac{(m_s^2-2)\,\gamma_e B_z - m_s\Delta}{2\,(\Delta^2-\gamma_e^2 B_z^2)}\hat{N} \tag{A.30}$$

where

$$M = \gamma_e^2 B_\perp^2 + \sum_n \gamma_e \left(B_- \mathbf{A}^n_+ \cdot \mathbf{I}_n + B_+ \mathbf{A}^n_- \cdot \mathbf{I}_n\right) + \frac{\mathbf{A}^n_- \mathbf{A}^n_+}{2} + \sum_{n\neq m} \mathbf{A}^n_- \cdot \mathbf{I}_n \mathbf{A}^m_+ \cdot \mathbf{I}_m \tag{A.31}$$

$$N = i\sum_n \mathbf{I}_n \cdot \mathbf{A}^n_+ \times \mathbf{A}^n_- = \sum_n I_n \cdot \mathbf{A}^n_x \times \mathbf{A}^n_y \tag{A.32}$$

Let us get some special cases

(i) $\Delta \gg B_z$ $(B_z \approx 0)$

$$E^{(2)}_{m_s} = \frac{(3m_s^2-2)}{2\Delta}\hat{M} - \frac{m_s}{2\Delta}\hat{N} \tag{A.33}$$

(ii) $\Delta \ll B_z$ $(\Delta \approx 0)$

$$E^{(2)}_{m_s} = -\frac{m_s}{2\gamma_e B_z}\hat{M} + \frac{(2-m_s^2)}{2\gamma_e B_z}\hat{N} \tag{A.34}$$

Perturbation for $S = 1/2$ central spin

For the case of $S = 1/2$ we have to second order that

$$E^{(2)}_{\pm} = \frac{\langle \pm|V|\mp\rangle\langle\mp|V|\pm\rangle}{E^{(0)}_{\pm} - E^{(0)}_{\mp}} \tag{A.35}$$

where $E^{(0)}_{\pm} = \mp\gamma_e B_z/2$ and the non-zero matrix elements are

$$\langle \pm|V|\mp\rangle = -\frac{1}{2}\left(\gamma_e B_\mp + \sum_n \mathbf{A}_{\mp n}\cdot\mathbf{I}_n\right) \tag{A.36}$$

therefore

$$E^{(2)}_{m_s} = \frac{1}{4\gamma_e B_z}\hat{N} - \frac{m_s}{2\gamma_e B_z}\hat{M}. \tag{A.37}$$

Back action on nuclear bath

The above analysis found new terms for the dynamics of the nuclear bath which now we will put in more familiar terms. First we need to distinguish between constant terms and dynamics terms, terms that depend on the state of the nucleus. The $\hat{M}$ operator contains a constant part $\hat{M}_C$ and a dynamic part $\hat{M}_D$,

$$\hat{M} = \hat{M}_C + \hat{M}_D \tag{A.38}$$

$$\hat{M}_C = \gamma_e^2 B_\perp^2 + \frac{1}{2}\sum_n |\mathbf{A}_x^n|^2 + |\mathbf{A}_y^n|^2 \tag{A.39}$$

$$\hat{M}_D = \sum_n 2\gamma_e \mathbf{B}\cdot\mathbf{G}_n\cdot\mathbf{I}_n + \sum_{n>m} 2\mathbf{I}_n\cdot\mathbf{G}_n^T\mathbf{G}_m\cdot\mathbf{I}_m \tag{A.40}$$

where

$$\mathbf{G}_n = \begin{pmatrix} \mathbf{A}_x^n \\ \mathbf{A}_y^n \\ 0 \end{pmatrix} = \begin{pmatrix} A_{xx}^n & A_{xy}^n & A_{xz}^n \\ A_{yx}^n & A_{yy}^n & A_{yz}^n \\ 0 & 0 & 0 \end{pmatrix} \tag{A.41}$$

meanwhile

$$\hat{N} = \sum_n \mathbf{I}_n\cdot\mathbf{F}_n \tag{A.42}$$

is purely dynamic and

$$\mathbf{F}_n = \mathbf{A}_x^n \times \mathbf{A}_y^n = \begin{pmatrix} A_{xy}A_{yz} - A_{yy}A_{xz} \\ A_{yx}A_{xz} - A_{xx}A_{yz} \\ A_{xx}A_{yy} - A_{yx}A_{xy} \end{pmatrix} \tag{A.43}$$

As an example, we write the case of the NV center for low field,

$$\begin{aligned} E_{m_s}^{(2)} = & \sum_n \mathbf{B}\cdot\left(3m_s^2-2\right)\frac{\gamma_e}{\Delta}\mathbf{G}_n\cdot\mathbf{I}_n - \mathbf{I}_n\cdot m_s\frac{1}{2\Delta}\mathbf{F}_n \\ & + \frac{(3m_s^2-2)}{\Delta}\sum_{n>m}\mathbf{I}_n\cdot\mathbf{G}_n^T\mathbf{G}_m\cdot\mathbf{I}_m \end{aligned} \tag{A.44}$$

where the first term can be thought as an enhanced g-tensor

$$\Delta \mathbf{g}_n = \left(3m_s^2 - 2\right) \frac{\gamma_e}{\gamma_n \Delta} \mathbf{G}_n \tag{A.45}$$

Depending on the system under consideration the hyperfine interaction can be purely contact interaction as it is the case of quantum dots o purely dipolar as it would be the case for far enough nuclei in deep centers (where the wavefunction is very localized). Therefore, it is instructive to know the form of these matrices for these special cases. In the case of a purely contact interaction $A_{ij} = a\delta_{ij}$ we have,

$$\mathbf{G}_n = \begin{pmatrix} a & & \\ & a & \\ & & 0 \end{pmatrix} \qquad \mathbf{F}_n = \begin{pmatrix} 0 \\ 0 \\ a^2 \end{pmatrix} \qquad \mathbf{G}_n^T \mathbf{G}_m = \begin{pmatrix} a_n a_m & & \\ & a_n a_m & \\ & & 0 \end{pmatrix} \tag{A.46}$$

Meanwhile the purely dipolar case is pretty much filled everywhere.

Effective g-tensor

One of the consequences of this correction is an enhanced coupling between nuclei spins and the external magnetic field, which can be expressed in terms of an effective g-factor

$$g_n \left(m_s\right)_{ij} = g_c \delta_{ij} - \left(3|m_s| - 2\right) \frac{g_c \gamma_e}{2\Delta \gamma_N} \left(1 - \delta_{iz}\right) A_{ij}^n \tag{A.47}$$

or

$$g_n \left(m_s\right)_{ij} \quad = g_c \delta_{ij} + \Delta g_n \left(m_s\right)_{ij} \tag{A.48}$$

where

$$\Delta g_n \left(m_s\right)_{ij} \quad = -\left(3|m_s| - 2\right) \tfrac{g_c \gamma_e}{2\Delta \gamma_N} \left(1 - \delta_{iz}\right) \left(a_n \delta_{ij} + b_n \left(\delta_{ij} - 3\hat{r}_i \hat{r}_j\right)\right) \tag{A.49}$$

where a_n and b_n are the Fermi-contact and dipole-dipole term from the hyperfine interaction between the electronic spin state and the nuclear spin n.

Larmor frequency and Larmor vector

Besides the coupling between the external field and the nuclear spin operator, the latter also experiences an itself interaction mediated by the electronic spin. Both effects modify the Larmor frequency and the direction at which the nuclear spin precess. From Equations (A.30) and (A.31) we identify the complete effective coupling with the nuclear spin n as

$$-\sum_{ij}\mu_N g_n \left(m_S\right)_{ij} B_i I_j^n - m_s \left(2\Delta\right)^{-1} \sum_{ijk} \epsilon_{ijk} A_{xi}^n A_{yj}^n I_k^n \tag{A.50}$$

and including the rest of the couplings with the nuclear spin coming from (A.23), we can identify the following effective Larmor vector

$$\Omega_n \left(m_s\right)_k = -\sum_i \mu_N g_n \left(m_s\right)_{ik} B_i - \frac{m_s}{2\Delta} \sum_{ij} \epsilon_{ijk} A_{xi}^n A_{yj}^n - m_s A_{zk}^n. \tag{A.51}$$

This last equation tell us that each spin n has a particular Larmor frequency pointing in a particular direction. This will be very important when analyzing the nuclear decay. Corrections to the Larmor frequency decays exponentially and as r^{-3} and r^{-6}.

To see this result more clearly, let us analyze the case $m_s = 0$,

$$\Omega_n \left(m_s = 0\right)_j = -\sum_i \mu_N g_n \left(m_s = 0\right)_{ij} B_i \tag{A.52}$$

$$= -\sum_i \mu_N \left(g_c \delta_{ij} + \frac{g_c \gamma_e}{\Delta \gamma_N} \left(1 - \delta_{iz}\right) A_{ij} \right) B_i \tag{A.53}$$

$$\mathbf{\Omega}_n = -\mu_N \begin{pmatrix} B_x \\ B_y \\ B_z \end{pmatrix} - \frac{\gamma_e}{\Delta} \begin{pmatrix} A_{xx}B_x + A_{yx}B_y \\ A_{xy}B_x + A_{yy}B_y \\ A_{xz}B_x + A_{yz}B_y \end{pmatrix}. \tag{A.54}$$

Effective Nuclear Spin Interaction

Finally, the non-secular correction leads to an effective interaction between nuclei. From equations (A.30) and (A.31) we have that

$$\left(\Delta C_{nm}\right)_{ij} = \frac{\left(3m_s^2 - 2\right)}{2\Delta} \sum_{n \neq m ij} \left(A^n_{xi} A^m_{xj} + A^n_{yi} A^m_{yj} \right) I^n_i I^m_j. \tag{A.55}$$

which can be written as a function of the correction to the g factor $\left(\Delta g_n\right)_{ij}$,

$$\left(\Delta C_{nm}\right)_{ij} = \frac{1}{2\Delta \left(3|m_s| - 2\right)} \left(\frac{\Delta \gamma_N}{g_c \gamma_e} \right)^2 \sum_k \left(\Delta g_n^T\right)_{ik} \left(\Delta g_m\right)_{kj}. \tag{A.56}$$

The pre-factor before the summation has dimension of Hz and an approximate value of (in the case $m_s = 0$)

$$\frac{1}{4\Delta} \left(\frac{\Delta \gamma_N}{g_c \gamma_e} \right)^2 \sim \frac{1}{12} \ \texttt{kHz} \tag{A.57}$$

This constitute an important correction to the bare nuclei interaction, which is of the order of 2 kHz for nearest neighbors. Besides this important enhancement, the correction ΔC_{nm} does not depend on the relative position between nuclei, it depends on the relative positions between the electron and each nucleus. For nearest neighbor

nuclear spins right beside the defect, this new interaction is 1000 times grater than the bare interaction between them, however it decreases exponentially as the nuclear spins get away from the defect.

Appendix B

Supporting material for Chapter 3

B.1 Samples

AC magnetometry was performed at room temperature on nitrogen-vacancy (NV) centers in both a bulk single-crystal diamond sample (1mm x 1mm x 0.5mm, natural diamond with an atypically low nitrogen concentration) and in diamond nanocrystals (monocrystalline, synthetic diamonds, 30 nm mean diameter, purchased from Microdiamant AG, www.microdiamant.com, Switzerland) deposited on a quartz coverslip (see Figure B.1).

B.2 Confocal Setup

Single NV centers were isolated and probed via confocal microscopy (see Figure B.2). Phonon-mediated fluorescent emission (630 nm - 750 nm) was detected under coherent optical excitation ($\lambda = 532$ nm) using a single photon counting module

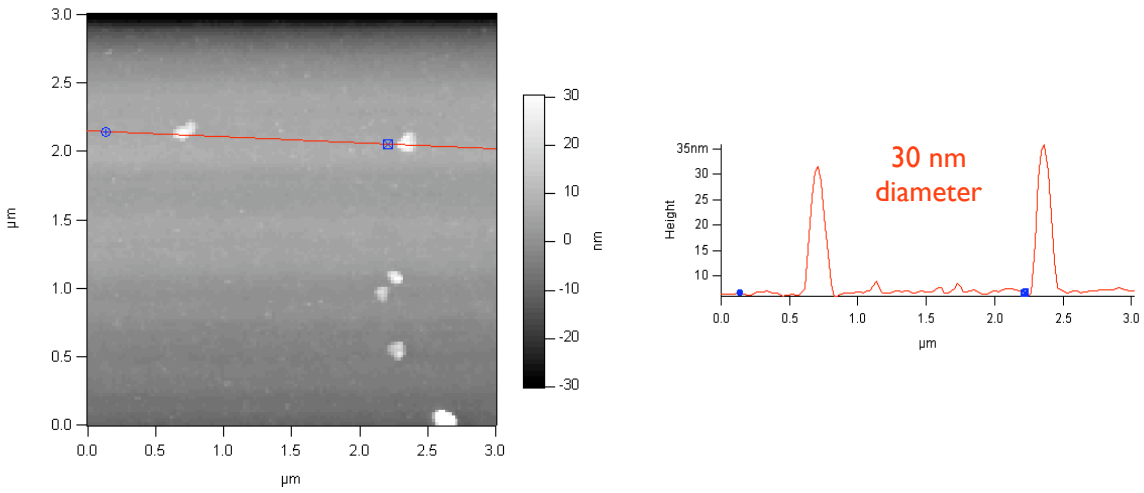

Figure B.1: **Atomic Force Microscope image of a diamond nanocrystal.** Typical image of a substrate where diamond nanocrystals were spin coated. The sizes for these nanocrsytals varies between 20 and 50 nm with an average size of 30 nm. As described in chapter 3, one of these crystals was used to sense AC magnetic field with 0.5 μT/Hz$^{1/2}$. Courtesy of Alexey Akimov.

(Perkin-Elmer SPCM-AQRH-13). The density of NV centers in both the bulk single-crystal and nanocrystal samples were sufficiently low that single bright spots (within the approximate confocal volume of 200 nm x 200 nm x 500 nm) were resolvable from the background fluorescence. As single spots in the confocal image may constitute many NV centers, single centers were identified by observing photon anitbunching in the measurement of the second-order correlation function. This emission was separated from the excitation path using a dichroic mirror, and also notch and longpass filters. Samples were imaged with an oil immersion objective lens (Nikon CFI Plan Fluor Series, NA=1.3, 100× magnification) over a 50 μm × 50 μm area in the plane normal to the optical path. Two galvanometer controlled mirrors steered the beam path for rapid imaging of this area. Experimental drifting of the focal plane due to

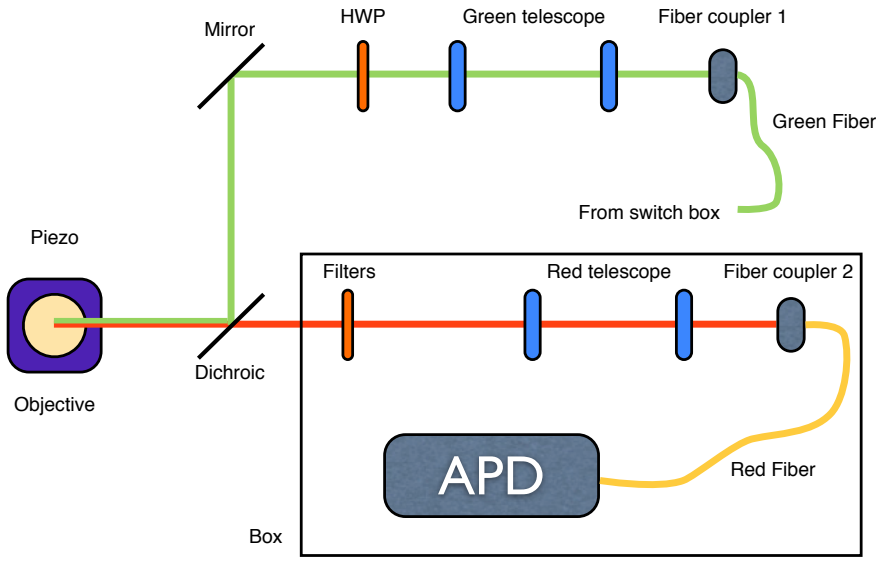

Figure B.2: **Schematic of a confocal setup for NV centers.** As explained in this appendix, an NV center is excited with green line on the absorption phonon side band and fluoresces in the range 637-800 nm. The green laser is delivered to the setup by a fiber coupler. A telescope is used so that the beam diameter of the green laser matches the aperture of the back of the objective in order to achieve an optimum resolution. An oil immersed objective with a numerical aperture of 1.3 is used to achieve ∼250 nm resolution which is nearly diffraction limited (∼ $\lambda/2$NA). Before reaching the objective, the green laser bounces a dichroic which reflects the green but transmits the red light. In this way, only the fluorescence of the NV center passes through the dichroic and reaches a black box where photons are counted. A set of filters inside the box can be used to narrow the fluorescence bandwidth to eliminated undesired light coming from the surface of the diamond, other impurities and even small green leakages. A telescope and a fiber coupler is used to better collect the fluorescence. Finally, the fiber is connected to a avalanche photon detector producing a TTL pulse that can be used to feed a counter.

thermal effects was compensated for using closed-loop feedback of the galvanometer and objective piezo voltages. Green laser pulses were generated using an acousto-optic modulator as shown on Figure B.3.

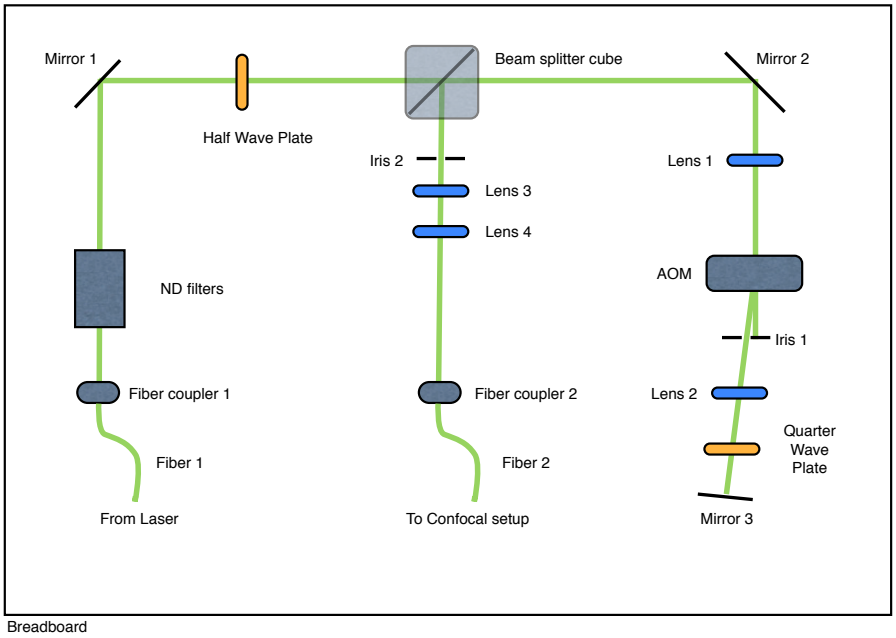

Figure B.3: **Laser switch box.** The green laser used to excite NV centers needs to be turned on/off faster than the polarization process of the center ($\approx$ 300 ns). For this reason, an acousto optic modulator (AOM) with a rise time of $\sim$10 ns is used in a double path configuration. The double path configuration is used to increase the extinction ratio between the on and off intensities achieving a ratio of the order of $I_{off}/I_{on} = 10^{-6}$. A low extinction ratio is important in long experiments so that the electronic spin is not re-polarized to the $m_s = 0$ state. The green beam coming from the laser passes through a polarizing beam splitter. Previously, a half wave plate is used to align the polarization of the laser with the beam splitter cube so that most of the light is transmitted. Then, the beam is focused by a lens on the AOM creating a first order diffracted beam which passes through an Iris (stopping the zeroth order beam). After Lens 2, the beam is brought to collimation again and bounces a mirror passing twice through a quarter wave plate. As a result, the beam that is coming back to the AOM has the opposite polarization to that of the incoming beam. Again, a first order Bragg diffracted beam is generated (a first order of the first order) that upon reaching the beam splitter cube will be totally reflected since it has the opposite polarization of the incoming beam. Finally, the beam passes through an iris and a telescope to better coupling the beam to an optical fiber.

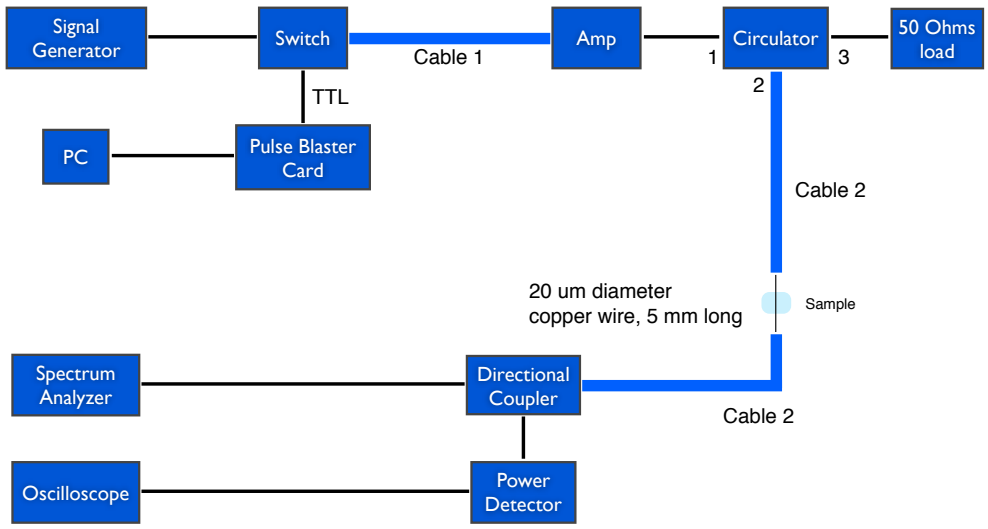

Figure B.4: **Microwave setup.** A signal generator provides a microwave signal in the range of 2-4 GHz to drive the electronic spins transition at low field (<500 G). The signal is turned on/off by a fast switch (6 ns rise time) controlled by a pulse blaster card which in turns is controlled by a computer. After the switch, the signal is brought to the setup through a low loss sma cable and then it is amplified by 30 dBm (a 1 W amplifier). For safety, the signal is connected to a circulator so that any reflected power from the setup reaches the 50 Ohms load instead of the amplifier. Otherwise, the reflected signal may damage the amplifier. This high power signal is then brought to the sample with another low loss cable. The signal is then connected to a thin 20 μm-diameter wire which in turns is connected to a cable for analysis purposes (optional), where the spectrum and power can be measured by a Spectrum Analyzer and an oscilloscope, respectively. To measure the spectrum, just a small signal is needed, obtained by unevenly splitting the signal with a directional coupler. A small signal (attenuated by 30 dBm) is connected to a spectrum analyzer and the rest is connected to a power detector generating a voltage inversely proportional to the power of the signal which can be monitored on an oscilloscope.

B.3 Single Center Electron Spin Resonance

The NV center $^3A_2$ ground state consists of two unpaired electrons in a triplet conguration leading to a zero-field splitting ($\Delta = 2.87$ GHz) between the $m_s = 0$ and $m_s = \pm 1$ sublevels. Coherent optical excitation at $\lambda = 532$ nm optically pumped

the ground state into its $m_s = 0$ sublevel. In addition, an external static magnetic field produced by a pair of Helmholtz coils split the degeneracy between the $m_s = \pm 1$ states. It was then possible to selectively address transitions between the $m_s = 0$ and $m_s = 1$ (or $m_s = -1$) states with microwave radiation (see Figure 3.1) and manipulate a two-level subspace of the spin triplet (e.g., with spin-echo pulse sequences). Microwave radiation was applied by using the magnetic field emanating from a 20 μm wire placed on the surface of the samples.

The excited (^3E) state decay rates, also responsible for optical pumping, provided a means for spin-sensitive detection, as the rate of fluorescence was reduced for the $m_s = \pm 1$ states compared to the $m_s = 0$ states, with $> 35\%$ contrast. The spin state in the ground electronic state was measured by pulsing on green excitation and monitoring the total number of photons collected within the optimal measurement interval, 324 ns. A 300 MHz PulseBlasterESR pulse generator was employed for timing the triggering of counters, microwave pulses, the AC magnetic field, and the excitation laser. Microwave pulses were provided by gating the output of a frequency synthesizer with a microwave switch (see Figure B.3). The π and $\pi/2$ pulses used for the spin-echo sequence were calibrated from the Rabi nutation curves between the two spin states.

B.4 AC magnetometry

As described in Figure 3.2 and in Ref. [25], demonstration magnetometer measurements were performed for an externally applied AC magnetic field with amplitude B_{AC}, frequency ν, and phase ϕ_{AC} during a cycle of a spin-echo sequence with a period

τ. The accumulated phase of the spin superposition state,

$$\delta\phi = \frac{4\gamma B_{AC}}{2\pi\nu}\sin^2[\frac{\pi\nu\tau}{2}]\cos[\pi\nu\tau + \phi_{AC}] \tag{B.1}$$

contained information about the projection of the AC magnetic field amplitude onto the quantization axis of the electronic spin, corresponding to a vector magnetometer. Oscillatory magnetic fields from 1-10 kHz were generated by modulating the current through a Helmholtz pair also used to apply a bias DC magnetic field. For application of higher frequency AC fields (100-300 kHz), a single coil (60 turns) was resonantly driven and placed near the sample.

The measured signal intensity S_B was a function of the accumulated phase $\delta\phi$, as given by the probability to be in the $m_s = 0$ state after the spin-echo pulse sequence: $S_B \propto P_0(B_{AC}) = \frac{1}{2}(1 + F(\tau)\cos[\delta\phi])$. Ideally, for a single-shot measurement of B_{AC} the sensitivity was maximized for a particular ν by setting $\tau = 1/\nu$. In practice, many spin-echo cycles were averaged to reduce the uncertainty in photon statistics given the low single-shot count rate. To this end, the period of the entire measurement sequence (including polarization and readout, see Figure 3.2) was matched to $1/\nu$ in order to avoid multiple offset phases ϕ_{AC} when the periods were incommensurate. The dependence on ϕ_{AC} was removed entirely by appropriately shifting the time origin of the measurement pulse train. As the polarization ($\tau_p = 1$ μs) and readout ($\tau_r = 3$ μs) periods were short compared to the oscillation periods for typical 1-10 kHz AC magnetic fields, this choice introduced a slight deviation ϵ from the optimal $\delta\phi$, as $\tau_p + \tau_r + \tau = 1/\nu \Rightarrow \tau\nu = 1 - \epsilon$. The overall sensitivity was thus slightly reduced from its optimal value as $1 - \mathcal{O}(\epsilon^2)$. For all experiments presented here, $\nu\tau = 0.88$ was used. The envelope of the spin-echo signal, $F(\tau)$ (e.g., see Figure 3.4)

was modeled with an exponential decay modulated by the effect of a pair of nearby strongly interacting ^{13}C nuclear spins. In this model[85], $F(\tau) = \exp(-(\tau/T_2)^4)(1 - \frac{(a^2-b^2)}{a^2}\sin^2 a\tau \sin^2 b\tau)$; where for the data in Figure 3.4 we found $T_2 = 676$ μs, $b = 478$ Hz (corresponding to the dipolar interaction between the two nuclei) and $a = 626$ Hz (corresponding to the interactions between the nuclei and the NV spin). Using these experimentally determined parameters, the above model provided a prediction for the the magnetometer sensitivity[25] $\eta_{AC} = \frac{\pi\hbar}{g\mu_B C\sqrt{\nu F(1/\nu)}}$ as a function of frequency (solid curve in Figure 3.6a), where $g \approx 2$ is the electron g-factor, μ_B is the Bohr magneton, and $C^{-1} = \sqrt{1 + 2\frac{(a_0+a_1+a_0a_1)}{(a_0-a_1)^2}}$ is a factor that estimates[25] the photon shot-noise when the average photon number during the readout window of 324 ns is much less than 1. The values $a_0 = 0.03 \pm 0.006$ and $a_1 = 0.018 \pm 0.004$ were the average number of detected photons for the the electronic spin states $m_S = 0$ and $m_S = \pm 1$, respectively.

Appendix C

Supporting material for Chapter 4

C.1 Experimental Setup

We isolate single NV centers using standard confocal microscopy techniques. The NV centers are optically excited using green light (λ_{ex} = 532 nm, sourced from a Coherent Compass 315M-100 laser). We focus the green spot to a nearly diffraction-limited spot-size using an oil immersion objective (Nikon CFI Apochromat TIRF 100X, NA = 1.49) focused to a depth of up to 50 μm below the diamond surface. Fluorescence emission from the lowest lying excited triplet state (^3E level of NV [111]) is collected within the phonon sideband, extending from 650 nm to 750 nm. This light is focused onto a single-mode optical fiber (NA=.12, MFD = 4.3μm), which acts as a small aperture spatial filter and rejects light emanating from outside the focal plane. Photons incident on the fiber are detected using an avalanche photodiode module (PerkinElmer SPCM-AQR-13).

In order to find a single NV center within the diamond, we image a 50μm x 50μm

area within a fixed focal plane by changing the incidence angle of the excitation light wavefronts at the objective. This is accomplished by using a fast, closed-loop XY scanning mirror system (Cambridge Technology, 6215H scanning mirrors). Different focal planes are examined by moving the entire sample, along the tube axis of the objective, using a closed-loop z-axis piezo stage (Physique Instrument, P-620.ZCD). The density of NV centers within the sample is small enough that we can resolve single bright spots and collect light from these emitters. In order to verify that these spots are single centers, we measure the autocorrelation function of the emitted light in a Hanbury-Brown-Twiss style setup ($g^{(2)}(\tau)$). Furthermore, we monitor the fluorescence intensity under resonant microwave excitation to verify that these single emitters are indeed nitrogen-vacancy centers, with a finite ESR response near 2.87 GHz at zero applied magnetic field. If an NV center is strongly coupled to a ^{13}C spin within the lattice, this appears as an additional splitting in the the spectrum of microwave response.

The nitrogen-vacancy color centers used for our repetitive readout experiments are found within a bulk, single crystal type IIa natural diamond with a remarkably low native nitrogen impurity concentration. The lack of paramagnetic defects in this sample is believed to be the primary reason for long ($> 500\mu s$) spin dephasing times of the NV center electronic spin. The ^{13}C nuclei within the lattice are randomly distributed and have a natural isotope fraction, 1.1% relative to all carbon nuclei.

Spin Control of the NV centers

At room temperature, the three spin eigenstates of the NV center ($|0\rangle_e$, $|1\rangle_e$, and $|-1\rangle_e$) are equally populated. Optical excitation at 532 nm, excites the ground state triplet of the NV to an excited vibronic state, which decays to the first excited triplet state. The population in these spin states will either radiatively decay back to the ground state or undergo an intersystem crossover to a metastable singlet state, which decays into the $|0\rangle_e$ state. This provides a mechanism for optical pumping of the NV center spin. After 1 μs period of illumination (near optical saturation) the $|\pm 1\rangle_e$ states are optically pumped to the $|0\rangle_e$ state in excess of 95%. This conveniently prepares an initial state $|0\rangle_e$ after readout, but barely perturbs the nuclear spin state.

We apply microwave and radiofrequency (RF) fields to individual NV centers by driving a small copper wire (15μm diameter) placed on the diamond surface and secured to a 50Ω impedance matched microstrip transmission line. Three separate frequency synthesizers are used to generate the three frequencies needed for obtain full spin control of the electronic-nuclear spin system, identified as MW1, MW2 and RF in Figure 4.1D. These values are cited below. Separate amplifiers for the microwave (OphirRF, S-Band, 15W, Model XRF738) and RF (ENI, 10W, Model 310-L) allow us to generate magnetic fields of about 10 gauss. Short microwave pulses, on the order of 10ns, are generated by gating an SPST switch with an extremely short rise time (Custom Microwave Components S0947A-02, rise time 3ns). Timing of the counter gating, RF and microwave pulses and the acousto-optic modulator (AOM) is coordinated by a multiple channel TTL pulse generator (SpinCore PulseBlaster ESR-Pro, 400MHz), with up to 2.5ns timing resolution.

For pulsed experiments, measurement of the spin state involves counting the NV fluorescent photons after optical pumping. This involves monitoring the phonon side band fluorescence under optical excitation within 100-500ns [111]. Short optical pulses are achieved using an AOM with a digital driver (Isomet 1250C-848) in a double-pass setup [150]. Rise times of the optical pulses are about 20ns and thus enable sufficient contrast between the two spin states.

In order to remove systematic fluctuations in the counting rates of the fluorescent photons (e.g., heating and defocusing of the NV due to long microwave pulses), we take a series of measurements before *each* run of the experiment. Prior to any of our repeated readout experiments, we measure the fluorescence after the following microwave pulse configurations: (1) no microwave pulse, (2) a single MW1 π-pulse, (3) a single MW2 π-pulse, and (4) a MW1 and MW2 π-pulse. Conditions (1) and (4) set the maximum and minimum count rates for the NV center readout and set the relative scale for the Rabi experiments (Figure 4.1).

Random, slow drifting of the counting rates of the NV center (e.g., due to day/night temperature cycles or mechanical perturbations) are accounted for by a software-based feedback mechanism. Prior to each experimental average ($\sim 10^5$ repetitions), we take a reference count rate of the NV fluorescence. If this is outside an allowed threshold, we vary the scanning mirror and piezo stage voltages in order to maximize the counting rate. In this way, defocusing of the NV center can be corrected and stabilized. Over the course of six months, such tracking has enabled us to study the same center exclusively.

Magnetic field, microwave and RF control pulses

We use three sets of orthogonal coil windings in a quasi-Helmholtz configuration to apply the static magnetic field for tuning the spin resonance of the NV. Each winding consists of roughly 100 turns and each pair can generate up to 40 gauss in three orthogonal directions when driven with 4A, direct current. By independently changing the current supplied to each coil pair, we can align the magnetic field vector relative to the axis of symmetry of the NV center ($\hat{z}$). Coarse measurements of the magnetic field amplitudes are made using a three-axis Hall sensor (Ametes MFS-3A). For more precise alignment, we measure the ESR response of the NV in both a continuous wave and pulsed (electron spin echo envelope modulation) manner, as described below.

As shown in Figure 4.1A, we use MW1 to drive the transition between $|0\rangle_e|\downarrow\rangle_{n1}$ and $|1\rangle_e|\downarrow\rangle_{n1}$, and MW2 for the transition between $|0\rangle_e|\uparrow\rangle_{n1}$ and $|1\rangle_e|\uparrow\rangle_{n1}$. The two transitions differ in energy by $\delta = (2\pi) \times 13.675\,(1)$ MHz, mostly due to the hyperfine interaction between spins $\mathbf{e}$ and $\mathbf{n}_1$. When the microwave (MW) Rabi frequency Ω_{MW} is comparable to the detuning δ, the effect of off-resonant driving should be considered. For example, when trying to drive microwave transitions for only levels with the nuclear spin in $|\downarrow\rangle_{n1}$, we may also change the populations for the $|\uparrow\rangle_{n1}$ levels. Fortunately, if we are only interested in π-pulses, the effect of off-resonant driving can be suppressed. We choose the bare MW Rabi frequency $\Omega_{MW} = \delta/\sqrt{3} = (2\pi) \times 7.89$ MHz with pulse duration π/Ω_{MW}, which performs a π rotation for the resonant transition. For the δ-detuned transition, the effective Rabi frequency is $\sqrt{\Omega_{MW}^2 + \delta^2} = \sqrt{\Omega_{MW}^2 + 3\Omega_{MW}^2} = 2\Omega_{MW}$, and the operation gives a

(trivial) 2π rotation. Thus, in principle, we can achieve a perfect $C_{n1}NOT_e$ gate with an MW1 (or MW2) π pulse, despite the finite detuning δ.

For our experiment the two microwave resonance frequencies are $\nu_{MW1} = 2.962$ GHz and $\nu_{MW2} = 2.949$ GHz. The radiofrequency field is tuned to the nuclear spin splitting at $\nu_{RF} = 13.675$ MHz. We note that the duration for a π-pulse at this frequency is about 5μs, which indicates a Rabi frequency of almost 100 kHz. This nuclear Rabi frequency is enhanced from that of a bare ^{13}C nucleus ($\gamma_C = 1.1$kHz/ Gauss) due to the pseudo-nuclear Zeeman effect [151]. This effect enhances transitions of the nuclear spin because of the strong hyperfine coupling between the nucleus and the NV electronic spin.

In addition, we must also consider the presence of a ^{14}N nuclear spin, with $I = 1$ and hyperfine coupling strength $\alpha_N = (2\pi) \times 2.1\,(1)$ MHz, which gives the triplet splitting for both transition lines in the ESR spectrum (Figure C.1). At room temperature, the ^{14}N nuclear spin is unpolarized (i.e., in a completely mixed state), with equal probability in the spin states $I_z = 0, \pm 1$.

The splitting associated with ^{14}N nuclear spin can introduce a small detuning $\pm\alpha_N$ to the resonant transition, resulting in an error probability $\sim (\alpha_N/\Omega_{MW})^2$. We estimate the average error probability for the MW π-pulse to be $\varepsilon_{\text{res}}^{MW} \approx 0.07$ for the resonant transition. In addition, the splitting associated with ^{14}N can also affect the δ-detuned transition. In the presence of extra detuning $\pm\alpha_N$, the 2π rotation for the δ-detuned transition is no longer perfect. The estimated average error probability for the MW π-pulse is $\varepsilon_{\text{det}}^{MW} \approx 0.01$ for the δ-detuned transition.

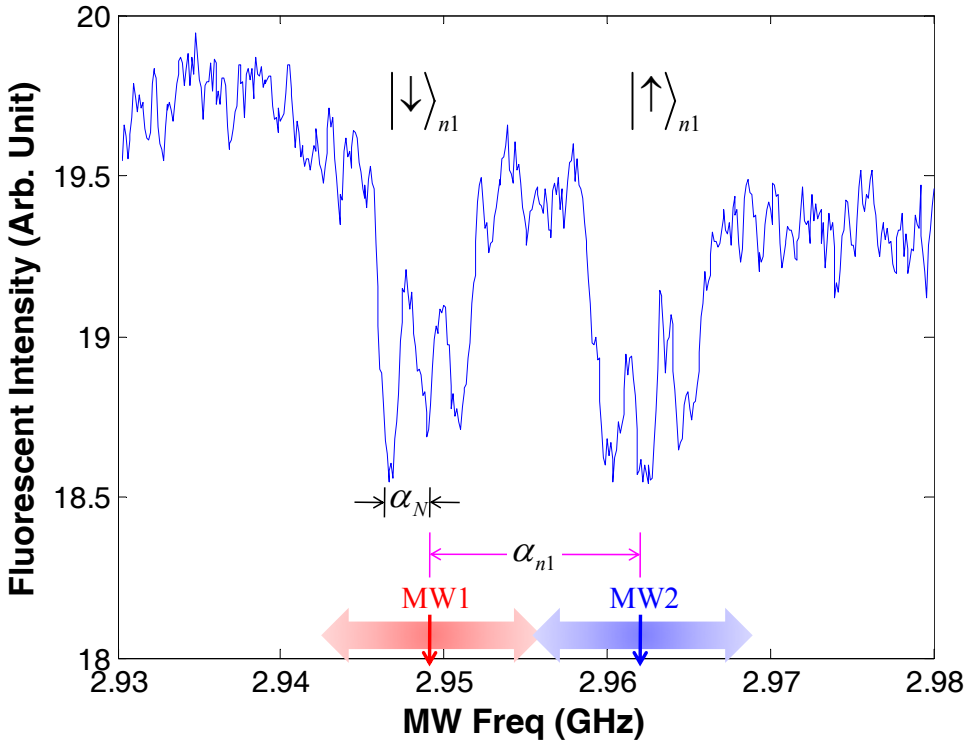

Figure C.1: Fluorescence detected electron spin resonance of the NV center. We monitor the fluorescence under optical excitation at λ_{ex} while sweeping the carrier microwave frequency. When the resonance condition is met, we see a drop in the count rate, signifying a transfer of population to the $m_s = \pm 1$ states. Here we show only the portion of the spectrum involving transitions between $m_s = 0$ and 1. In the absence of any nuclear spins, this condition would occur at single frequency, but is split due to the hyperfine interaction with nearby nuclear spins. The six lines shown correspond to coupling of the NV to a nearby ^{13}C ($\mathbf{n_1}, I = 1/2$) and ^{14}N ($I = 1$) with hyperfine couplings α_N and α_{n1} respectively. The two microwave driving frequencies (MW1 and MW2) address the $|\downarrow\rangle_{n1}$ and $|\uparrow\rangle_{n1}$ manifolds and differ in frequency by α_{n1}. The MW Rabi frequency ($\Omega = 7.89$ MHz) is sufficiently large to drive the triplet lineshape for each manifold.

C.2 Effective Hamiltonian

In this section, we write the effective hamiltonian using time-independent perturbation theory. We then study the hyperfine coupling associated with the first nuclear spin ($\mathbf{n}_1$) to justify the claim that the quantization axis of spin $\mathbf{n}_1$ is effectively the

same when spin **e** is $|m_s = 0\rangle_e$ or $|m_s = 1\rangle_e$. Finally, we use the effective Hamiltonian to study the electron-mediated coupling between the two nuclear spins $\mathbf{n}_1$ and $\mathbf{n}_2$.

The effective hamiltonian for the electronic spin and nuclear spins can be obtained from second order perturbation theory (see Equation A.44 in Appendix A.4), which we copy here for the convenience of the reader,

$$\begin{aligned} H_{nuc}^{m_s} &= \sum_n \gamma_0 \mathbf{B}\cdot\mathbf{I}_n + m_s \mathbf{A}_z^n \cdot \mathbf{I}_n + \mathbf{B}\cdot\left(3m_s^2-2\right)\frac{\gamma_e}{\Delta}\mathbf{G}_n\cdot\mathbf{I}_n - \mathbf{I}_n\cdot m_s\frac{1}{2\Delta}\mathbf{F}_n \\ &+ \sum_{n>m}\mathbf{I}_n\cdot\mathbf{C}_{nm}\cdot\mathbf{I}_m + \frac{(3m_s^2-2)}{\Delta}\sum_{n>m}\mathbf{I}_n\cdot\mathbf{G}_n^T\mathbf{G}_m\cdot\mathbf{I}_m \end{aligned} \tag{C.1}$$

where

$$\mathbf{G}_n = \begin{pmatrix} \mathbf{A}_x^n \\ \mathbf{A}_y^n \\ 0 \end{pmatrix} = \begin{pmatrix} A_{xx}^n & A_{xy}^n & A_{xz}^n \\ A_{yx}^n & A_{yy}^n & A_{yz}^n \\ 0 & 0 & 0 \end{pmatrix} \tag{C.2}$$

and

$$\mathbf{F}_n = \mathbf{A}_x^n \times \mathbf{A}_y^n = \begin{pmatrix} A_{xy}A_{yz} - A_{yy}A_{xz} \\ A_{yx}A_{xz} - A_{xx}A_{yz} \\ A_{xx}A_{yy} - A_{yx}A_{xy} \end{pmatrix} \tag{C.3}$$

The third term in Equation (C.1) is the pseudo nuclear Zeeman effect, arising from the enhancement of the external magnetic field due to the hyperfine interaction [151]. The enhancement vanishes when we carefully align the external magnetic field along the NV axis (i.e., $\mathbf{B} = B_z\vec{e}_z$). This is because $\vec{e}_z\cdot\mathbf{G}_n \equiv 0$ (i.e., all elements vanish in the third row of Equation (C.2)), and consequently there is *no enhancement* for external magnetic field along the $\hat{z}$ (i.e., NV) axis. Thus, all ^{13}C nuclear spins share

the *same* quantization axis (i.e., along the NV axis) and they have the *same* Zeeman splitting $\omega_0 = \gamma_0 B_z \approx 32\,(1)$ kHz, regardless of the individual hyperfine interactions [11]. The last term in Equation (C.1) is the electron-mediated interaction among the nuclear spins, with the correction to the dipolar interaction tensor.

For the $m_s = 0$ subspace, the effective Hamiltonian is

$$H_{nuc}^{m_s=0} = -\sum_{\mathsf{j}} \omega_0 I_z^{\mathsf{j}} + \sum_{\mathsf{j}>\mathsf{k}} \mathbf{I}_j \cdot \tilde{\mathbf{C}}_{jk}(0) \cdot \mathbf{I}_k. \tag{C.4}$$

where $\tilde{\mathbf{C}}_{nm}(m_s) = \mathbf{C}_{nm} + \frac{\left(3m_s^2-2\right)}{\Delta}\mathbf{G}_n^T\mathbf{G}_m$. When the Zeeman splitting is large (i.e., $\omega_0 \gg \tilde{C}_{mn}^{\mathsf{j},\mathsf{k}}\,(0)$), we neglect the non-secular terms of $\tilde{\mathbf{C}}$ and obtain the simplified Hamiltonian for $m_s = 0$:

$$H_{nuc}^{m_s=0} \approx -\sum_{\mathsf{j}} \omega_0 I_z^{\mathsf{j}} + \sum_{\mathsf{j}>\mathsf{k}} I_z^{\mathsf{j}} \tilde{C}_{zz}^{\mathsf{j},\mathsf{k}}\,(0)\, I_z^{\mathsf{k}} + \sum_{\mathsf{j}>\mathsf{k}} \left(b^{\mathsf{j},\mathsf{k}} I_+^{\mathsf{j}} I_-^{\mathsf{k}} + \left(b^{\mathsf{j},\mathsf{k}}\right)^* I_-^{\mathsf{j}} I_+^{\mathsf{k}} \right), \tag{C.5}$$

where $b^{\mathsf{j},\mathsf{k}} = \frac{1}{4}\left(\tilde{C}_{xx}^{\mathsf{j},\mathsf{k}} + \tilde{C}_{yy}^{\mathsf{j},\mathsf{k}} + i\tilde{C}_{xy}^{\mathsf{j},\mathsf{k}} - i\tilde{C}_{yx}^{\mathsf{j},\mathsf{k}}\right)$. Both Ising coupling and flip-flop coupling may exist for the $m_s = 0$ subspace.

For the $m_s = 1$ subspace, the effective Hamiltonian is

$$H_{nuc}^{m_s=1} = -\sum_{\mathsf{j}} \omega_0 I_z^{\mathsf{j}} + \sum_{n=x,y,z} A_{zn}^{\mathsf{j}} I_n^{\mathsf{j}} + \sum_{\mathsf{j}>\mathsf{k}} \sum_{m,n=x,y,z} I_m^{\mathsf{j}} \tilde{C}_{mn}^{\mathsf{j},\mathsf{k}}\,(1)\, I_n^{\mathsf{k}}. \tag{C.6}$$

where we have dropped the constant $\Delta - \gamma_e B_z$ term for simplicity. The first two terms imply that the j-th nuclear spin precesses around the vector $\vec{\omega}^{\mathsf{j}} \equiv -\omega_0 \vec{e}_z + \sum_{n=x,y,z} A_{zn}^{\mathsf{j}} \vec{e}_n$, and the quantization axis is $\vec{e}_z^{\,\mathsf{j}} \equiv \vec{\omega}^{\mathsf{j}} / \left|\vec{\omega}^{\mathsf{j}}\right|$. When the hyperfine interactions are sufficiently different $\left|\vec{\omega}^{\mathsf{j}} - \vec{\omega}^{\mathsf{k}}\right| \gg \tilde{C}_{mn}^{\mathsf{j},\mathsf{k}}\,(1)$, all couplings between the

[11] Note that our earlier experiment [39] explores a different regime, where the external magnetic field has a transverse component with respect to the NV axis. Because of the anisotropy of the g-tensor for proximal nuclear spins, the transverse component can be enhanced depending on the hyperfine interaction. Thus, the proximal nuclear spins can have very different quantization axes, and different effective Zeeman splittings as well [53].

nuclear spins are suppressed except for the Ising coupling. The simplified Hamitonian for $m_s = 1$ is:

$$H_{nuc}^{m_s=1} \approx \sum_{\mathsf{j}} \left|\vec{\omega}^{\mathsf{j}}\right| I_{z_{\mathsf{j}}}^{\mathsf{j}} + \sum_{\mathsf{j}>\mathsf{k}} I_{z_{\mathsf{j}}}^{\mathsf{j}} \tilde{C}_{z_{\mathsf{j}}z_{\mathsf{k}}}^{\mathsf{j},\mathsf{k}}(1)\, I_{z_{\mathsf{k}}}^{\mathsf{k}}, \tag{C.7}$$

where $\tilde{C}_{z_{\mathsf{j}}z_{\mathsf{k}}}^{\mathsf{j},\mathsf{k}}(1) = \sum_{m,n=x,y,z} \left(\vec{e}_z^{\mathsf{j}}\right)_m \cdot \tilde{C}_{mn}^{\mathsf{j},\mathsf{k}}(1) \cdot \left(\vec{e}_z^{\mathsf{k}}\right)_m$. For example, with only two proximal nuclear spins $\mathbf{n}_1$ and $\mathbf{n}_2$, and $|\vec{\omega}^1 - \vec{\omega}^2| \gg \tilde{C}_{mn}^{1,2}(1)$,

$$H_{nuc}^{m_s=1} \approx \left|\vec{\omega}^1\right| I_{z_1}^1 + \left|\vec{\omega}^2\right| I_{z_2}^2 + I_{z_1}^1 \tilde{C}_{z_1z_2}^{1,2}(1)\, I_{z_2}^2. \tag{C.8}$$

If spin $\mathbf{n}_2$ is in the completely mixed state, then spin $\mathbf{n}_1$ has two possible energy splittings $|\vec{\omega}^1| \pm \frac{1}{2}\tilde{C}_{z_1z_2}^{1,2}(1)$. With a nuclear spin Ramsey experiment (Figure C.2), we should be able to either resolve such energy splitting (by observing the beating at frequency $\tilde{C}_{z_1z_2}^{1,2}(1)$) or give an upper bound on the magnitude of $\tilde{C}_{z_1z_2}^{1,2}(1)$.

Hyperfine Coupling for the First Nuclear Spin

We now justify the claim that spin $\mathbf{n}_1$ has approximately the same quantization axis for both $m_s = 0$ and $m_s = 1$ subspaces. Since the static magnetic field is along the NV axis $\vec{B} = B_z\vec{e}_z$, there is no enhancement from the g-tensor. Considering only one nuclear spin $\mathbf{n}_1$, we may reduce Equation (C.6) to

$$H^{1,m_s} = -\omega_0 I_z^1 + m_s \sum_n A_{zn}^1 I_n^1 \tag{C.9}$$

For the $m_s = 0$ subspace, spin $\mathbf{n}_1$ has the quantization axis $\hat{n}_{m_s=0} = \vec{e}_z$. For $m_s = 1$ subspace, we may calculate the quantization axis $\hat{n}_{m_s=1}$ using the hyperfine tensor $A_{mn}^{(1)}$ associated with spin $\mathbf{n}_1$.

If the hyperfine coupling is due to the contact interaction that is isotropic, the hyperfine tensor is proportional to the identity matrix, $A_{mn}^1 \propto \delta_{mn}$, and the relevant

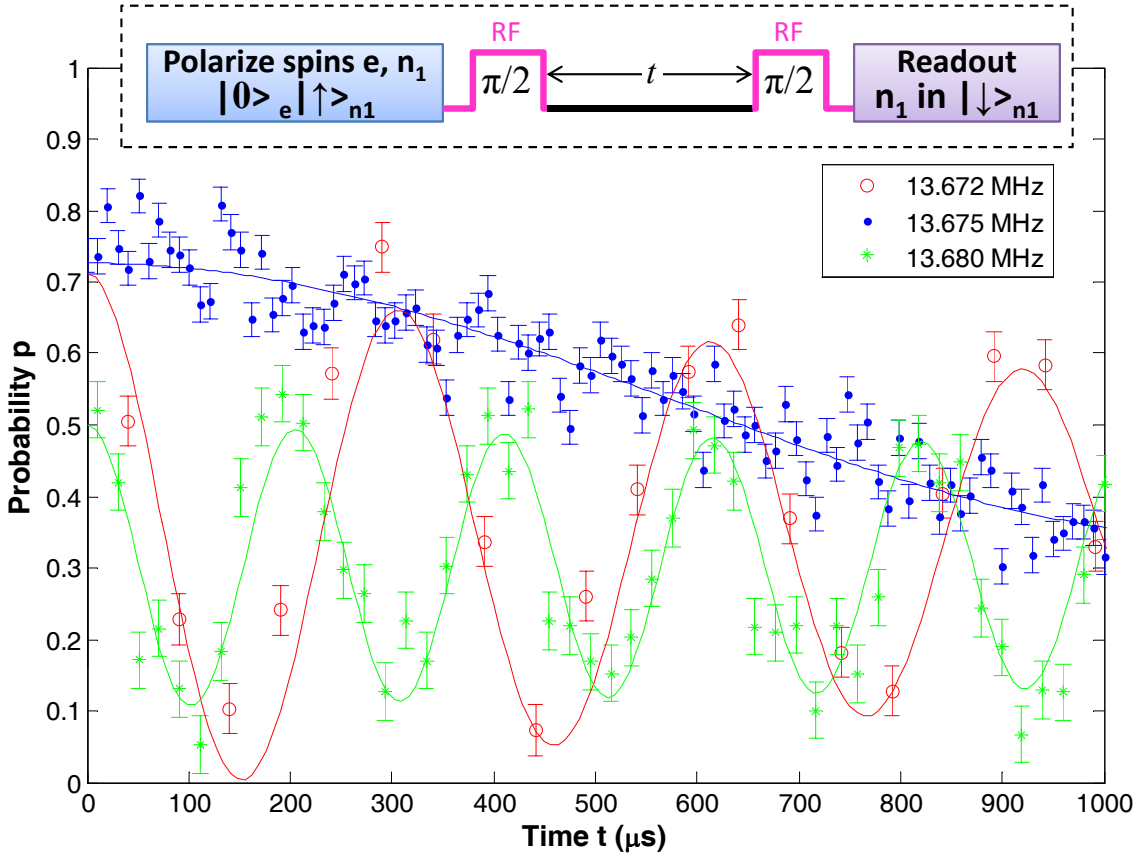

Figure C.2: Ramsey fringes for the nuclear spin $\mathbf{n}_1$. The operations for the nuclear Ramsey experiment are given in the dashed box. Three difference frequencies $\nu = 13.672, 13.675$, and 13.680 MHz are used for the RF field. The frequency for the Ramsey fringes is determined by the detuning of the RF field $\nu - \nu_0$, where $\nu_0 = 13.675\,(1)$ MHz. There is no significant decay in the amplitude of the Ramsey fringes up to 1 ms.

Hamiltonian can be reduced to $-\mu_n B_z I_z^1 + S_z A_{zz}^1 I_z^1$. This implies that the quantization axis $\hat{n}_{m_s=1} = \vec{e}_z$ is also along the NV axis. If the hyperfine coupling also contains a dipolar interaction that is anisotropic, the hyperfine tensor can be characterized by three principle axes with associated principle values. If one of the principle axis is fairly close to the NV axis and the three principle values are also quite similar, then the quantization axis of $\mathbf{n}_1$ can be still very close to the NV axis.

The hyperfine tensors have be calculated with density functional theory (DFT) [18] and obtained from the CW ensemble EPR spectra measurements [152]. In our experiment, we can measured the projection of the hyperfine tensor along the NV axis

$$A_z^1 \equiv \left|A_{zx}^1 \vec{e}_x + A_{zy}^1 \vec{e}_y + A_{zz}^1 \vec{e}_z\right| = \sqrt{\left(A_{zx}^1\right)^2 + \left(A_{zy}^1\right)^2 + \left(A_{zz}^1\right)^2}. \tag{C.10}$$

We perform a Ramsey experiment for spin $\mathbf{n}_1$ in $m_s = 1$ subspace, which measures the level splitting between $|1\rangle_e |\downarrow\rangle_{n1}$ and $|1\rangle_e |\uparrow\rangle_{n1}$ to be 13.675 (1) MHz (see Figure C.2). This value also includes $\omega_0 = \pm 32\,(1)$ kHz contribution of Zeeman splitting due to 30 gauss magnetic field parallel/antiparallel to the NV axis [53]. Thus, the projection of the hyperfine tensor along the NV axis is $A_z^1 = 13.675\,(1) \pm 0.032\,(1)$ MHz. The measured values match those reported by Felton et al. in bulk ESR studies [152]. The reported hyperfine tensor implies that the quantization axis $\hat{n}_{m_s=1} = \sin\delta\ \vec{e}_x + \cos\delta\ \vec{e}_z$ for $|m_s = 1\rangle_e$, where $\delta = \arctan\frac{A_{xz}^1}{A_{zz}^1} \approx 6.7^\circ$ is the angle between $\hat{n}_{m_s=0}$ and $\hat{n}_{m_s=1}$. Thus, the nuclear spin eigenstates for $m_s = 1$ subspace differ from the nuclear spin eigenstates for $m_s = 1$ subspace by a small angle δ. The difference between these two state is $\sin^2\delta \approx 0.007$, which is too small to be resolved with the current precision. Therefore, with our measurement precession, we have justified to claim that the quantization axis of the nuclear spin $\mathbf{n}_1$ almost does not depend on the electronic spin state $|m_s = 0\rangle_e$ or $|m_s = 1\rangle_e$. We may use the simple notation of $|0\rangle_e |\downarrow\rangle_{n1}, |0\rangle_e |\uparrow\rangle_{n1}, |1\rangle_e |\downarrow\rangle_{n1}$, and $|1\rangle_e |\uparrow\rangle_{n1}$ provides a good approximation for the eigenstates of the Hamiltonian in Equation (C.9).

Spin Flip-Flop Interaction between Nuclear Spins

We now consider the interaction between two nuclear spins $\mathbf{n}_1$ and $\mathbf{n}_2$. According to Equation (C.5), the effective secular spin Hamiltonian between spins $\mathbf{n}_1$ and $\mathbf{n}_2$ for $m_s = 0$ subspace is

$$H_{nuc}^{m_s=0} = \omega_0 I_z^1 + \omega_0 I_z^2 + \tilde{C}_{zz}^{1,2} I_1^1 I_z^2 + b^{1,2}(I_+^1 I_-^2 + I_-^1 I_+^2),$$

where we choose $b^{1,2}$ real by absorbing the complex phase into I_+^1. Experimentally, we estimate $\tilde{C}_{zz}^{1,2} \lesssim 0.3$ kHz from the nuclear spin Ramsey experiment (as the Ramsey fringes can be observed even up to 3 ms (Figure C.2)), which is one or two orders of magnitude smaller than $b^{1,2} = 4.27\,(3)$ kHz or $\omega_0 = 32\,(2)$ kHz, which corresponds to magnetic field of ~ 30 gauss. The observation is also consistent with the theoretical estimate from the hyperfine tensors [12]. For simplicity, we will neglect the $\tilde{C}_{zz}^{1,2}$ term and consider the following Hamiltonian:

$$H_f = \omega_0 \left(I_z^1 + I_z^2\right) + b(I_+^1 I_-^2 + I_-^1 I_+^2), \tag{C.11}$$

where $b = b^{1,2} = \left|\frac{1}{4}\left(\tilde{C}_{xx}^{1,2} + \tilde{C}_{yy}^{1,2} + i\tilde{C}_{xy}^{1,2} - i\tilde{C}_{yx}^{1,2}\right)\right|$. Neglecting $\tilde{C}_{zz}^{1,2}$ may introduce an error with probability $\left(\tilde{C}_{zz}^{1,2}/b\right)^2 \lesssim 1\%$, which is actually small compared to other imperfections. In principle, we may also use quantum control techniques [109] to completely compensate the deviation due to finite $\tilde{C}_{zz}^{1,2}$.

The nuclear spins $\mathbf{n}_1$ and $\mathbf{n}_2$ have initial poalrization $p_{n_1} \equiv p_{n_1,\uparrow} - p_{n_1,\downarrow}$ and $p_{n_2} \equiv p_{n_2,\uparrow} - p_{n_2,\downarrow}$, respectively. The initial densitiy matrix of the two nuclear spins

[12] The hyperfine tensor for n_1 is almost diagonal, with off-diagonal matrix elements much less than the diagonal ones (e.g., $A_{xz}^1 \ll A_{xx}^1, A_{yy}^1, \alpha_{zz}^1$). This suggests that it is very likely that $\delta C_{zz}^{1,2} \ll \delta C_{xx}^{1,2}, \delta C_{yy}^{1,2}$ for the electron-mediated nuclear spin coupling between n_1 and n_2.

is $\rho_0 = \rho_{10} \otimes \rho_{20}$, with $\rho_{10} = \frac{1}{2}(1 + p_{n_1} I_z^1)$ and $\rho_{20} = \frac{1}{2}(1 + p_{n_2} I_z^2)$. The evolution of the density matrix of spin $\mathbf{n}_1$ is

$$\rho_1(\tau) = \mathtt{Tr}_{\mathbf{n}_2}\{U\rho_0 U^\dagger\} = \frac{1}{2} + I_z^1(p_{n_1} + (p_{n_2} - p_{n_1})\sin^2 b\tau), \tag{C.12}$$

where $U = \exp(-iH_f\tau)$ is the evolution operator and $\mathtt{Tr}_{\mathbf{n}_2}$ traces out the subsystem of spin $\mathbf{n}_2$. Therefore, the polarization of spin $\mathbf{n}_1$ can be written as

$$p_{n_1}(\tau) = p_{n_1} + (p_{n_2} - p_{n_1})\sin^2 b\tau. \tag{C.13}$$

We observe that when the two nuclei are polarized equally ($p_{n_1} = p_{n_2}$) and $p_{n_1} \neq 0$, there is no flip-flop between them. For example, consider the two nuclei prepared in either $\uparrow\uparrow$ or $\downarrow\downarrow$. In this case, flip-flops are suppressed because of the energy gap ($2\omega_0 \gg b$) between the $\uparrow\uparrow$ and $\downarrow\downarrow$ configurations. On the other hand, when both nuclei are prepared with opposite polarizations ($p_{n_1} = -p_{n_2}$), the spin flip-flops are maximized since the energy gap between $\uparrow\downarrow$ and $\downarrow\uparrow$ is near zero. After a time of $\tau = \pi/2b$, the $\uparrow\downarrow$ part has evolved to $\downarrow\uparrow$ (i.e., the SWAP operation).

Meanwhile, for $m_s = 1$ subspace, the two nuclear spins have very different energy splittings due to the distinct hyperfine couplings (see the discussion after Equation (SC.6)). This would suppress the spin flip-flop terms. As shown in Figure C.3, the flip-flop process between spins $\mathbf{n}_1$ and $\mathbf{n}_2$ are significantly suppressed when the electronic spin is $|m_s = 1\rangle_e$. The residual oscillations are due to the imperfect preparation of the electronic spin (e.g., optical pumping and π pulses) that induces a small probability in $m_s = 0$.

We can use the oscillation amplitudes for both $m_s = 0$ and $m_s = 1$ subspaces to estimate the polarization of the electronic spin after optical pumping. Suppose the

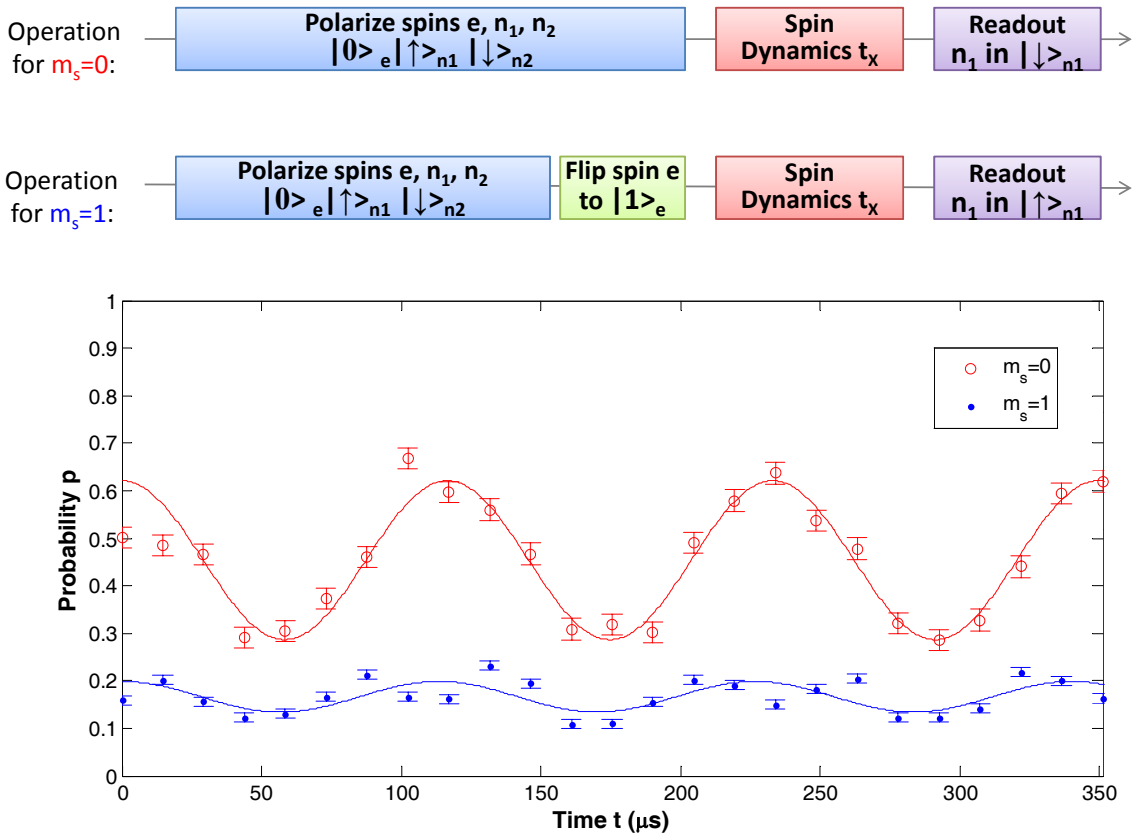

Figure C.3: Dynamics of nuclear spins for $m_s = 0$ and $m_s = 1$ subspaces. The nuclear spins $\mathbf{n}_1$ and $\mathbf{n}_2$ are initialized in $|\uparrow\rangle_{n_1}|\downarrow\rangle_{n_2}$. When the electronic spin is $|m_s = 0\rangle_e$, there is a flip-flop process between the two nuclear spins (red curve). When the electronic spin is $|m_s = 1\rangle_e$, the flip-flop process is strongly suppressed (blue curve).

polarization of the electronic spin is $1-\varepsilon_{pump}$, the ratio of two oscillation amplitudes is approximately $\frac{Am_s=1}{Am_s=0} \approx \frac{\frac{\varepsilon_{pump}}{2}+\varepsilon_{MW}}{1-\varepsilon_{pump}}$, where the total error probability associated with MW π-pulses is $\varepsilon^{MW} = \varepsilon^{MW}_{\text{res}} + \varepsilon^{MW}_{\text{det}} \approx 0.08$. Thus, we estimate $\varepsilon_{pump} \approx 0.16 \pm 0.07$. This estimate of spin polarization is consistent with that found by Harrison et. al. [153] who studied optical spin polarization in ensembles of NV centers at cryogenic temperature using ESR spectroscopy.

C.3 Nuclear Spin Depolarization for Each Readout

The mechanism for depolarization of nuclear spins under optical illumination is induced by stochastic electronic optical transitions, which connect multiple electronic states with different hyperfine interactions to the nuclear spins [74, 39]. The process can described by the master equation that accounts for both the classical stochastic transition of the electronic states and the coherent evolution of the nuclear spins with state-dependent hyperfine interactions. For fast optical excitation/relaxation, the evolution under each of these different hyperfine interactions is suppressed. This increases the depolarization time for the nuclear spin.

Reducing the transverse magnetic field with respective to the NV axis can further increase the depolarization time of the nuclear spin [74, 39]. The theoretical description for the depolarization of the nuclear spin under optical illumination is detailed in [74]. The same theoretical model can also explain the observed double exponential decay in Figure 4.2D, which is associated with the two time scales for dephasing and depolarizing with respective to the motional-averaged quantization axis [74].

Since the power for the laser pulses is almost the same for the experiments presented in Figures 4.2, 4.3 and 4.4, we may use the depolarization curve (Figure 4.2D) to estimate the relative reduction in polarization for various operations. For the first nuclear spin, the relative reduction of polarization ε_{n1} is 0.035 ± 0.015 after each 350 ns green laser pulse. For the second nuclear spin, we estimate the relative reduction of polarization ε_{n2} is about 0.3 ± 0.1 after 5 μs green laser pulse, and about 0.5 ± 0.1

after 20 μs green laser pulse.

Note also that the imperfect optical pumping of the electronic spin can be made very small with sufficiently long optical pulse, but this is not optimal for our repetitive readout scheme, because long optical illumination eventually induces depolarization of the nuclear spins that store useful information. To mitigate the perturbation to the nuclear spins, 350 ns green optical pumping pulses are chosen that result in 75% electronic spin polarization in the state $|0\rangle_e$. This affects all readouts immediately proceeded by an optical readout pulse (i.e., $m = 2, \cdots, M$), which degrades the gain in signal amplitude. These effects are estimated through numerical simulations of the repeated readout scheme in the following sections.

C.4 Deriving Optimized SNR

The rate of optical fluorescence of the NV center depends strongly on the electronic spin state for up to 500 ns after the center is optically probed at wavelengths below the zero-phonon line [111]. We define $\overline{n^0}$ and $\overline{n^1}$ as the average number of photons detected during a 325 ns measurement interval (i.e. readout) for the $|0\rangle_e$ and $|1\rangle_e$ states respectively. For a set of repeated readouts, we obtain the average number of counts $\overline{n_m}(\{p\})$ where the bar indicates the average number of photons over N experimental realizations and the m subscript indexes the repeated readout. The $\{p\}$ represent controllable parameters of the experiment. For example in a Rabi experiment $p = t_p$, the duration of microwave radiation.

We extract the signal amplitudes A_m for the mth measurement interval by fitting each $\overline{n}_m(t_p)$ readout of a Rabi experiment to a cosine curve of the form: $A_m \cos(\Omega_{MW} t_p) +$

B_m. The value A_0 is the amplitude of a Rabi oscillation with full initial spin polarization (Figure 4.1B). The standard error $\overline{\sigma}_m$ of the mth measurement is found to be almost independent of m: $\sigma_m \approx \sigma_0$, with σ_0 being the uncertainty associated with the measurement of A_0. Since the $|A_m|$ values decrease with increasing m (Figure 4.3D), it is optimal to weight each element of the measurement record.

We use the signal-to-noise ratio (SNR) as the figure of merit for the repetitive readout scheme. The signal is defined as the weighted sum of the Rabi oscillation amplitudes obtained from repetitive readout.

$$\text{Signal} = \sum_{m=1}^{M} w_m \left|A_m\right|, \tag{C.14}$$

with weight w_m for the m-th readout. The corresponding noise is

$$\text{Noise} = \sqrt{\sum_{m=1}^{M} w_m^2 \sigma_m^2}, \tag{C.15}$$

where σ_m is the noise for the m-th readout, which can also be obtained experimentally. The signal-to-noise ratio [154] is defined as

$$\frac{\text{Signal}}{\text{Noise}} = \frac{\sum_{m=1}^{M} w_m \left|A_m\right|}{\sqrt{\sum_{m=1}^{M} w_m^2 \sigma_m^2}}. \tag{C.16}$$

According to the Cauchy-Schwartz inequality, we have

$$\sum_{m=1}^{M} \left(w_m \sigma_m\right)^2 \sum_{m=1}^{M} \left(\frac{\left|A_m\right|}{\sigma_m}\right)^2 \geq \left(\sum_{m=1}^{M} w_m \left|A_m\right|\right)^2, \tag{C.17}$$

where equality is satisfied when $w_m = \left|A_m\right| / \sigma_m^2$. Therefore, the optimized SNR is

$$\text{SNR}_{\text{opt}}\left(M\right) = \sqrt{\sum_{m=1}^{M} \left|\frac{A_m}{\sigma_m}\right|^2}. \tag{C.18}$$

In Figure C.4, we plot the SNR curves for optimal weighting and for equal weighting of each measurement for the single proximal nuclear spin repeated readout. We

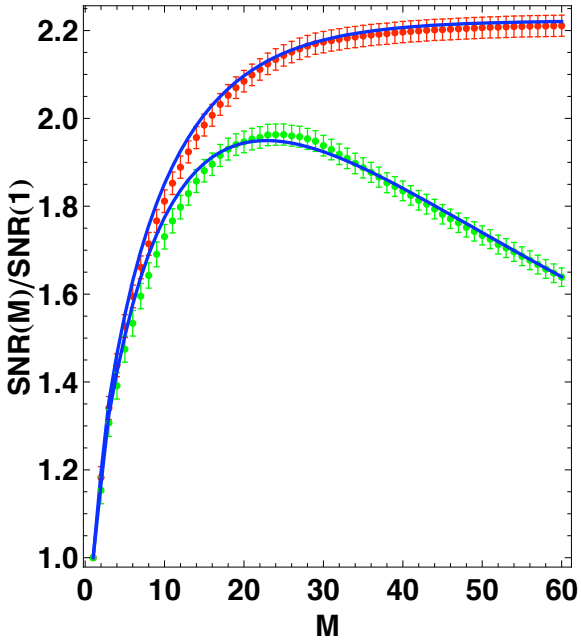

Figure C.4: Signal-to-Noise ratio for repetitive readout. The green data points correspond to the SNR where $w_m = 1$ for all measurements of the A_m amplitudes and σ_m uncertainties. The red data are for the optimized SNR values where $w_m = |A_m|/\sigma_m^2$ and reach the best SNR improvement of 220%. The blue curves are the theoretical fits to our model for measurement of the NV center electronic spin and fit well to the data. Note that the model is identical for both cases.

see that for the equal weighting case, after $M \approx 20$ the SNR begins to degrade. This is because of the reduction of the signal amplitude A_m for increasing m due to nuclear spin depolarization, while the noise level σ_m remains almost constant. The weighting factors w_m allow for updating the measurement records to most efficiently use the information with respect to the noise.

C.5 Simulation for the Repetitive Readout

We have performed a numerical simulation for both repetitive readout schemes. We use the transition matrix description to keep track of the state evolution. With reasonable choice of imperfection parameters, we are able to obtain A_m and $\mathrm{SNR}_{\mathrm{opt}}\,(M)$ consistent with the experiment.

Transition matrices

We model $8 = 2^3$ levels associated with the electronic spin and two nuclear spins in the simulation. Because the quantum coherence does not change the outcome of the repetitive readout, it is sufficient to track the probability distribution over these 8 levels. We use the array $\vec{q} = (q_{0\downarrow\downarrow}, q_{0\downarrow\uparrow}, q_{0\uparrow\downarrow}, q_{0\uparrow\uparrow}, q_{1\downarrow\downarrow}, q_{1\downarrow\uparrow}, q_{1\uparrow\downarrow}, q_{1\uparrow\uparrow})^T$ to represent the probability distribution. We consider the transition matrices for various operations characterized by imperfection parameters. For example, if initial state distribution is $\vec{q}_0$ and transition matrix is $\mathcal{T}$, the final state distribution is $\mathcal{T}\vec{q}_0$.

We now list the transition matrices for the operations that are used for spin initialization and repetitive readout.

1) Transition matrix for MW1 π-pulse is

$$\mathcal{T}_{\mathrm{MW1}} = W_{pi} \otimes I_{\downarrow} \otimes \mathbb{1}_2 + W_{id} \otimes I_{\uparrow} \otimes \mathbb{1}_2, \tag{C.19}$$

where

$$W_{pi} = \begin{pmatrix} \varepsilon_{\mathrm{res}}^{MW} & 1-\varepsilon_{\mathrm{res}}^{MW} \\ 1-\varepsilon_{\mathrm{res}}^{MW} & \varepsilon_{\mathrm{res}}^{MW} \end{pmatrix} \qquad W_{id} = \begin{pmatrix} 1-\varepsilon_{\mathrm{det}}^{MW} & \varepsilon_{\mathrm{det}}^{MW} \\ \varepsilon_{\mathrm{det}}^{MW} & 1-\varepsilon_{\mathrm{det}}^{MW} \end{pmatrix}$$

$$I_{\downarrow} = \begin{pmatrix} 1 & 0 \\ 0 & 0 \end{pmatrix} \qquad I_{\uparrow} = \begin{pmatrix} 0 & 0 \\ 0 & 1 \end{pmatrix} \qquad \mathbb{1}_2 = \begin{pmatrix} 1 & 0 \\ 0 & 1 \end{pmatrix}$$

with $\varepsilon_{\text{res}}^{MW} = 0.07$ for the resonant transition and $\varepsilon_{\text{det}}^{MW} = 0.01$ for the Δ-detuned transition (see Section C.1). Similarly the transition matrix for MW2 π-pulse is

$$\mathcal{T}_{\text{MW2}} = W_{pi} \otimes I_{\uparrow} \otimes \mathbb{1}_2 + W_{id} \otimes I_{\downarrow} \otimes \mathbb{1}_2. \tag{C.20}$$

2) The transition matrices for nuclear spin depolarization under optical illumination are

$$\mathcal{T}_{n1} = \mathbb{1}_2 \otimes \begin{pmatrix} 1 - \frac{\varepsilon_{n1}}{2} & \frac{\varepsilon_{n1}}{2} \\ \frac{\varepsilon_{n1}}{2} & 1 - \frac{\varepsilon_{n1}}{2} \end{pmatrix} \otimes \mathbb{1}_2 \tag{C.21}$$

for $\mathbf{n}_1$, and

$$\mathcal{T}_{n2} = \mathbb{1}_2 \otimes \mathbb{1}_2 \otimes \begin{pmatrix} 1 - \frac{\varepsilon_{n1}}{2} & \frac{\varepsilon_{n1}}{2} \\ \frac{\varepsilon_{n1}}{2} & 1 - \frac{\varepsilon_{n1}}{2} \end{pmatrix} \tag{C.22}$$

for $\mathbf{n}_2$. The depolarization factors are $\varepsilon_{n1} = 0.05$ for $\mathbf{n}_1$ after $t_{green} = 350$ ns green laser pulse, and $\varepsilon_{n2} = 0.42$ and 0.63 for the second nuclear spin after 5 and 20 μs green laser pulses (see Section C.3). During the M-step repetitive readout, the flip-flop evolution between $\mathbf{n}_1$ and $\mathbf{n}_2$ during the short 1.5 μs interval between sequential readouts may occur with probability about 5%, which is also effectively included into ε_{n2}.

3) The transition matrix for optical pumping of the electronic spin is

$$\mathcal{T}_{\text{Pump}} = \begin{pmatrix} 1 - \varepsilon_{pump,0} & 1 - \varepsilon_{pump,1} \\ \varepsilon_{pump,0} & \varepsilon_{pump,1} \end{pmatrix} \otimes \mathbb{1}_2 \otimes \mathbb{1}_2, \tag{C.23}$$

where $\varepsilon_{pump,0}$ and $\varepsilon_{pump,1}$ are the error probability for imperfect pumping. The characteristic time for optical pumping of the electronic spin is $\tau_{pump} = 235$ ns, so the 350

ns green laser pulse has $\varepsilon_{pump,1} = 0.25$. In addition, we also assume that there will be $\varepsilon_{pump,0} = 2\%$ of the population from $m = 0$ to $m = 1$ state.

4) The transition matrix for the RF π-pulse is

$$\mathcal{T}_{\mathrm{RF}} =_2 \otimes \begin{pmatrix} 1-\varepsilon_{RF} & \varepsilon_{RF} \\ \varepsilon_{RF} & 1-\varepsilon_{RF} \end{pmatrix} \otimes \mathbb{1}_2 \tag{C.24}$$

where $\varepsilon_{RF} < 1\%$ based on our calibration, so we assume perfect RF π-pulse (i.e., $\varepsilon_{RF} = 0$) for simplicity. Similarly we also assume negligible error for the SWAP gate on $\mathbf{n}_1$ and $\mathbf{n}_2$.

Simulation with transition matrices

Using the above transition matrices, we can obtain the evolution in probability distribution for a given pulse sequence. For example, the distribution after k-step repeated pumping of $\mathbf{n}_1$ is

$$\vec{q}_k = \left(\mathcal{T}_{\mathrm{Pump}}\mathcal{T}_{\mathrm{RF}}\mathcal{T}_{\mathrm{MW2}}\right)^k \ \vec{q}_0, \tag{C.25}$$

where $\vec{q}_0$ is the initial distribution. With these parameters, we first simulate and obtain the amplitude of nuclear Rabi oscillation, with amplitude 0.61, consistent with experimental observation of 0.60 ± 0.05.

For the pulse sequence provided in Figure 4.3B, the state for the first readout is

$$\vec{q}^{(\delta)}_{\mathrm{meas},1} = \mathcal{T}_{\mathrm{RF}} \left(\mathcal{T}_{\mathrm{MW1}}\right)^\delta \ \vec{q}_{k=6}, \tag{C.26}$$

where $\delta = 0$ for trivial MW1 pulse with duration $t = 0$, and $\delta = 1$ for MW1 π-pulse with duration $t = \pi/\Omega_{MW}$. The population difference in $|0\rangle_e$ between $\vec{q}^{(0)}_{\mathrm{meas},1}$ and

$\vec{q}^{(1)}_{\text{meas},1}$ gives the normalized amplitude

$$|A_1| = \left|\text{Prob}\left[\vec{q}^{(0)}_{\text{meas},1}\right] - \text{Prob}\left[\vec{q}^{(1)}_{\text{meas},1}\right]\right|, \tag{C.27}$$

where

$$\text{Prob}\left[\vec{q}\right] = q_{0\downarrow\downarrow} + q_{0\downarrow\uparrow} + q_{0\uparrow\downarrow} + q_{0\uparrow\uparrow} \tag{C.28}$$

is the probability in the $|0\rangle_e$ state for distribution $\vec{q}$.

The state for the following readout is

$$\vec{q}^{(\delta)}_{\text{meas},m} = \begin{cases} \left(\mathcal{T}_{\text{Pump}}\mathcal{T}_{\text{MW2}}\right)\vec{q}^{(\delta)}_{\text{meas},m-1} & \text{for even } m \\ \left(\mathcal{T}_{\text{Pump}}\mathcal{T}_{\text{MW1}}\right)\vec{q}^{(\delta)}_{\text{meas},m-1} & \text{for odd } m \end{cases}, \tag{C.29}$$

with $m = 2, 3, \cdots, M$. Finally, the normalized amplitude for the m-th readout is

$$|A_m| = \left|\text{Prob}\left[\vec{q}^{(0)}_{\text{meas},m}\right] - \text{Prob}\left[\vec{q}^{(1)}_{\text{meas},m}\right]\right|. \tag{C.30}$$

And

$$\text{SNR}_{\text{opt}}\left(M\right) = \sqrt{\sum_{m=1}^{M}|A_m|^2}. \tag{C.31}$$

The simulation of A_m and $\text{SNR}_{\text{opt}}\left(M\right)$ for the repetitive readout scheme assisted with one qubits are shown in Figure 4.3DE. Similarly, we can also simulate A_m and $\text{SNR}_{\text{opt}}\left(M\right)$ measured for the repetitive readout scheme assisted with two qubits are shown in Figure 4.4CD.

Appendix D

Supporting material for Chapter 5

D.1 Irradiation and annealing procedure

The sample used in the experiment described in Chapter 5 was an ultrapure single crystal bulk diamond grown by chemical vapour deposition (CVD) provided by Element Six Lta. (www.e6.com). The centers were created by irradiating 10^9 cm^{-2} nitrogen ions with energy of 6 keV, corresponding to an estimated average implantation depth of 10 nm, as determined by simulations. The irradiating procedure was done at CORE Lta. (California, USA). The sample was then annealed at 800 °C for 2 hours under a pressure no larger than 10^{-6} torr using a sputtering machine at the Center for Nanoscale Science at Harvard University. This procedure leads to a NV concentration of approximately 0.6 NV/μm^2 corresponding to a yield of 4%. To reliably distinguish shallow implanted ions from natural NV centers, a rare isotope ^{15}N was used.

D.2 Confocal and spin-RESOLFT microscopy

NV centers were probed using a custom-built confocal fluorescence microscope. Two 532 nm laser beams provided optical excitation, one a Gaussian shaped beam and the other a doughnut shaped beam. The two beams, which could be independently switched using Acouto-Optic Modulators (AOMs - Crystal Technology and Isomet), were combined on a polarised beam splitter before entering an oil immersion objective (Nikon Plan Fluor 100x 1.3 NA). Fluorescence from the NV centers was collected back through the objective, separated from the excitation path via a custom dichroic with high surface flatness (Chroma Technology). The fluorescence was filtered $(630-750)$ nm and focused onto a single-mode fibre connected to an avalanche photo detector (APD - Perkin Elmer). Imaging was achieved by scanning the diamond sample under the objective, using a digitized 3-axis piezo translation stage (Physical Instrument P-733.3CD). The doughnut shaped mode was created by passing a Gaussian beam through the center of a helical phase ramp (RPC Photonics), which adds a phase from $(0$ to $2\pi)$ conditional on the azimuthal position. To prevent distortion of the doughnut center due to beam focusing by the objective, the beam was circularly polarized by placing a quarter-lambda waveplate immediately before the objective.

D.3 Generation of Doughnut beam

The doughnut shaped mode was created by passing a Gaussian beam through the center of a helical phase ramp (RPC Photonics), which adds a phase from (0 to 2π) conditional on the azimuthal position. The exact expression for the doughnut

intensity can be calculated using Fourier analysis[155],

$$A_D(x,y) = \int dk_x dk_y A_G(k_x,k_y) D(k_x,k_y) \tag{D.1}$$

where $A_G(k_x,k_y)$ is the Fourier transform of the amplitude of the initial Gaussian beam

$$A_G(x,y) = \exp\left(-\frac{r^2}{2W}\right) \tag{D.2}$$

and the doughnut Fourier amplitude is given by

$$D(k_x,k_y) = \exp\left(\arctan\left(k_x/k_y\right)\right). \tag{D.3}$$

Applying Equation (D.1) leads to the following intensity for the doughnut

$$I_G(r) = |A_D(x,y)|^2 = \frac{\pi}{4}\frac{r^2}{2W^2} e^{-\frac{r^2}{2W^2}} \left(I_0\left(\frac{r^2}{4W^2}\right) - I_1\left(\frac{r^2}{4W^2}\right)\right)^2 \tag{D.4}$$

Assuming that the setup has achieved the confocal resolution, $r_c = \frac{\lambda}{2\mathtt{NA}}$ (and therefore $W = \frac{\lambda}{2\mathtt{NA}}\frac{1}{2\sqrt{log2}} \approx 0.6\frac{\lambda}{2\mathtt{NA}}$) we find that for small r the intensity can be written as

$$I_D(r) = \frac{\pi}{2} log(2) \left(\frac{r}{(\lambda/2\mathtt{NA})}\right)^2 \approx 1.0888 \left(\frac{r}{(\lambda/2\mathtt{NA})}\right)^2. \tag{D.5}$$

Finally, the pumping rate can be written as

$$R = R_0 + R\left(\frac{x}{(\lambda/2\mathtt{NA})}\right)^2, \tag{D.6}$$

where R_0 is the pumping rate at the center of the doughnut due to imperfect non-zero intensity I_0 at the center of the doughnut. To prevent distortion of the doughnut center due to beam focusing by the objective, the beam was circularly polarized by placing a quarter-lambda waveplate immediately before the objective.

D.4 Spin imaging resolution

The spin-RESOLFT signal is proportional to $f(x) = n_0(x)I_G(x)$, where n_0 is the population of the $m_s = 0$ state, $I_G = \exp(-\alpha(x/r_C)^2)$ is the intensity profile of the gaussian beam used for readout of the electronic spin, $r_C = \lambda/2\mathtt{NA}$ is the confocal resolution and $\alpha = 4/log(2)$. n_0 depends on the duration of the doughnut beam t_D; it can be evaluated by solving the rate equations of the system given in Figure D.3. In the limit of large lifetime of the spin transition, it is given by $n_0 = \exp(-R_x t_D)$, where $R_x = \epsilon k_x$ is the position-dependent optical depletion rate out of the $m_s = 1$ state (i.e., polarization rate to the $m_s = 0$ state measured after waiting for the non-radiative relaxation from the singlet state to the $m_s = 0$ state), k_x is the intensity profile of the doughnut-shaped beam and ϵ is the branching ratio of the spin changing ($m_s = 1 \rightarrow m_s = 0$) decay relative to the total decay of the excited state. In the unsaturated regime, $R_x = R_0 + \alpha\Gamma(x/r_C)^2$, where $\Gamma = \kappa\epsilon$ is proportional to the optical excitation rate associated with the maximal intensity of the doughnut κ, and $R_0 = \epsilon\kappa_0$ is proportional to the intensity of the doughnut center and the corresponding excitation κ_0. The resolution r is defined by $f(x) = \exp(-\alpha(x/\Delta r)^2)$. Solving for Δr leads to Eq. (1) in Chapter 5. In the case of a perfect doughnut beam the ultimate resolution is determined by the maximum values of $\Gamma = \gamma\epsilon$ and $T_D \sim T_1$. Thus leading to an improvement in resolution relative to the diffraction limit of a confocal microscope of $\sqrt{\epsilon\gamma T_1}$.

In our experiments, the resolution is limited by a small imperfection of the doughnut-zero intensity. We can find the maximum achievable resolution by using a model that includes a back pumping process which brings the electronic spin from the $m_s = 0$

to the $m_s = 1$ state, and finite spin lifetime. Consider the rate equations of our two level system ($m_s = 0$ and $m_s = 1$),

$$\frac{dn_0}{dt} = R_x n_1 - \gamma_{0\to1}(n_1 - n_0) \tag{D.7}$$

and $n_1 = 1 - n_0$. The solution for this equation is,

$$n_1 = \frac{\gamma_1 + R_x}{2\gamma_{0\to1} + R_x}(1 - e^{-(2\gamma_{0\to1}+R_x)t_D}) \tag{D.8}$$

The resolution δr is defined by the FWHM condition $n_2(R_{r/2}, t) = \frac{1}{2}n_2(R_0, t)$. The maximum improvement in resolution relative to the diffraction limit of a confocal microscope is given by

$$\Delta r/r_C = \sqrt{R_0/\Gamma}\sqrt{1 + 2\gamma_{0\to1}/R_0} \tag{D.9}$$

for an optimal doughnut duration $t_D = \log[(3\gamma_{0\to1} + 2R_0)/(\gamma_{0\to1} + R_0)]/(2\gamma_{0\to1} + R_0)$, where $\gamma_{0\to1}$ is the total rate out of the electronic spin $m_s = 0$. In the limit of long spin lifetime ($\gamma_{0\to1} \ll R_0$), the maximum improvement in resolution is given by $\sqrt{R_0/\Gamma} = \sqrt{\kappa_0/\kappa}$, i.e., the intensity of the doughnut center relative to the maximum doughnut intensity. In our experiments, $\kappa_0/\kappa \approx 1\%$, which is in a good agreement with our 10-fold improvement in resolution relative to the diffraction limit.

To demonstrate the nanoscale resolving power of our spin sensitive far-field optical technique, we imaged NV centers in bulk diamond separated by less than the diffraction limit. Figure D.3a shows a pair of individual NV centers that cannot be resolved using confocal microscopy. However, an optically detected ESR measurement performed in this location displays multiple spectral lines (Figure D.3b), indicating the presence of multiple NV centers with different crystallographic orientations relative to

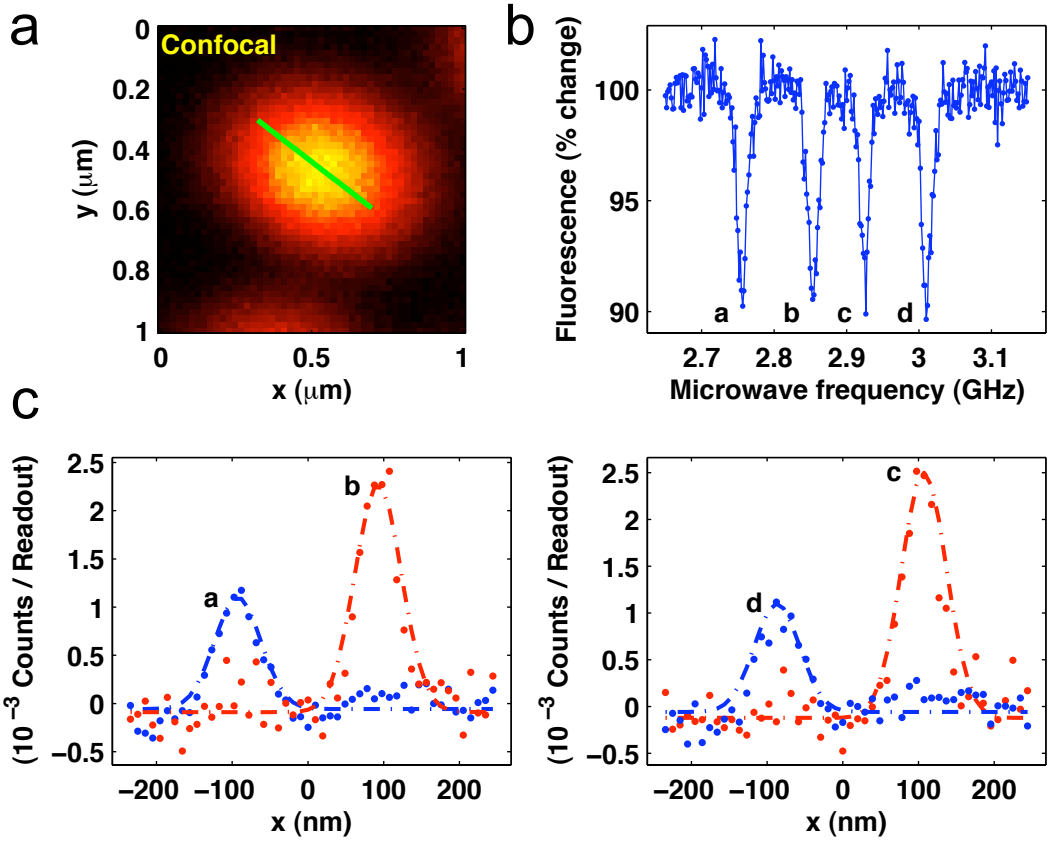

Figure D.1: **Demonstration of sub-diffraction optical imaging of neighbouring NV centers.** A Closely spaced NV centers cannot be resolved using conventional standard imaging. B Optically-detected ESR spectrum with an applied DC magnetic field of 60 G indicates presence of two NV centers with different crystallographic orientations. C Individual NV centers are imaged with sub-diffraction resolution by scanning along the trajectory indicated in A. Each 1D image is obtained by selectively driving corresponding ESR resonance (A-D) with resonant microwave pulse followed by application of doughnut beam and optical readout. Each ESR spectral signature is thereby uniquely associated with its spatial location. Resonances a,c correspond to $|0\rangle \rightarrow |\pm 1\rangle$ transitions of one NV center, while resonances b,d are corresponding transitions for a second NV center.

the applied static magnetic field. Using our sub-diffraction spin detection technique and scanning the microwave frequency, we associated each ESR spectral line with the corresponding location of an individual NV center with sub-diffraction limited

resolution (Figure D.3c). In particular, sub-diffraction spin imaging scans along the trajectory indicated in Figure D.3a, taken for each ESR transition frequency, reveal that two NV centers are responsible for the observed ESR spectrum: each NV center has two spectral ESR lines corresponding to the $|0\rangle \rightarrow |+1\rangle$ and $|0\rangle \rightarrow |-1\rangle$ transitions.

D.5 Measurements of local magnetic field environment with sub-diffraction resolution

As described in Chapter 5, individual NV centers can be resolved, independently manipulated and read-out using our technique. Here we individually measure the response of two NV centers to their local magnetic environment using Rabi and spin-echo techniques. By placing the center of the doughnut over one NV center, the other NV center is polarized and only contributes a constant background to the fluorescence signal. Figure D.2 shows the raw data for Rabi measurements of the two NV centers in Figure 5.3 when the doughnut zero is placed over Center 1 (upper-left panel) and Center 2 (bottom-left panel). When the two curves are added together (green line, right panel), the confocal measurement (taken at the position of Center 1) is recovered (dotted line in Figure D.2).

The observed modulations of the Rabi oscillations shown in Figure 5.3c (and Figure D.2) reveal the different magnetic fields experienced by each NV center. These modulations are caused by hyperfine induced splitting in the NV center's electronic transition ($m_s = 0 \rightarrow 1$) associated with the ^{15}N nuclear spin ($I = \frac{1}{2}$). A simple model

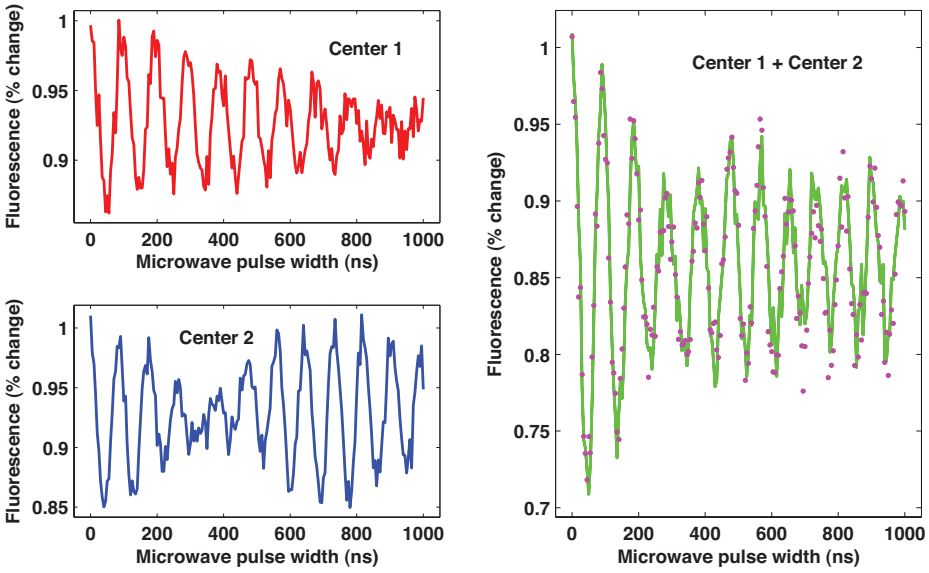

Figure D.2: **Realization of spin-RESOLFT Rabi measurements.** Rabi oscillations for each NV center were measured by centering the doughnut on one of the NV centers. The addition of the two Rabi oscillation data curves (green line, right panel) corresponds to the confocal measurement of both NV centers as expected (pink dots, right panel).

for the probability of finding the electronic spin in the $m_s = 0$ state, P_0, assumes that on average the ^{15}N nuclear spin is half of the time in its spin down state and the other half of the time in its spin up state. Thus, P_0 is just the average of the dynamics of two two-level systems with different splittings. For a two-level system with states $|0\rangle$ and $|1\rangle$, Rabi frequency Ω and detuning δ, the probability to find the system in state $|1\rangle$ (starting from state $|0\rangle$) is given by $(\frac{\Omega}{\Omega_e})^2 \sin^2 \Omega_e \tau$, where $\Omega_e^2 = \Omega^2 + \delta^2$. Therefore, P_0 in our case is given by

$$P_0 = \frac{1}{2}\left(2 - \left(\frac{\Omega}{\Omega_1}\right)^2 \sin^2(\Omega_1 \tau/2) - \left(\frac{\Omega}{\Omega_2}\right)^2 \sin^2(\Omega_2 \tau/2)\right) \tag{D.10}$$

where $\Omega_1^2 = \Omega^2 + \delta_1^2$ and $\Omega_2^2 = \Omega^2 + \delta_2^2$. If $\Omega \gg \delta$, the modulation frequency is given by

$\Delta\Omega = \Omega_2 - \Omega_1 \approx (\delta_1 + \delta_2)(\delta_1 - \delta_2)/2\Omega$. Since $\delta_1 + \delta_2 = 2(f_0 - f)$ and $\delta_2 - \delta_1 = A$, the modulation frequency for an NV center is given by $\Delta\Omega = (\nu_0 - \nu)A/\Omega$, where ν_0 is the frequency of the electronic transition $m_s = 0 \rightarrow 1$, ν is the microwave frequency and $A = 3.05$ MHz[87] is the hyperfine splitting induced by the ^{15}N nuclear spin present on each of our NV centers (see section Samples).

Modulations appear when the microwave frequency is detuned from the central transition $\nu_0^i = \Delta + \gamma_e B^i$, where B^i is the local magnetic field along the NV axis of center i, Δ is the zero-field splitting, and γ_e is the gyromagnetic ratio of the electronic spin. In other words, modulations appear when the two hyperfine transitions are driven with different detunings. The difference in the modulation frequencies of each NV center ($\Delta\Omega_2 - \Delta\Omega_1 = 1.3 - 0.5 = 0.8$ MHz) reveals a difference in the static magnetic field experienced by each NV center of about $\Delta B = 1$ G.

Spin echo measurements can reveal even more subtle differences in the local environment between the two NV centers. In our measurements (Figure 5.3d), the dominant contribution comes from interactions between the electronic spin of the NV center and the ^{15}N nuclear spin and ^{13}C nuclear spin bath. The spin echo signal can be written as [53] $p(\tau) = \frac{1+S(\tau)}{2}$, where $S(\tau)$ is the pseudo spin which can be written as the multiplication of all individual nuclear spin contributions. The first collapse and first revival of the NV spin echo signal can thus be approximated by

$$S(\tau) = S_{^{15}N}(\tau)\left(e^{-(\tau/\tau_C)^4} + ce^{-((\tau-\tau_R)/\tau_C)^4}\right), \tag{D.11}$$

where we have phenomenologically grouped the effect of all ^{13}C nuclear spins in the exponential decays, and where τ_C is the collapse rate[53] given by $\tau_C = 13\mu\mathbf{s}\sqrt{\frac{5\mathbf{G}}{B}}$, B is the local magnetic field, τ_R is the revival time, c is the contrast of the first revival.

The pseudo spin for the ^{15}N nuclear spin is given by

$$S_{^{15}N}(\tau) = 1 - \frac{|\Omega_{^{15}N,0} \times \Omega_{^{15}N,1}|^2}{|\Omega_{^{15}N,0}|^2 |\Omega_{^{15}N,1}|^2} \sin(\Omega_{^{15}N,0}\tau/2)^2 \sin(\Omega_{^{15}N,1}\tau/2)^2, \tag{D.12}$$

where $\Omega_{^{15}N,m_s}$ is the Larmor frequency of ^{15}N when the electron is in state m_s. The blue lines in Figure 5.3d are fitted to Equation (D.11). While Center 2 shows good coherence ($c = 0.86$), Center 1 shows no revival of the signal ($c = 0$). The absence of revival for Center 1 can be due to an unfavorable distribution of nearby pairs of ^{13}C nuclear spins that quickly decohere the electronic spin [23], or due to nearby paramagnetic impurities or other defects. The position of the first revival for Center 2, $\tau_R = 13.5$ μs, is set by the Larmor precession of ^{13}C, $\tau_R^{-1} = \omega_{C13} = \gamma_{C13} B$, corresponding to a local magnetic field of B = 69 G. The high frequency oscillations ($\Omega_{^{15}N,1}$) correspond to the hyperfine interaction between the electronic spin and the ^{15}N nuclear spin, $\Omega_{^{15}N,1} \approx A = 3.05$ MHz. Meanwhile the slow frequency component of the dynamics, $\Omega_{^{15}N,0} = 360$ kHz, corresponds to the Larmor frequency of the ^{15}N nuclear spin when the electron is in state $m_s = 0$. We immediately notice that the slow frequency component is too large to be explained by the bare Larmor frequency of ^{15}N at 69 G, $\gamma_{N15} B = 30$ kHz. This slow frequency component $\Omega_{^{15}N,0}$ is enhanced by virtual transitions between the NV electronic spin and the ^{15}N nuclear spin. This enhancement is of the form (see Appendix A.4),

$$\Delta g = -(3|m_s| - 2)\frac{g_n \gamma_e}{\Delta \gamma_n} \begin{pmatrix} A_{xx} & A_{xy} & A_{xz} \\ A_{yx} & A_{yy} & A_{yz} \\ 0 & 0 & 0 \end{pmatrix}. \tag{D.13}$$

In the case of ^{15}N, the hyperfine interaction is isotropic[87] and the enhancement is given by $\Delta g^0 \approx 7.8$ (corresponding to a gyromagnetic increment factor of $2(\gamma_2/\gamma_n)A/\Delta \approx$

14). Therefore, $\Omega_{^{15}N,0} \approx 14\gamma_n B_\perp$ corresponding to a perpendicular field to the NV axis of $B_\perp = 60$ G. This value is in agreement with the component of the magnetic field parallel to the NV axis that leads to the observed splitting in the ESR spectrum (Figure 5.3a), $B_{||} = 36$ G ($B = \sqrt{36^2 + 59^2} \approx 69$ G).

D.6 Inhibition of Electron-Spin Rabi Oscillations via Quantum Zeno-like Effect

In Chapter 5 (Figure 5.4a), we demonstrate that a green laser beam can inhibit coherent electron-spin transitions of a single, isolated NV center driven by a resonant microwave pulse. In Figure 5.4b we exploit this property to perform spatially-selective coherent electron-spin Rabi oscillations on one of two closely spaced, 150 nm, NV centers, using a doughnut shaped laser beam.

In Figure 5.4a we investigate this suppression mechanism by applying the pulse sequences S1 and S2. Our analysis requires knowledge of the populations ($\rho_{0,0}$, $\rho_{1,1}$, $\rho_{1A_1,1A_1}$) of the $m_s = 0$, $m_s = \pm 1$ and $^1A_1$ manifolds right after state preparation. To determine these quantities we record the fluorescence,

$$f(\tau_d) = c_{0,0}\rho_{0,0}(\tau_d) + c_{1,1}\rho_{1,1}(\tau_d) + c_{1A_1,1A_1}\rho_{1A_1,1A_1}(\tau_d), \tag{D.14}$$

of a single NV center for two different times $\tau_d \ll T_{1A_1}$ and $\tau_d \gg T_{1A_1}$, where τ_d is the time defined in S1 and S2 of Figure 5.4a, $T_{1A_1} = 300$ ns is the lifetime of the singlet, and $c_{i,i}$ are the fluorescence rates for the corresponding states, which can be determined experimentally. Since the singlet $^1A_1$ nearly always decays non-radiatively into the $m_s = 0$ state (and hence $c_{1A_1,1A_1} = 0$)[111] we can extract the populations

$\rho_{i,i}$, which are shown in Figure 5.4a, from measuring the fluorescence at $\tau_d \ll T_{1A_1}$ and $\tau_d \gg T_{1A_1}$ and using the relation $\rho_{0,0} + \rho_{1,1} + \rho_{1A_1,1A_1} = 1$. This allows us to find the system of equations

$$\begin{aligned} 1 &= \rho_{0,0} + \rho_{1A_1,1A_1} + \rho_{1,1} \\ f(\tau_d \ll 50ns) &= c_{0,0}\rho_{0,0} + c_{1,1}\rho_{1,1} \\ f(\tau_d \gg 50ns) &= c_{0,0}(\rho_{0,0} + \rho_{1A_1,1A_1}) + c_{1,1}\rho_{1,1}, \end{aligned} \tag{D.15}$$

which defines the population $\rho_{i,i}$ for $\tau_d \ll T_{1A_1}$.

Figure 5.4b demonstrates that a green doughnut-shaped laser beam inhibits electron-spin Rabi oscillations on one of two closely spaced NV centers (Center 2, sitting outside the central doughnut null), while allowing Rabi oscillations to proceed on Center 1, which sits in the zero of the doughnut. The two NV centers have a spatial separation of about 150 nm. To verify that Center 1 can undergo coherent Rabi oscillations while Center 2 is kept in the $m_s = 0$ state, two experiments (pulse sequences S3 and S4 in Figure 5.4b) were performed and subtracted from each other. If Center 2 remains in the $m_s = 0$ state, a constant signal is expected for the difference. In this subtraction procedure we accounted for contrast reduction in the spin-RESOLFT readout of Center 1 by multiplying the results of experiment S4 by 1.3. (This weighting factor is determined from a separate experiment, in which both centers were prepared in the state $m_s = 1$ and imaged with spin-RESOLFT). The signals were normalized relative to the ideal (unperturbed) Rabi oscillation signal for Center 1.

In this section, we describe in detail the optical inhibition of electron spin Rabi oscillations using a doughnut beam (Figure 5.4b in Chapter 5). The basic idea can be explained by considering a simple two-level system (with states $|0\rangle$ and $|1\rangle$), which

undergoes Rabi oscillations (with Rabi frequency Ω) and which is subject to an effective dephasing (with dephasing rate γ_p). The system dynamics is then governed by the Hamiltonian $H = -\frac{\Omega}{2}\sigma_x$ (where $\vec{\sigma}$ are Pauli matrices) combined with the decay of the off-diagonal matrix elements of the density matrix ρ with rate γ_p. Formally, this is described by the following master equation:

$$\frac{d\rho}{dt} = i\left[\frac{\Omega}{2}\sigma_x, \rho\right] - \frac{\gamma_p}{4}\left[\sigma_z, [\sigma_z, \rho]\right]. \tag{D.16}$$

Suppose the system starts in the $|0\rangle$ state, i.e., $P_0(t=0) = 1$. We analytically solve the master equation and obtain the probability of being in the $|0\rangle$ state as a function of time:

$$P_0(t) = \frac{1}{2}\left(1 + \frac{\Gamma_+ e^{-\Gamma_- t} - \Gamma_- e^{-\Gamma_+ t}}{\Gamma_+ - \Gamma_-}\right), \tag{D.17}$$

where $\Gamma_\pm = \frac{1}{2}\left(\gamma_p \pm \sqrt{\gamma_p^2 - 4\Omega^2}\right)$. We may also use the approximate form:

$$P_0(t) \approx \begin{cases} \frac{1}{2}\left(1 + \cos(\Omega t)\, e^{-\gamma_p t/2}\right) & \texttt{for } \Omega \gg \gamma_p \\ \frac{1}{2}\left(1 + \exp\left(-\frac{\Omega^2}{\gamma_p} t\right)\right) & \texttt{for } \Omega \ll \gamma_p \end{cases}. \tag{D.18}$$

For $\Omega \gg \gamma_p$, the two-level system undergoes Rabi oscillations with an amplitude decay rate $\gamma_p/2$. This scenario approximately describes the evolution of Center 1 [blue curve in Figure 5.4b in Chapter 5]: there the amplitude decay comes from a combination of T_2^* decay and of the dephasing due to the imperfect zero of the dougnut. On the other hand, for $\Omega \ll \gamma_p$, the oscillation dynamics is inhibited, and the system remains in the initial state $|0\rangle$ with a slow spin-relaxation rate Ω^2/γ_p, which is inversely proportional to γ_p. This scenario, which we refer to as a quantum Zeno-like effect [48], approximately describes the evolution of Center 2 [green curve in Figure 5.4b in Chapter 5]. In particular, the scheme succeeds if the spin-relaxation

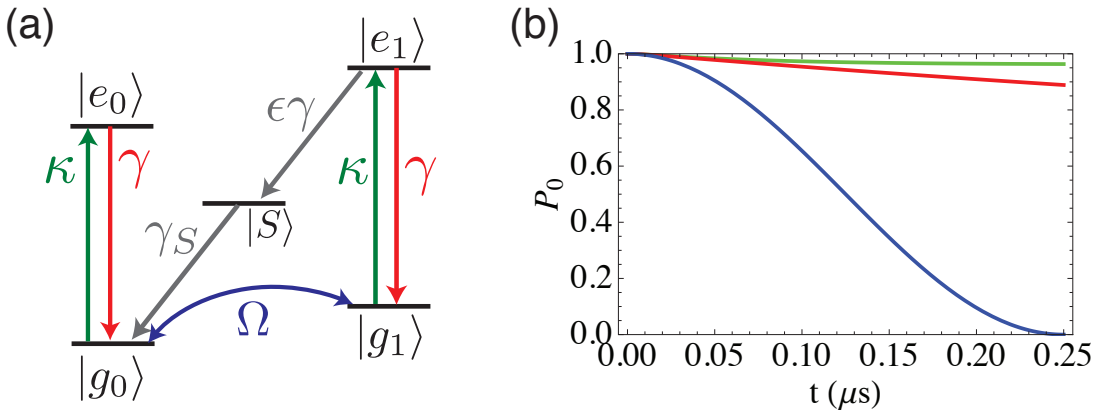

Figure D.3: **title.** (a) 5-level system used to model inhibition of electron-spin Rabi oscillations. $\gamma \approx 1/(13\text{ ns}) = (2\pi)12.2$ MHz, $\gamma_S \approx 1/(300\text{ ns})$, and $\Omega = (2\pi)2$ MHz. (b) Calculated inhibition of electron-spin Rabi oscillations: the blue curve has $\kappa = 0$ and shows an uninhibited Rabi π-pulse [analogous to Center 1 evolution shown as the blue curve in Figure 5.4b of Chapter 5]; the green (red) curve has $\kappa = \gamma$ and $\epsilon = 0.3$ ($\epsilon = 0$) and demonstrates the inhibition of the Rabi oscillations. The green curve is analogous to Center 2 evolution shown as the green curve in Figure 5.4b of Chapter 5. The fact that the red curve stays close to 1 confirms that the quantum Zeno-like effect due to dephasing (and not the optical pumping from $|g_1\rangle$ to $|g_0\rangle$) plays the dominant role in suppressing Rabi oscillations of Center 2. The value (here ≈ 0.9) of the red curve at the final time π/Ω can be used as a rough estimate of preservation of nuclear spin coherence on Center 2 in future experiments.

rate in Center 2 over the course of a π-pulse on Center 1 is much less than unity: $1-P_0(t) \approx (1/2)(\Omega^2/\gamma_p)*(\pi/\Omega) = \pi\Omega/(2\gamma_p) \ll 1$. In other words, for times $t \ll \gamma_p/\Omega^2$ the center is "frozen" in the ground state.

In reality, the experimental situation is more complicated than this simple two-level model. Specifically, we must account for processes in which the spin is first flipped to state $|1\rangle$ and subsequently repolarized to state $|0\rangle$. We therefore model the experiment by considering the five-level system shown in Figure D.3(a). The five states are the ground states $|g_0\rangle$ with $m_s = 0$ and $|g_1\rangle$ with $m_s = 1$, the excited states $|e_0\rangle$ with $m_s = 0$ and $|e_1\rangle$ with $m_s = 1$, as well as the singlet $|S\rangle$. In addition to

the coherent evolution with Rabi frequency Ω, the system is subject to incoherent excitation (caused by the green laser) from the ground to the excited states with rate κ. Moreover, the excited states decay down to the triplet with rate $\gamma \approx 1/(13\text{ ns}) = (2\pi)12.2$ MHz [111]. At the same time, the state $|e_1\rangle$ decays down to the singlet with rate $\epsilon\gamma$, where we take $\epsilon = 0.3$, while the singlet decays to $|g_0\rangle$ with rate $\gamma_S \approx 1/(300\text{ ns})$. After extracting $\Omega = (2\pi)2$ MHz from the uninhibited Rabi oscillations of Center 1 [Figure 5.4b in Chapter 5] and $\kappa \approx \gamma$ (on Center 2) from the fluorescence saturation curve (not shown), we know all the parameters and can compute the resulting evolution of Center 2 over time π/Ω, which is sufficient for a π pulse on the uninhibited Center 1. We begin with Center 2 in the state $|g_0\rangle$, keep the microwave and the green light on for time t, then allow the population to relax to $|g_0\rangle$ and $|g_1\rangle$, and plot in green in Figure D.3(b) the resulting population P_0 of $|g_0\rangle$ for Center 2 as a function of t. In agreement with the green curve in Figure 5.4b of Chapter 5, we see that the population stays within a few percent of the initial population of unity, while Center 1 (with $\kappa \approx 0$) does a Rabi π pulse (blue curve). The reason why the blue curve in Figure 5.4b of Chapter 5 does not show a perfect π-pulse is because the doughnut zero is imperfect and because T_2^* is finite.

To confirm that the observed inhibition indeed comes from Zeno-like effects and not from re-pumping of the electron spin from $|g_1\rangle$ to $|g_0\rangle$ via the singlet, we plot in red in Figure D.3(b) the equivalent of the green curve except with $\epsilon = 0$, i.e. we turn off the $|g_1\rangle \rightarrow |g_0\rangle$ pumping process. We observe that the population still stays mostly in $|g_0\rangle$, confirming that it is indeed Zeno-like dynamics that is largely responsible for the inhibition. In fact, for our parameters ($\kappa \gg \Omega$), the red curve has a simple

analytical form

$$P_0(t) = \frac{1}{2}\left(1 + e^{-\frac{\gamma}{\kappa+\gamma}\frac{\Omega^2}{\kappa}t}\right). \tag{D.19}$$

Since both $|g_0\rangle$ and $|g_1\rangle$ are excited with rate κ, the coherence between these two levels decays with rate κ, so κ plays the role of the dephasing rate γ_p from our two-level model above. The prefactor $\gamma/(\kappa+\gamma)$ in front of Ω^2/κ is the population that is in the ground state triplet, while the remainder is in the excited state and is unaffected by Ω since the corresponding transition in the excited state is highly off-resonant (and was, thus, not included in the model). Under this approximation, the transition probability for Center 2 over time π/Ω is $1 - P_0(t) \approx [\gamma/(\kappa+\gamma)][\pi\Omega/(2\kappa)]$, which for our parameters is ≈ 0.1, which is much smaller than unity, as desired. This value can be further reduced by going to larger green laser powers or smaller Rabi frequencies.

One eventual goal of this demonstrated inhibition is to allow quantum information stored in a nuclear spin degree of freedom (coming from the nitrogen or a nearby carbon-13) to be controllably manipulated in each NV center. Provided that the electron state of the illuminated NV center (Center 2) is kept in $|m_s = 0\rangle$, the state of the corresponding nuclear spin would be preserved [74], while the nuclear spin associated with Center 1 can be prepared, coherently manipulated, or detected with subwavelength resolution. The performance of this technique can be directly evaluated from our measurements. Specifically, the error induced on the nuclear spin associated with illuminated Center 2 is proportional to $1 - P_0 \approx 0.1 \ll 1$. This small error indicates that the state of the nuclear spin associated with Center 2 can be well preserved while we manipulate Center 1.

Appendix E

Supporting material for Chapter 6

E.1 Dangling bond representation and character table

In this appendix we show in detail how to find the electronic representation for the case of the NV center. The NV center contains a vacancy that results in broken bonds in the system. In the tight binding picture, this means that three C atoms and one N-atom do not have enough immediate neighbor atoms to form a covalent bond for *each* of their valence electrons. These unpaired electrons are called 'dangling bonds'. In the case of the NV center, we consider a simple model consisting of four sp^3 dangling bonds, where three of them are centered on each of the three carbon atoms around the vacancy and the fourth dangling bond is associated with the nitrogen atom. The point group symmetry is C_{3v} and its elements are the identity, rotations around the z (NV-axis) by $\pm 2\pi/3$ and three vertical reflection planes where each contains one of

the carbons and the nitrogen.

As discussed in Section 6.2, it is possible to construct the representation of the dangling bonds for the point group they belong to. Consider Figure E.1 where the $\hat{z}$ axis is pointing out of the paper. The dangling bonds $\{\sigma_1, \sigma_2, \sigma_3, \sigma_N\}$ transform into one another under the operations of the C_{3v} group. In this representation, each operation can be written as a 4x4 matrix, as shown in Figure E.1. As representations depend on the particular choice of basis, it is customary to use the sum of the diagonal of each matrix (characters). Note that the character for matrices belonging to the same class is the same, so in short the character representation for the dangling bonds is $\Gamma_\sigma = \{411\}$. This representation is clearly reducible, as it can be decomposed by the irreducible representation of the C_{3v} group given in Table E.1[156].

Table E.1: Character and bases table for the double C_{3v} group. Examples of functions that transform under a particular representation are $\{z, x^2+y^2, z^2\}$ which transform as the IR A_1, R_z transforming as A_2 and the pair of functions $\{(x,y),(R_x,R_y),(xy,x^2-y^2),(yz,xz)\}$ for the E IR.

C_{3v}	E	C_3	$3\sigma_v$	$\bar{E}$	$2\bar{C}_3$	$3\bar{\sigma}_v$
A_1	1	1	1	1	1	1
A_2	1	1	-1	1	1	1
E	2	-1	0	2	-1	0
$E_{1/2}$	2	1	0	-2	-1	0
${}^1E_{3/2}$	1	-1	i	-1	1	$-i$
${}^2E_{3/2}$	1	-1	$-i$	-1	1	i

Application of Equation (6.1) gives the following combination of σ's: $\{a_C = (\sigma_1+\sigma_2+\sigma_3)/3,\ e_x = (2\sigma_1-\sigma_2-\sigma_3)/\sqrt{6},\ e_y = (\sigma_2-\sigma_3)\sqrt{2},\ a_N = \sigma_N\}$, where a_C and a_N transform as the totally symmetric irreducible representation A_1, and e_x and e_y transform as functions of the IR E. Note that the e states transform as vectors

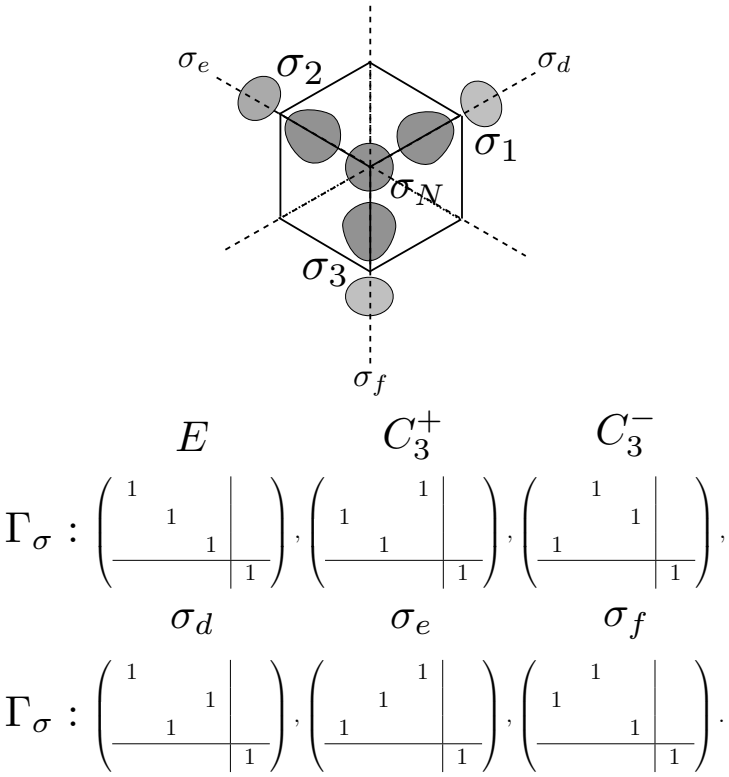

Figure E.1: **Schematic of the NV defect and dangling bond representation.** (Top) Schematic of the dangling bond orbitals used to represent the NV defect. The symmetry axis or NV axis is pointing out of the plane of the page. The dashed lines represent the three vertical reflections planes of the C_{3v} group. (Bottom) Matrix representation of the dangling bonds.

in the plane perpendicular to the NV axis.

Next, we model the electron-ion interaction to find out the ordering of these states. This interaction can be written in the basis of the dangling bonds σ_i as,

$$V = v_n|\sigma_N\rangle\langle\sigma_N| + \sum_i v_i|\sigma_i\rangle\langle\sigma_i| + h_n|\sigma_i\rangle\langle\sigma_N| + \sum_{i>j}|\sigma_i\rangle\langle\sigma_j|h_c \tag{E.1}$$

where $v_i < 0$ is the Coulomb interaction of orbital σ_i at site i and h_c is the expectation value of the interaction between orbitals σ_i and σ_{i+1} at site $i = \{1, 2, 3\}$. This interaction, which transforms as the totally IR A_1, not only sets the order of

the orbitals but also mixes orbitals a_N and a_C. This is as expected since both wave functions transform as the totally symmetric representation A_1 as well as the interaction between them so that the representation for the matrix element also transform as $\Gamma_{\langle\rangle} = \Gamma_a \otimes \Gamma_{\sigma_N} \otimes \Gamma_{int} = A_1 \supset A_1$. The following concept is of major importance: whenever a matrix element contains the totally symmetric representation, its expectation value *might* be different from zero[130]. This interaction leads to the new basis[18] $\{a_1(1) = \alpha a_c + \beta a_n,\, a_1(2) = \alpha a_n + \beta a_c,\, e_x = (2\sigma_1 - \sigma_2 - \sigma_3)/\sqrt{6},\, e_y = (\sigma_2 - \sigma_3)\sqrt{2}\}$, with energies $\{E_{a_1(1),a_1(2)} = \frac{1}{2}(v_c + 2h_c + v_n) \pm \frac{1}{2}\Delta,\, v_c - h_c,\, v_c - h_c\}$, respectively, where $\Delta = \sqrt{(v_c + 2h_c - v_n)^2 + 12h_n^2}$, $\alpha^2 = 1 - \beta^2 = 3h_n^2/\Delta E_{a_1(1)}$. We see that the most symmetric state is lowest in energy, which is usually the case for attractive interactions.

E.2 Ordering of singlet states

Here we show that two states belonging to the same irreducible representation should have the same expectation value for their Coulomb interaction. We first note that the expectation value of an operator is a classical number and it should not depend on the particular coordinate system in use. In particular, this expectation value should be invariant under any operation of the C_{3v} group of the NV center. The Coulomb interaction is totally symmetric and therefore not affected by any rotation, and the wavefunctions $\{e_x, e_y\}$ transform as the irreducible representation E. Therefore, we can get more information about these expectation values by projecting

them on the totally symmetric irreducible representation A_1,

$$(ab, V, cd) = \frac{1}{h}\sum_{R=1}^{h} \chi_e \left(P_R(a)P_R(b), V, P_R(c)P_R(d)\right). \tag{E.2}$$

We find as expected that

$$({}^1E_1, V, {}^1E_1) = \frac{1}{2}({}^1E_1, V, {}^1E_1) + \frac{1}{2}({}^1E_2, V, {}^1E_2), \tag{E.3}$$

which means that the states $({}^1E_1, V, {}^1E_1)$ and $({}^1E_2, V, {}^1E_2)$ have the same energy, as required by symmetry.

E.3 Spin-spin interaction

In order to analyze the effect of spin-spin interactions (Equation 6.6) from the perspective of group theory, we first rewrite this interaction to identify spatial and spin terms that transform as IR objects in the point group,

$$\begin{aligned} h_{ss} \;=\; & -\frac{\mu_0 g^2 \beta^2}{4\pi}\left[\frac{1-3\hat{z}^2}{4r^3}(s_{1+}s_{2-} + s_{1-}s_{2+} - 4s_{1z}s_{2z})\right. \\ & +\frac{3}{4}\frac{\hat{x}^2-\hat{y}^2}{r^3}(s_{1-}s_{2-} + s_{1+}s_{2+}) \\ & +i\frac{3}{2}\frac{\hat{x}\hat{y}}{r^3}(s_{1-}s_{2-} - s_{1+}s_{2+}) \\ & +\frac{3}{2}\frac{\hat{x}\hat{z}}{r^3}(s_{1-}s_{2z} + s_{1z}s_{2-} + s_{1+}s_{2z} + s_{1z}s_{2+}) \\ & \left.+i\frac{3}{2}\frac{\hat{y}\hat{z}}{r^3}(s_{1-}s_{2z} + s_{1z}s_{2-} - s_{1+}s_{2z} - s_{1z}s_{2+})\right], \end{aligned}$$

where $\hat{x}, \hat{y}$ and $\hat{z}$ are directional cosines and $s_\pm = s_x \pm i s_y$. In the case of C_{3v}, for the unperturbed center, the expectation values of the 4th and 5th terms are not zero in the spatial manifold of the excited state $\{|X\rangle, |Y\rangle\}$ because the center lacks inversion symmetry and therefore we cannot neglect them. However, these terms might be

neglected when considering other defects with inversion symmetry. We note now that the spatial part of the first term transforms as the totally symmetric representation A_1, while the 2nd and 3rd terms transform as the irreducible representation E. The reader can check which IR these combinations belong to by looking at the character table in the appendix. Therefore, their expectation values can be written as

$$\begin{aligned}
\frac{\mu_0}{4\pi}g^2\beta^2\left\langle\frac{1-3\hat{z}^2}{4r^3}\right\rangle &= \Delta(|X\rangle\langle X|+|Y\rangle\langle Y|)\\
\frac{\mu_0}{4\pi}g^2\beta^2\left\langle\frac{3\hat{x}^2-3\hat{y}^2}{4r^3}\right\rangle &= \Delta'(|X\rangle\langle X|-|Y\rangle\langle Y|)\\
\frac{\mu_0}{4\pi}g^2\beta^2\left\langle\frac{3\hat{x}\hat{y}+3\hat{y}\hat{x}}{4r^3}\right\rangle &= \Delta'(|X\rangle\langle Y|+|Y\rangle\langle X|),\\
\frac{\mu_0}{4\pi}g^2\beta^2\left\langle\frac{3\hat{x}\hat{z}+3\hat{z}\hat{x}}{4r^3}\right\rangle &= \Delta''(|Y\rangle\langle Y|-|X\rangle\langle X|),\\
\frac{\mu_0}{4\pi}g^2\beta^2\left\langle\frac{3\hat{z}\hat{y}+3\hat{y}\hat{z}}{4r^3}\right\rangle &= \Delta''(|X\rangle\langle Y|+|Y\rangle\langle X|),
\end{aligned} \tag{E.4}$$

where $|X\rangle$ and $|Y\rangle$ are the two electron states given in Table 6.1. Note that, for symmetry reasons, the second and third relations are characterized by the same parameter Δ', while the last two relations are characterized by the same parameter Δ''. Similarly, it is possible to write the spin operators in the spin basis of the two holes, $\{|\alpha\alpha\rangle, |\alpha\beta\rangle, |\beta\alpha\rangle, |\beta\beta\rangle\}$, e.g., $s_{1+}s_{2-} = |\alpha\beta\rangle\langle\beta\alpha|$. Using these relations and Equation (E.4), the hamiltonian in the fundamental bases of the excited state of the NV center

is

$$
\begin{aligned}
H_{ss} \;=\; & -\Delta(|X\rangle\langle X| + |Y\rangle\langle Y|) \qquad \text{(E.5)}\\
& \otimes (|\alpha\alpha\rangle\langle\alpha\alpha| + |\beta\beta\rangle\langle\beta\beta| - 2|\alpha\beta+\beta\alpha\rangle\langle\alpha\beta+\beta\alpha|)\\
& -\Delta'(|X\rangle\langle X| - |Y\rangle\langle Y|) \otimes (|\alpha\alpha\rangle\langle\beta\beta| + |\beta\beta\rangle\langle\alpha\alpha|)\\
& -i\Delta'(|X\rangle\langle Y| + |Y\rangle\langle X|) \otimes (|\beta\beta\rangle\langle\alpha\alpha| - |\alpha\alpha\rangle\langle\beta\beta|)\\
& +\Delta''(|Y\rangle\langle Y| - |X\rangle\langle X|)\\
& \otimes (|\alpha\beta+\beta\alpha\rangle\langle\alpha\alpha-\beta\beta| + |\alpha\alpha-\beta\beta\rangle\langle\alpha\beta+\beta\alpha|)\\
& +i\Delta''(|Y\rangle\langle Y| - |X\rangle\langle X|)\\
& \otimes (|\alpha\beta+\beta\alpha\rangle\langle\alpha\alpha+\beta\beta| - |\alpha\alpha+\beta\beta\rangle\langle\alpha\beta+\beta\alpha|)\,. \qquad \text{(E.6)}
\end{aligned}
$$

Finally, to see the effect of this interaction on the excited state triplet more clearly, we can write H_{ss} in terms of the eigenstates of the unperturbed defect (see Table 6.1). This leads to Equation (6.7).

E.4 Strain and electric field

The effect of strain on the electronic structure of the defect can be obtained from the effect of the electron-nuclei Coulomb interaction on the eigenstates of the defect. In our example, the Coulomb interaction is given by Equation (E.1). However, when the positions of the atoms are such that the symmetry of the defect is reduced, we should allow for different expectation values of the matrix elements, i.e., $h_{ij} = \langle\sigma_i|V|\sigma_j\rangle$ and $h_{in} = \langle\sigma_i|V|\sigma_N\rangle$. We have assumed that the self interactions, v_c and v_n, do not change as the electrons follow the position of the ion (Born Oppenheimer

approximation). To relate the matrix elements to the ionic displacements, we can assume as a first approximation that the electron orbitals are spherical functions, and therefore the matrix elements can be parametrized by the distance between ions, $h_{ij}(q_i, q_j) = h_{ij}(|q_i - q_j|)$, so that we can write

$$h_{ij}(|q_{ij}|) \approx h_{ij}\left(|q_{ij}^0|\right) + \frac{1}{|q_{ij}|}\frac{\partial h_{ij}}{\partial q_{ij}}(q_i - q_j)\Big|_0 \cdot (\delta q_i - \delta q_j) + ... \tag{E.7}$$

The change in the matrix elements is linear in the atomic displacements. In turn, the atomic displacements are related to the strain tensor by $\delta q_i = e q_i$, and therefore the change in the matrix element is given by

$$\delta h_{ij}(|q_{ij}|) \approx \frac{1}{|q_{ij}|}\frac{\partial h_{ij}}{\partial q_{ij}}(q_i - q_j)^T e\,(q_i - q_j)\Big|_0 . \tag{E.8}$$

Under these considerations, it is straightforward to calculate the effect of strain on the eigenstates of the defect. For simplicity, we write here only the effect of strain on the degenerate orbitals, e_x and e_y,

$$\delta V = -g \begin{pmatrix} e_{xx} & e_{xy} \\ e_{xy} & e_{yy} \end{pmatrix}, \tag{E.9}$$

where $g = \frac{8}{3}\frac{\partial h_{ij}}{\partial q_{ij}}$. Using the electron wavefunction calculated by the CRYSTAL code we estimate that $g \sim 1000$ THz/fm.

The effect of electric field on the eigenstates of the defect can be analyzed by the inverse piezoelectric effect as described in Section 6.7.1. In this appendix we show how group theory can tell us the nature of the piezoelectric tensor. By projecting d_{ijk} (or $x_i x_j x_k$) onto the irreducible representation A_1, we can build the following

relations,

$$a = d_{111} = -d_{221} = -d_{122} \qquad d = d_{333} \tag{E.10}$$

$$b = d_{113} = d_{223} \qquad c = d_{131} = d_{232} \tag{E.11}$$

and the d tensor can be written in the following short notation (contracted matrix form)[142]

$$d_{ijk} \rightarrow \begin{pmatrix} a & -a & & c & \\ & & c & & -2a \\ b & b & d & & \end{pmatrix}. \tag{E.12}$$

For a given electric field, we have a strain tensor of the form

$$\epsilon = \begin{pmatrix} aE_x + bE_z & -aE_y & cE_x \\ -aE_y & -aE_x + bE_z & cE_y \\ cE_x & cE_y & dE_z \end{pmatrix}. \tag{E.13}$$

To evaluate the magnitude of the piezo-electric response, we have used the software SIESTA where the NV center is treated as a molecule composed of 70 Carbons with a hydrogen terminated on the surface. We have found that the atom displacements in the presence of 1 MV/m electric field are on the order of a few 0.1 μA.

E.5 Information about the first principles methods applied in our study

The spin-orbit energy was calculated by following Equation (6.4) in our manuscript. Since the spin-orbit interaction is a short-range interaction, we applied all-electron

methods beyond the frozen-core approximation. We utilized the CRYSTAL code for this calculation using the PBE functional within density functional theory (DFT). We applied 6-31*G Gaussian basis set for both the carbon and nitrogen atoms. The calculated properties (like the position of the defect levels in the gap) agreed well with those from plane wave calculations. We used a 512-atom simple cubic supercell with Γ-point sampling. After optimizing the geometry in the ground state, we obtained the all-electron single particle states and the corresponding Kohn-Sham potentials on a grid, and we calculated the spin-orbit energy numerically. Convergence tests confirmed the numerical accuracy of our method.

The electron spin-spin interaction is not sensitive to the electron wave functions close to the ions, thus we applied the plane wave PWSCF code with ultrasoft pseudopotentials to obtain the single particle wave functions. The spin-spin interaction is then calculated in the Fourier-space by following Equation (17) in Ref. [138]. We used the occupied Kohn-Sham PBE DFT states in the gap in the evaluation of the electron spin-spin interaction.

Bibliography

[1] N. F. Ramsey. *Molecular Beams*. Oxford University Press, 1990.

[2] E. L. Hahn. Spin echoes. *Phys. Rev.*, 80(4):580–594, Nov 1950.

[3] C. Langer, R. Ozeri, J. D. Jost, J. Chiaverini, B. DeMarco, A. Ben-Kish, R. B. Blakestad, J. Britton, D. B. Hume, W. M. Itano, D. Leibfried, R. Reichle, T. Rosenband, T. Schaetz, P. O. Schmidt, and D. J. Wineland. Long-lived qubit memory using atomic ions. *Phys. Rev. Lett.*, 95(6):060502, Aug 2005.

[4] J. McKeever, A. Boca, A. D. Boozer, R. Miller, J. R. Buck, A. Kuzmich, and H. J. Kimble. Deterministic generation of single photons from one atom trapped in a cavity. *Science*, 303(5666):1992–1994, 2004.

[5] J. M. Raimond, M. Brune, and S. Haroche. Manipulating quantum entanglement with atoms and photons in a cavity. *Rev. Mod. Phys.*, 73(3):565–582, Aug 2001.

[6] Wolfgang Paul. Electromagnetic traps for charged and neutral particles. *Rev. Mod. Phys.*, 62(3):531–540, Jul 1990.

[7] J. I. Cirac and P. Zoller. Quantum computations with cold trapped ions. *Phys. Rev. Lett.*, 74(20):4091–4094, May 1995.

[8] C. Monroe, D. M. Meekhof, B. E. King, W. M. Itano, and D. J. Wineland. Demonstration of a fundamental quantum logic gate. *Phys. Rev. Lett.*, 75(25):4714–4717, Dec 1995.

[9] H. Haffner, W. Hansel, C. F. Roos, J. Benhelm, D. Chek-al kar, M. Chwalla, T. Korber, U. D. Rapol, M. Riebe, P. O. Schmidt, C. Becher, O. Guhne, W. Dur, and R. Blatt. Scalable multiparticle entanglement of trapped ions. *Nature*, 438:643–646, 2005.

[10] J. Chiaverini, J. Britton, D. Leibfried, E. Knill, M. D. Barrett, R. B. Blakestad, W. M. Itano, J. D. Jost, C. Langer, R. Ozeri, T. Schaetz, and D. J. Wineland. Implementation of the Semiclassical Quantum Fourier Transform in a Scalable System. *Science*, 308(5724):997–1000, 2005.

[11] I. Chiorescu, Y. Nakamura, C. J. P. M. Harmans, and J. E. Mooij. Coherent Quantum Dynamics of a Superconducting Flux Qubit. *Science*, 299(5614):1869–1871, 2003.

[12] J. R. Petta, A. C. Johnson, J. M. Taylor, E. A. Laird, A. Yacoby, M. D. Lukin, C. M. Marcus, M. P. Hanson, and A. C. Gossard. Coherent Manipulation of Coupled Electron Spins in Semiconductor Quantum Dots. *Science*, 309(5744):2180–2184, 2005.

[13] A. D. Armour, M. P. Blencowe, and K. C. Schwab. Entanglement and decoherence of a micromechanical resonator via coupling to a cooper-pair box. *Phys. Rev. Lett.*, 88(14):148301, Mar 2002.

[14] B. E. Kane. A silicon-based nuclear spin quantum computer. *Nature*, 393:133–137, 1998.

[15] T. G. Castner. Direct measurement of the valley-orbit splitting of shallow donors in silicon. *Phys. Rev. Lett.*, 8(1):13–15, Jan 1962.

[16] A. M. Tyryshkin, S. A. Lyon, A. V. Astashkin, and A. M. Raitsimring. Electron spin relaxation times of phosphorus donors in silicon. *Phys. Rev. B*, 68(19):193207, Nov 2003.

[17] D. K. Wilson and G. Feher. Electron spin resonance experiments on donors in silicon. iii. investigation of excited states by the application of uniaxial stress and their importance in relaxation processes. *Phys. Rev.*, 124(4):1068–1083, Nov 1961.

[18] A. Gali, M. Fyta, and E. Kaxiras. Ab initio supercell calculations on nitrogen-vacancy center in diamond: Electronic structure and hyperfine tensors. *Phys. Rev. B*, 77:155206, 2008.

[19] R. Farrer. On the substitutional nitrogen donor in diamond. *Solid State Communications*, 7:685–688, May 1969.

[20] I. Aharonovich, S. Castelletto, D. A. Simpson, A. Stacey, J. McCallum, A. D. Greentree, and Prawer S. Two-level ultrabright single photon emission from diamond nanocrystals. *Nano Letters*, 9:3191–3195, 2009.

[21] A. Gruber, A. Drabenstedt, C. Tietz, L. Fleury, J. Wrachtrup, and C. von Borczyskowski. Scanning Confocal Optical Microscopy and Magnetic Resonance on Single Defect Centers. *Science*, 276(5321):2012–2014, 1997.

[22] E van Oort, N B Manson, and M Glasbeek. Optically detected spin coherence of the diamond n-v centre in its triplet ground state. *Journal of Physics C: Solid State Physics*, 21(23):4385, 1988.

[23] J. Wrachtrup and F. Jelezko. Processing quantum information in diamond. *Journal of Physics-Condensed Matter*, 18:S807–S824, 2006.

[24] L. Childress, J. M. Taylor, A. S. Sorensen, and M. D. Lukin. Fault-tolerant quantum communication based on solid-state photon emitters. *Phys. Rev. Lett.*, 96(7):070504–4, 2006.

[25] J.M. Taylor, P. Cappellaro, L. Childress, L. Jiang, D. Budker, P.R. Hemmer, A. Yacoby, R. Walsworth, and M.D. Lukin. High-sensitivity diamond magnetometer with nanoscale resolution. *Nat. Phys.*, 4:810–816, 2008.

[26] C. L. Degen. Scanning magnetic field microscope with a diamond single-spin sensor. *Appl. Phys. Lett.*, 92:243111, 2008.

[27] J. R. Maze, P. L. Stanwix, J. S. Hodges, S. Hong, J. M. Taylor, P. Cappellaro, L. Jiang, M. V. G. Dutt, E. Togan, A. S. Zibrov, A. Yacoby, R. L. Walsworth, and M. D. Lukin. Nanoscale magnetic sensing with an individual electronic spin in diamond. *Nature*, 455:644–647, 2008.

[28] G. Balasubramanian, I. Y. Chan, R. Kolesov, M. Al-Hmoud, J. Tisler, C. Shin, C. Kim, A. Wojcik, P. R. Hemmer, A. Krueger, T. Hanke, A. Leitenstorfer, R. Bratschitsch, F. Jelezko, and J. Wrachtrup. Nanoscale imaging magnetometry with diamond spins under ambient conditions. *Nature*, 455:648–651, 2008.

[29] S. Schietinger, M. Barth, T. Aichele, and O. Benson. Plasmon-enhanced single photon emission from a nanoassembled metal-diamond hybrid structure at room temperature. *Nano Letters*, 9(4):1694–1698, 2009.

[30] T. M. Babinec, Hausmann B. J. M., M. Khan, Y. Zhang, J. R. Maze, P. R. Hemmer, and M. Loncar. A diamond nanowire single-photon source. *Nat. Nano.*, 5:195–199, 2010.

[31] K.-M. C. Fu, C. Santori, P. E. Barclay, I. Aharonovich, S. Prawer, N. Meyer, A. M. Holm, and R. G. Beausoleil. Coupling of nitrogen-vacancy centers in diamond to a gap waveguide. *Applied Physics Letters*, 93(23):234107, 2008.

[32] P. Stanwix, M. L. Pham, D LeSage, Yeung, J. R. Maze, P. Cappellaro, P. Hemmer, M. D. Lukin, A. Yacoby, and R. Walsworth. bla dependence on magnetic field ensemble measurements. *to be published*, 2010.

[33] D. Budker and M. Romalis. Optical magnetometry. *Nature Physics*, 3(4):227–234, 2007.

[34] S. J. Bending. Local magnetic probes of superconductors. *Advances in Physics*, 48(4):449, 1999.

[35] R. Kleiner, D. Koelle, F. Ludwig, and J. Clarke. Superconducting quantum interference devices: State of the art and applications. *Proceedings of the IEEE*, 92(10):1534–1548, 2004.

[36] C. N. Owston. A hall effect magnetometer for small magnetic fields. *Journal of Scientific Instruments*, 44(9):798–800, 1967.

[37] D. Rugar, R. Budakian, H. J. Mamin, and B. W. Chui. Single spin detection by magnetic resonance force microscopy. *Nature*, 430(6997):329–332, 2004.

[38] H. J. Mamin, M. Poggio, C. L. Degen, and D. Rugar. Nuclear magnetic resonance imaging with 90-nm resolution. *Nature Nanotechnology*, 2(5):301–306, 2007.

[39] M. V. Gurudev Dutt, L. Childress, L. Jiang, E. Togan, J. Maze, F. Jelezko, A. S. Zibrov, P. R. Hemmer, and M. D. Lukin. Quantum register based on individual electronic and nuclear spin qubits in diamond. *Science*, 316(5829):1312–1316, 2007.

[40] Vanier J. and C. Audoin. *The quantum physics of atomic frequency standards.* Hilger, Philadelphia, 1989.

[41] S. T. Cundiff and J. Ye. Colloquium: Femtosecond optical frequency combs. *Rev. Mod. Phys.*, 75:325–342, 2003.

[42] D. Budker, Kimball D. F., and D. P. DeMille. *Atomic Physics: An Exploration Through Problems and Solutions*. Oxford University Press, 2004.

[43] Xiaodong Xu, Bo Sun, Paul R. Berman, Duncan G. Steel, Allan S. Bracker, Dan Gammon, and L. J. Sham. Coherent Optical Spectroscopy of a Strongly Driven Quantum Dot. *Science*, 317(5840):929–932, 2007.

[44] K. Hennessy, A. Badolato, M. Winger, D. Gerace, M. Atature, S. Gulde, S. Falt, E. L. Hu, and A. Imamoglu. Quantum nature of a strongly coupled single quantum dotcavity system. *Nature*, 445:896–899, 2007.

[45] P. Neumann, N. Mizuochi, F. Rempp, P. Hemmer, H. Watanabe, S. Yamasaki, V. Jacques, T. Gaebel, F. Jelezko, and J. Wrachtrup. Multipartite Entanglement Among Single Spins in Diamond. *Science*, 320(5881):1326–1329, 2008.

[46] B. M. Chernobrod and G. P. Berman. Spin microscope based on optically detected magnetic resonance. *Journal of Applied Physics*, 97(1):014903, 2005.

[47] S. W. Hell and J. Wichmann. Breaking the diffraction resolution limit by stimulated emission: stimulated-emission-depletion fluorescence microscopy. *Opt. Lett.*, 19:780–782, 1994.

[48] W. M. Itano, D. J. Heinzen, J. J. Bollinger, and D. J. Wineland. Quantum zeno effect. *Phys. Rev. A*, 41:2295, 1990.

[49] D. Loss and D. P. DiVincenzo. Quantum computation with quantum dots. *Phys. Rev. A*, 57(1):120–126, Jan 1998.

[50] N. B. Manson, X.-F. He, and P. T. H. Fisk. Raman heterodyne detected electron-nuclear double-resonance measurements of the nitrogen-vacancy center in diamond. *Optics Letters*, 15:1094–1096, 1990.

[51] F. Jelezko, T. Gaebel, I. Popa, A. Gruber, and J. Wrachtrup. Observation of coherent oscillations in a single electron spin. *Physical Review Letters*, 92(7):076401, 2004.

[52] M. Van Oort E.and Glasbeek. Optically detected low field electron spin echo envelope modulations of fluorescent n-v centers in diamond. *Chemical Physics*, 143(1):131–140, May 1990.

[53] L. Childress, M. V. Gurudev Dutt, J. M. Taylor, A. S. Zibrov, F. Jelezko, J. Wrachtrup, P. R. Hemmer, and M. D. Lukin. Coherent dynamics of coupled electron and nuclear spin qubits in diamond. *Science*, 314(5797):281–285, 2006.

[54] N. Shenvi, R. de Sousa, and K. B. Whaley. Universal scaling of hyperfine-induced electron spin echo decay. *Phys. Rev. B*, 71(22):224411–8, 2005.

[55] W. A. Coish and D. Loss. Hyperfine interaction in a quantum dot: Non-markovian electron spin dynamics. *Phys. Rev. B*, 70(19):195340, 2004.

[56] R. de Sousa and S. Das Sarma. Electron spin coherence in semiconductors: Considerations for a spin-based solid-state quantum computer architecture. *Phys. Rev. B*, 67(3):033301, 2003.

[57] R. de Sousa and S. Das Sarma. Theory of nuclear-induced spectral diffusion: Spin decoherence of phosphorus donors in si and gaas quantum dots. *Phys. Rev. B*, 68(11):115322, 2003.

[58] W. M. Witzel, R. de Sousa, and S. Das Sarma. Quantum theory of spectral-diffusion-induced electron spin decoherence. *Phys. Rev. B*, 72(16):161306, 2005.

[59] W. A. Coish and D. Loss. Singlet-triplet decoherence due to nuclear spins in a double quantum dot. *Phys. Rev. B*, 72(12):125337–12, 2005.

[60] W. Yao, R.-B. Liu, and L. J. Sham. Theory of electron spin decoherence by interacting nuclear spins in a quantum dot. *Phys. Rev. B*, 74(19):195301–11, 2006.

[61] S. K. Saikin, W. Yao, and L. J. Sham. Single-electron spin decoherence by nuclear spin bath: Linked-cluster expansion approach. *Phys. Rev. B*, 75(12):125314–12, 2007.

[62] Y.-Y. Shi, L.-M. Duan, and G. Vidal. Classical simulation of quantum many-body systems with a tree tensor network. *Phys. Rev. A*, 74(2):022320, August 2006.

[63] J. P. Goss, R. Jones, S. Breuer, P. Briddon, and S. Oberg. The twelve-line 1.682 ev luminescence center in diamond and the vacancy-silicon complex. *Phys. Rev. Lett.*, 77:3041, 1996.

[64] Xing-Fei He, Neil B. Manson, and Peter T. H. Fisk. Paramagnetic resonance of photoexcited n-v defects in diamond. ii. hyperfine interaction with the ^{14}n nucleus. *Phys. Rev. B*, 47(14):8816–8822, Apr 1993.

[65] H. F. Trotter. On the Product of Semi-Groups of Operators. *Proc. Amer. Math. Soc.*, 10(4):545–551, 1959.

[66] N. Mizuochi, P. Neumann, F. Rempp, J. Beck, V. Jacques, P. Siyushev, K. Nakamura, D. J. Twitchen, H. Watanabe, S. Yamasaki, F. Jelezko, and J. Wrachtrup. Coherence of single spins coupled to a nuclear spin bath of varying density. *Phys. Rev. B*, 80(4):041201, Jul 2009.

[67] A. Abragam. *Principles of Nuclear Magnetism*. Oxford University Press, 1983.

[68] V. V. Dobrovitski, A. E. Feiguin, D. D. Awschalom, and R. Hanson. Decoherence dynamics of a single spin versus spin ensemble. *Phys. Rev. B*, 77(24):245212, Jun 2008.

[69] A. D. Ludlow, T. Zelevinsky, G. K. Campbell, S. Blatt, M. M. Boyd, M. H. G. de Miranda, M. J. Martin, J. W. Thomsen, S. M. Foreman, Jun Ye, T. M. Fortier, J. E. Stalnaker, S. A. Diddams, Y. Le Coq, Z. W. Barber, N. Poli, N. D. Lemke, K. M. Beck, and C. W. Oates. Sr Lattice Clock at 1 x 10-16 Fractional Uncertainty by Remote Optical Evaluation with a Ca Clock. *Science*, 319(5871):1805–1808, 2008.

[70] T. Rosenband, D. B. Hume, P. O. Schmidt, C. W. Chou, A. Brusch, L. Lorini, W. H. Oskay, R. E. Drullinger, T. M. Fortier, J. E. Stalnaker, S. A. Diddams, W. C. Swann, N. R. Newbury, W. M. Itano, D. J. Wineland, and J. C. Bergquist. Frequency ratio of Al^+ and Hg^+ single-ion optical clocks; metrology at the 17th decimal place. *Science*, 319(5871):1808–1812, 2008.

[71] D. J. Wineland, J. J. Bollinger, W. M. Itano, F. L. Moore, and D. J. Heinzen. Spin squeezing and reduced quantum noise in spectroscopy. *Physical Review A*, 46(11):R6797, 1992.

[72] I. K. Kominis, T. W. Kornack, J. C. Allred, and M. V. Romalis. A subfemtotesla multichannel atomic magnetometer. *Nature*, 422(6932):596–599, 2003.

[73] F. Jelezko, T. Gaebel, I. Popa, M. Domhan, A. Gruber, and J. Wrachtrup. Observation of coherent oscillation of a single nuclear spin and realization of a two-qubit conditional quantum gate. *Phys. Rev. Lett.*, 93(13):130501, Sep 2004.

[74] L. Jiang, M. V. Gurudev Dutt, E. Togan, L. Childress, P. Cappellaro, J. M. Taylor, and M. D. Lukin. Coherence of an optically illuminated single nuclear spin qubit. *Physical Review Letters*, 100(7):073001–4, 2008.

[75] R. Hanson, F. M. Mendoza, R. J. Epstein, and D. D. Awschalom. Polarization and readout of coupled single spins in diamond. *Physical Review Letters*, 97(8):087601, 2006.

[76] T. Gaebel, M. Domhan, I. Popa, C. Wittmann, P. Neumann, F. Jelezko, J. R. Rabeau, N. Stavrias, A. D. Greentree, S. Prawer, J. Meijer, J. Twamley, P. R. Hemmer, and J. Wrachtrup. Room-temperature coherent coupling of single spins in diamond. *Nature Physics*, 2(6):408–413, 2006.

[77] R. Hanson, V. V. Dobrovitski, A. E. Feiguin, O. Gywat, and D. D. Awschalom. Coherent dynamics of a single spin interacting with an adjustable spin bath. *Science*, 320(5874):352–355, 2008.

[78] J. R. Kirtley, M. B. Ketchen, K. G. Stawiasz, J. Z. Sun, W. J. Gallagher, S. H. Blanton, and S. J. Wind. High-resolution scanning squid microscope. *Applied Physics Letters*, 66(9):1138–1140, 1995.

[79] M. I. Faley, U. Poppe, K. Urban, D. N. Paulson, and R. L. Fagaly. A new generation of the hts multilayer dc-squid magnetometers and gradiometers. *Journal of Physics: Conference Series*, 43:1199–1202, 2006.

[80] F. Baudenbacher, L. E. Fong, J. R. Holzer, and M. Radparvar. Monolithic low-transition-temperature superconducting magnetometers for high resolution imaging magnetic fields of room temperature samples. *Applied Physics Letters*, 82(20):3487–3489, 2003.

[81] A. Sandhu, A. Okamoto, I. Shibasaki, and A. Oral. Nano and micro hall-effect sensors for room-temperature scanning hall probe microscopy. *Microelectronic Engineering*, 73-74:524 – 528, 2004. Micro and Nano Engineering 2003.

[82] A. Sandhu, K. Kurosawa, M. Dede, and A. Oral. 50 nm hall sensors for room temperature scanning hall probe microscopy. *Jpn. J. Appl. Phys.*, 43:777–778, 2004.

[83] M. Vengalattore, J. M. Higbie, S. R. Leslie, J. Guzman, L. E. Sadler, and D. M. Stamper-Kurn. High-resolution magnetometry with a spinor bose-einstein condensate. *Phys. Rev. Lett.*, 98(20):200801, May 2007.

[84] V. Shah, S. Knappe, P. D. D. Schwindt, and J. Kitching. Subpicotesla atomic magnetometry with a microfabricated vapour cell. *Nat. Photonics*, 1:649–652, 2007.

[85] J. R. Maze, J. M. Taylor, and M. D. Lukin. Electron spin decoherence of single nitrogen-vacancy defects in diamond. *Phys. Rev. B*, 78:094303, 2008.

[86] J. R. Rabeau, A. Stacey, A. Rabeau, S. Prawer, F. Jelezko, I. Mirza, and J. Wrachtrup. Single nitrogen vacancy centers in chemical vapor deposited diamond nanocrystals. *Nano Letters*, 7(11):3433–3437, 2007.

[87] J. R. Rabeau, P. Reichart, G. Tamanyan, D. N. Jamieson, S. Prawer, F. Jelezko, T. Gaebel, I. Popa, M. Domhan, and J. Wrachtrup. Implantation of labelled single nitrogen vacancy centers in diamond using ^{15}N. *Applied Physics Letters*, 88(2):023113, 2006.

[88] D. E. Chang, A. S. Sorensen, P. R. Hemmer, and M. D. Lukin. Quantum optics with surface plasmons. *Physical Review Letters*, 97(5):053002, 2006.

[89] J. I. Cirac and P. Zoller. A scalable quantum computer with ions in an array of microtraps. *Nature*, 404(6778):579–581, 2000.

[90] P. Treutlein, D. Hunger, S. Camerer, T. W. Hansch, and J. Reichel. Bose-einstein condensate coupled to a nanomechanical resonator on an atom chip. *Physical Review Letters*, 99(14):140403–4, 2007.

[91] P. Rabl, P. Cappellaro, M. V. Gurudev Dutt, L. Jiang, J. R. Maze, and M. D. Lukin. Strong magnetic coupling between an electronic spin qubit and a mechanical resonator. *Phys. Rev. B*, 79(4):041302, Jan 2009.

[92] R. Blatt and D. Wineland. Entangled states of trapped atomic ions. *Nature (London)*, 453:1008–1015, 2008.

[93] R. Hanson and D. D. Awschalom. Coherent manipulation of single spins in semiconductors. *Nature (London)*, 453:1043–1049, 2008.

[94] M. Riebe, H. Haffner, C. F. Roos, W. Hansel, J. Benhelm, G. P. T. Lancaster, T. W. Korber, C. Becher, F. Schmidt-Kaler, D. F. V. James, and R. Blatt. Deterministic quantum teleportation with atoms. *Nature (London)*, 429:734–737, 2004.

[95] R. Reichle, D. Leibfried, E. Knill, J. Britton, R. B. Blakestad, J. D. Jost, C. Langer, R. Ozeri, S. Seidelin, and D. J. Wineland. Experimental purification of two-atom entanglement. *Nature (London)*, 443:838–841, 2006.

[96] L. DiCarlo, J. M. Chow, J. M. Gambetta, Lev S. Bishop, B. R. Johnson, D. I. Schuster, J. Majer, A. Blais, L. Frunzio, S. M. Girvin, and R. J. Schoelkopf. Demonstration of two-qubit algorithms with a superconducting quantum processor. *Nature (London)*, 460:240–244, 2009.

[97] C. A. Ryan, C. Negrevergne, M. Laforest, E. Knill, and R. Laflamme. Liquid-state nuclear magnetic resonance as a testbed for developing quantum control methods. *Phys. Rev. A*, 78:012328–14, 2008.

[98] D. B. Hume, T. Rosenband, and D. J. Wineland. High-fidelity adaptive qubit detection through repetitive quantum nondemolition measurements. *Phys. Rev. Lett.*, 99:120502–4, 2007.

[99] W. M. Witzel and S. Das Sarma. Wavefunction considerations for the central spin decoherence problem in a nuclear spin bath. *Phys. Rev. B*, 77:165319, 2008.

[100] W. A. Coish, J. Fischer, and D. Loss. Exponential decay in a spin bath. *Phys. Rev. B*, 77:125329–8, 2008.

[101] John J. L. Morton, Alexei M. Tyryshkin, Arzhang Ardavan, Simon C. Benjamin, Kyriakos Porfyrakis, S. A. Lyon, and G. Andrew D. Briggs. Bang-bang control of fullerene qubits using ultrafast phase gates. *Nat. Phys.*, 2:40–43, 2006.

[102] J. S. Hodges, J. C. Yang, C. Ramanathan, and D. G. Cory. Universal control of nuclear spins via anisotropic hyperfine interactions. *Phys. Rev. A*, 78:010303–4, 2008.

[103] J. J. L. Morton, A. M. Tyryshkin, R. M. Brown, S. Shankar, B. W. Lovett, A. Ardavan, T. Schenkel, E. E. Haller, J. W. Ager, and S. A. Lyon. Solid-state quantum memory using the 31p nuclear spin. *Nature (London)*, 455:1085–1088, 2008.

[104] G. Balasubramanian, P. Neumann, D. Twitchen, M. Markham, R. Kolesov, N. Mizuochi, J. Isoya, J. Achard, J. Beck, J. Tissler, V. Jacques, P. R. Hemmer, F. Jelezko, and J. Wrachtrup. Ultralong spin coherence time in isotopically engineered diamond. *Nat. Mater.*, 8:383–387, 2009.

[105] G. D. Fuchs, V. V. Dobrovitski, R. Hanson, A. Batra, T. Weis, C. D.and Schenkel, and D. D. Awschalom. Excited-state spectroscopy using single spin manipulation in diamond. *Phys. Rev. Lett.*, 101:117601, 2008.

[106] L. Jiang, J. M. Taylor, A. S. Sorensen, and M. D. Lukin. Distributed quantum computation based on small quantum registers. *Physical Review A (Atomic, Molecular, and Optical Physics)*, 76(6):062323–22, 2007.

[107] S. Haroche and J. M. Raimond. *Exploring the quantum : atoms, cavities, and photons*. Oxford University Press, Oxford ; New York, 2006.

[108] M. Sarovar, K. C. Young, T. Schenkel, and K. B. Whaley. Quantum nondemolition measurements of single donor spins in semiconductors. *Phys. Rev. B*, 78:245302–8, 2008.

[109] N. Khaneja, T. Reiss, C. Kehlet, T. Schulte-Herbruggen, and S. J. Glaser. Optimal control of coupled spin dynamics: design of nmr pulse sequences by gradient ascent algorithms. *J. Magn. Reson.*, 172:296–305, 2005.

[110] P. Cappellaro, L. Jiang, J. S. Hodges, and M. D. Lukin. Coherence and control of quantum registers based on electronic spin in a nuclear spin bath. *Phys. Rev. Lett.*, 102:210502, 2009.

[111] N. B. Manson, J. P. Harrison, and M. J. Sellars. Nitrogen-vacancy center in diamond: Model of the electronic structure and associated dynamics. *Phys. Rev. B*, 74:104303, 2006.

[112] A. Batalov, V. Jacques, F. Kaiser, P. Siyushev, P. Neumann, L. J. Rogers, R. L. McMurtrie, N. B. Manson, F. Jelezko, and J. Wrachtrup. Low temperature studies of the excited-state structure of negatively charged nitrogen-vacancy color centers in diamond. *Phys. Rev. Lett.*, 102:195506, 2009.

[113] Volker Westphal, Silvio O. Rizzoli, Marcel A. Lauterbach, Dirk Kamin, Reinhard Jahn, and Stefan W. Hell. Video-Rate Far-Field Optical Nanoscopy Dissects Synaptic Vesicle Movement. *Science*, 320(5873):246–249, 2008.

[114] X. Zhuang. Nano-imaging with storm. *Nat. Photonics*, 3:365–367, 2009.

[115] E. Betzig, G. H. Patterson, R. Sougrat, O. W. Lindwasser, S. Olenych, J. S. Bonifacino, M. W. Davidson, J. Lippincott-Schwartz, and H. F. Hess. Imaging Intracellular Fluorescent Proteins at Nanometer Resolution. *Science*, 313(5793):1642–1645, 2006.

[116] L. J. Li, R. R. Gattass, E. Gershgoren, H. Hwang, and J. T. Fourkas. Achieving /20 resolution by one-color initiation and deactivation of polymerization. *Science*, 324:910–913, 2009.

[117] T. F. Scott, B. A. Kowalski, A. C. Sullivan, C. N. Bowman, and R. R. McLeod. Two-color single-photon photoinitiation and photoinhibition for subdiffraction photolithography. *Science*, 324:913–917, 2009.

[118] K. S. Johnson, J. H. Thywissen, N. H. Dekker, K. K. Berggren, A. P. Chu, R. Younkin, and M. Prentiss. Localization of Metastable Atom Beams with Optical Standing Waves: Nanolithography at the Heisenberg Limit. *Science*, 280(5369):1583–1586, 1998.

[119] S. W. Hell. Far-field optical nanoscopy. *Science*, 316:1153–1158, 2007.

[120] S. W. Hell and M. Kroug. Ground-state-depletion fluorscence microscopy: A concept for breaking the diffraction resolution limit. *Appl. Phys. B*, 60:495–497, 1995.

[121] E. Rittweger, K. Y. Han, S. E. Irvine, C. Eggeling, and S. E. Hell. Sted microscopy reveals crystal colour centres with nanometric resolution. *Nat. Phot.*, 3:144–147, 2009.

[122] P. Neumann, J. Beck, M. Steiner, H. Rathgen, P. R. Hemmer, J. Wrachtrup, and F. Jelezko. Quantum non-demolition measurement of a single nuclear spin. *submitted for publication*, X:X, 2010.

[123] A. V. Gorshkov, L. Jiang, M. Greiner, P. Zoller, and M. D. Lukin. Coherent quantum optical control with subwavelength resolution. *Phys. Rev. Lett.*, 100:093005, 2008.

[124] E. Togan, Y. Chu, A. S. Trifonov, L. Jiang, J. R. Maze, L. Childress, M. V. G. Dutt, A. Sorensen, P. R. Hemmer, A. S. Zibrov, and M. D. Lukin. Quantum entanglement between an optical photon and a solid-state spin qubit. *submitted to Nature*, 2010.

[125] C. Santori, P. Tamarat, P. Neumann, J. Wrachtrup, D. Fattal, R. G. Beausoleil, J. Rabeau, P. Olivero, A. D. Greentree, S. Prawer, S. Jelezko, and P. Hemmer. Coherent population trapping of single spins in diamond under optical excitation. *Phys. Rev. Lett.*, 97:247401, 2006.

[126] A. Lenef and S. Rand. Electronic structure of the nv center in diamond: Theory. *Phys. Rev. B*, 53:13441–13445, 1996.

[127] L. J. Rogers, R. McMurtrie, M. Sellars, and N. B. Manson. Time-averaging within the excited state of the nitrogen-vacancy centre in diamond. *New Journal of Physics*, 11:063007, 2009.

[128] Y. Ma, M. Rohlfing, and A. Gali. Excited states of the negatively charged nitrogen-vacancy color center in diamond. *Phys. Rev. B*, 81(4):(R), Jan 2010.

[129] Ph. Tamarat, N. B. Manson, J. P. Harrison, R. L. McMurtrie, A. Nizovtsev, C. Santori, R. G. Beausoleil, P. Neumann, T. Gaebel, F. Jelezko, and

J. Hemmer, P. Wrachtrup. Spin-ip and spin-conserving optical transitions of the nitrogen-vacancy centre in diamond. *New Journal of Physics*, 10:045004, 2008.

[130] M. Tinkham. *Group theory and quantum mechanics*. Courier Dover Publications, 2003.

[131] M. Lannoo, G. A. Baraff, and M. Schlüter. Self-consistent second-order perturbation treatment of multiplet structures using local-density theory. *Phys. Rev. B*, 24(2):943–954, Jul 1981.

[132] P. Kok and B. W. Lovett. Materials science: Qubits in the pink. *Nature*, 444:49, 2006.

[133] A. Stoneham. *Theory of defects in solids: electronic structure of defects in insulators and semiconductors*. Oxford University Press, 2001.

[134] J. S. Griffith. *The theory of transition-metal ions*. Cambridge University Press, 1961.

[135] P. Jacobs. *Group theory with applications in chemical physics*. Cambridge, 2005.

[136] A. Gali. Identification of individual ^{13}c isotopes of nitrogen-vacancy center in diamond by combining the polarization studies of nuclear spins and first-principles calculations. *Phys. Rev. B*, 80(24):241204, Dec 2009.

[137] P. Y. Yu and M. Cardona. *Fundamentals of semiconductors: physics and materials properties*. Springer, 2005.

[138] M. J. Rayson and P. R. Briddon. First principles method for the calculation of zero-field splitting tensors in periodic systems. *Phys. Rev. B*, 77:035119, 2008.

[139] F. M. Hossain, M. W. Doherty, H. F. Wilson, and L. C. L. Hollenberg. Ab initio electronic and optical properties of the n-v$^-$ center in diamond. *Phys. Rev. Lett.*, 101:26403, 2008.

[140] N. R. S. Reddy, N. B. Manson, and E. R. Krausz. Two-laser spectral hole burning in a colour centre in diamond. *Journal of Luminescence*, 38(1-6):46 – 47, 1987.

[141] B. B. Blinov, D. L. Moehring, L.-M. Duan, and C. Monroe. Observation of entanglement between a single trapped atom and a single photon. *Nature*, 428:153–157, 2004.

[142] J. Nye. *Physical properties of crystals: their representation by tensors and matrices*. Oxford University Press, 1985.

[143] G. Davies and M. F. Hamer. Optical studies of the 1.945 ev vibronic band in diamond. *Proceedings of the Royal Society of London. Series A*, 348:285, 1976.

[144] G. González and M. N. Leuenberger. Theory of optical λ transitions in the $^{1}5$n-v^{-} center in diamond: Role of the hyperfine interaction. *Phys. Rev. B*, 80(20):201201, Nov 2009.

[145] C. A. Bates. The linear electric field effect on the electron paramagnetic resonance spectrum of cu2+ ions in tetrahedral crystal fields. *J. Phys. C*, 1(4):877–888, 1968.

[146] P. Tamarat, T. Gaebel, J Rabeau, M. Khan, A. D. Greentree, H. Wilson, L. C. L. Hollenberg, S. Prawer, P. Hemmer, F. Jelezko, and J. Wrachtrup. Stark shift control of single optical centers in diamond. *Phys. Rev. Lett.*, 97:083002, 2006.

[147] H. A. Jahn and E. Teller. Stability of polyatomic molecules in degenerate electronic states. i. orbital degeneracy. *Proceedings of the Royal Society of London. Series A, Mathematical and Physical Sciences*, 161(905):220–235, 1937.

[148] E. Michel, R. Samadi, F. Baudin, C. Barban, T. Appourchaux, and M. Auvergne. Intrinsic photometric characterisation of stellar oscillations and granulation. *A&A*, 495(3):979–987, 2009.

[149] D. Yao and J. Shi. Projection operator approach to time-independent perturbation theory in quantum mechanics. *American Journal of Physics*, 68:278–281, 2000.

[150] E. A. Donley, T. P. Heavner, F. Levi, M. O. Tataw, and S. R. Jefferts. Double-pass acousto-optic modulator system. *Rev. Sci. Instrum.*, 76:063112, 2005.

[151] A. Abragam and B. Bleaney. *Electron paramagnetic resonance of transition ions*. Clarendon Press, 1970.

[152] S. Felton, A. M. Edmonds, M. E. Newton, P. M. Martineau, D. Fisher, D. J. Twitchen, and J. M. Baker. Hyperfine interaction in the ground state of the negatively charged nitrogen vacancy center in diamond. *Phys. Rev. B*, 79:075203–8, 2009.

[153] J. Harrison, M. Sellars, and N. Manson. Measurement of the optically induced spin polarisation of n-v centres in diamond. *Diamond and Related Materials*, 15(4-8):586–588, Apr 2006.

[154] J. Gambetta, W. A. Braff, A. Wallraff, S. M. Girvin, and R. J. Schoelkopf. Protocols for optimal readout of qubits using a continuous quantum nondemolition measurement. *Phys. Rev. A*, 76:012325, 2007.

[155] B. E. A. Saleh and M. C. Teich. *Fundamentals of Photonics*. John Wiley & Sons, Inc., 1991.

[156] Altmann S. L. *Rotations, quaternions, and double groups*. Clarendon Press, 1986.